EVALUATION OF THE VISIBLE INFRARED IMAGING RADIOMETER SUITE CLOUD BASE HEIGHT PIXEL-LEVEL RETRIEVAL ALGORITHM FOR SINGLE-LAYER WATER CLOUDS

THESIS

Kyle E. Fitch, Captain, USAF

AFIT-ENP-MS-16-M-069

DEPARTMENT OF THE AIR FORCE
AIR UNIVERSITY

AIR FORCE INSTITUTE OF TECHNOLOGY

Wright-Patterson Air Force Base, Ohio

AFIT-ENP-MS-16-M-069

EVALUATION OF THE VISIBLE INFRARED IMAGING RADIOMETER SUITE CLOUD BASE HEIGHT PIXEL-LEVEL RETRIEVAL ALGORITHM FOR SINGLE-LAYER WATER CLOUDS

THESIS

Presented to the Faculty

Department of Engineering Physics

Graduate School of Engineering and Management

Air Force Institute of Technology

Air University

Air Education and Training Command

in Partial Fulfillment of the Requirements for the

Degree of Master of Science

Kyle E. Fitch, BS

Captain, USAF

March 2016

AFIT-ENP-MS-16-M-069

EVALUATION OF THE VISIBLE INFRARED IMAGING RADIOMETER SUITE CLOUD BASE HEIGHT PIXEL-LEVEL RETRIEVAL ALGORITHM FOR SINGLE-LAYER WATER CLOUDS

THESIS

Kyle E. Fitch, BS
Captain, USAF

Committee Membership:

Lt Col Kevin S. Bartlett
Chair

Keith D. Hutchison, PhD
Member

Lt Col Robert S. Wacker
Member

Kevin C. Gross, PhD
Member

AFIT-ENP-MS-16-M-069

Abstract

A system-level analysis was performed on Visible Infrared Imaging Radiometer Suite (VIIRS) Cloud Base Height (CBH) products. CBH is an important factor for both aviation and climate research, but a lack of spatial coverage for ground-based CBH retrieval is a significant limitation. Therefore, space-based retrieval by polar-orbiting satellites is essential. The VIIRS CBH retrieval algorithm was evaluated for single-layer water clouds at moderate pixel resolution, which averages ˜1 km. Accurate (truth) measurements were needed not only for the CBH product, but also for other VIIRS data used to create the CBH product: cloud optical thickness (COT), effective particle size (EPS), and cloud top height (CTH). This necessitated the exploitation of ground-based data collected at the United States (U.S.) Department of Energy (DOE) Atmospheric Radiation Measurement (ARM) sites. Match-up datasets were created between VIIRS cloud products and DOE ARM site truth datasets from June 2013 through October 2015 for four locations. The initial results showed the error in the VIIRS CBH products to be large and highly variable; however, errors in VIIRS COT and the derived VIIRS cloud geometric thickness were much smaller. Consequently, the VIIRS CTH product was replaced with the ARM CTH (truth) product, which substantially reduced the variability and errors in the VIIRS CBH products - indicating that performance of the VIIRS CBH products were most strongly correlated with errors in the VIIRS CTH product, while errors in COT and cloud geometric thickness were acceptable. Once corrections were made for the CTH errors, the CBH products were found to be greatly improved, which verifies the technical approach used in the retrieval of

the CBH product. Thus, future research is needed to reduce the errors in the VIIRS CTH products in order to ensure the VIIRS CBH products are suitable for civilian and military aerodrome operations.

AFIT-ENP-MS-16-M-069

Dedicated to my wife, children, and parents for their love and support.

Acknowledgements

I would like to thank my advisor, Lieutenant Colonel (Lt Col) Kevin Bartlett, for his guidance and patience. I also wish to thank the members of my committee, Dr. Keith Hutchison, Lt Col Robert Wacker, and Dr. Kevin Gross. Dr. Hutchison paved the way in Visible Infrared Imaging Radiometer Suite (VIIRS) Cloud Base Height (CBH) retrieval and has been a critical mentor in focusing this research topic, ensuring that it was done well. Lt Col Wacker provided the foundation of my knowledge of satellite operations and applications. Finally, Dr. Kevin Gross initiated my interest in radiative transfer and served as a subject matter expert for infrared radiative transfer physics theory, in particular.

This undertaking would have been much more difficult without the University of Wisconsin Space Science and Engineering Center (SSEC) making intermediate (1 km) product data available on its NASA Atmosphere Science Investigator-led Processing System (SIPS) website. In addition, the high-quality instrumentation of the Department of Energy Atmospheric Radiation Measurement (ARM) Program was absolutely essential, and a proper system-level analysis would not have been possible without it.

Furthermore, Dr. S. C. (Steve) Ou and Dr. Stephen Warren provided the needed expertise for a proper comparison of VIIRS-calculated and ground truth cloud optical thicknesses. Finally, Ms. Barbara Iisager assisted with the decoding of cloud mask data, and Dr. William Bailey provided early computational knowledge.

Kyle E. Fitch

Table of Contents

Page

Abstract . . . iv

Acknowledgements . . . vii

List of Figures . . . x

List of Tables . . . xi

I. Introduction . . . 1

1.1 Motivation . . . 1
1.2 Cloud Base Height (CBH) Retrieval . . . 3
1.3 Research Topic and Objective . . . 6
1.4 Preview . . . 7

II. Background . . . 8

2.1 Previous Research . . . 8
2.2 Suomi NPP and VIIRS . . . 13
2.2.1 Suomi NPP . . . 13
2.2.2 VIIRS . . . 14
2.3 VIIRS CBH Retrieval Algorithm . . . 16
2.3.1 VIIRS Cloud Mask (CM) IP . . . 18
2.3.2 VIIRS Cloud Optical Properties (COP) IP . . . 21
2.3.3 VIIRS Cloud Top Parameters (CTP) IP . . . 26
2.3.4 VIIRS Parallax and Terrain Correction . . . 28
2.3.5 VIIRS Cloud Layer/Type (CLT) IP . . . 29
2.3.6 VIIRS Cloud Base Height (CBH) IP . . . 31
2.3.7 Validation of the VIIRS CBH IP . . . 36
2.3.8 VIIRS Data Maturity . . . 38
2.4 Atmospheric Radiation Measurement (ARM) Data . . . 39
2.4.1 Cloud Base Height (CBH) Retrieval . . . 40
2.4.2 Cloud Top Height (CTH) Retrieval . . . 41
2.4.3 Cloud Optical Property (COP) Retrieval . . . 43
2.5 Research Question and Objective . . . 45

III. Methodology . . . 46

3.1 Time Period and Location Selection . . . 46
3.2 Data Sources . . . 47
3.3 Evaluation . . . 49
3.3.1 VIIRS-ARM Site Match-ups . . . 49
3.3.2 Processing the Data . . . 49

3.3.2.1 Primary Daytime Method 49
3.3.2.2 Alternate Daytime Method 51
3.3.2.3 Nighttime Method 52
3.3.3 Test Scene Identification using False Color Images 52

IV. Results and Analysis 54

4.1 Initial Results 54
4.1.1 Daytime Results using Primary Method 54
4.1.2 Daytime Results using Alternate Method 58
4.1.3 Nighttime Results 62
4.2 Removal of Outliers 64
4.3 Analysis of the Upstream Cloud Products 70
4.3.1 CTH Analysis: CBH Sensitivity to CTH Error 70
4.3.2 COT Analysis: CBH Retrieval as a Function of COT 79
4.3.3 EPS Analysis: Replacing VIIRS EPS with Modal EPS Values 80
4.4 Findings and Discussion 81

V. Conclusion 84

5.1 Summary of Results 84
5.2 Recommendations for Future Research 85

Appendix. Acronym and Abbreviation List 86

Bibliography 91

Vita 99

List of Figures

Figure Page

1. VIIRS-CALIOP Comparison . . . 12
2. VIIRS CBH Processing Chain Diagram . . . 17
3. VIIRS CBH Algorithm Overview . . . 31
4. VIIRS False-color Image Example . . . 53
5. Correlations for CBH and CTH (Primary Daytime) . . . 54
6. Error (VIIRS - ARM) for CBH and CTH (Primary Daytime) . . . 55
7. Correlations for COT and EPS (Primary Daytime) . . . 56
8. Error (VIIRS - ARM) for COT and EPS (Primary Daytime) . . . 56
9. Correlations for CBH and CTH (Alternate Daytime) . . . 58
10. Error (VIIRS - ARM) for CBH and CTH (Alternate Daytime) . . . 59
11. Correlations for COT and EPS (Alternate Daytime) . . . 60
12. Error (VIIRS - ARM) for COT and EPS (Alternate Daytime) . . . 60
13. Correlations for CBH and CTH (Nighttime) . . . 62
14. Error (VIIRS - ARM) for CBH and CTH (Nighttime) . . . 63
15. CTH Outliers . . . 66
16. COD and EPS Outliers . . . 67
17. EPS Correlation Comparison . . . 68
18. CBH Correlation Comparison . . . 76
19. VIIRS CBH Error Plots . . . 78
20. VIIRS CTH Error Plots . . . 79

List of Tables

Table		Page
1.	VIIRS System Specification Requirements	14
2.	VIIRS Channels	15
3.	VIIRS Cloud Type Assignments	29
4.	VIIRS Liquid Water Content (LWC) Values	33
5.	S-NPP Data Maturity Definitions	39
6.	ARM Sites and Corresponding Data	48
7.	Daytime Statistics (Primary)	57
8.	Daytime Statistics (Alternate)	61
9.	Nighttime Statistics	64
10.	Daytime Statistics with Outliers Removed (Primary)	68
11.	Daytime Statistics with Outliers Removed (Alternate)	69
12.	Nighttime Statistics with Outliers Removed	70
13.	Daytime Subset	71
14.	Daytime Subset Results	72
15.	Daytime Subset (Corrected)	73
16.	Daytime Subset Comparison	73
17.	Corrected Daytime CBH Comparison (Primary)	75
18.	Corrected Daytime CBH Comparison with Outliers Removed (Primary)	75
19.	Corrected Daytime CBH (Alternate)	76
20.	Corrected Daytime CBH with Outliers Removed (Alternate)	77
21.	Corrected Daytime CBH by Optical Thickness	80

Table Page

22. Daytime Statistics using Modal EPS 81

EVALUATION OF THE VISIBLE INFRARED IMAGING RADIOMETER SUITE CLOUD BASE HEIGHT PIXEL-LEVEL RETRIEVAL ALGORITHM FOR SINGLE-LAYER WATER CLOUDS

I. Introduction

1.1 Motivation

Cloud base height (CBH) is an important factor for both aviation and climate research. The American Meteorological Society (AMS) Glossary of Meteorology defines cloud base to be "the lowest level in the atmosphere at which the air contains a perceptible quantity of cloud particles" (AMS Glossary, 2015b). For aviation, the height of the "ceiling" occurs where the lowest cloud layer obscures more than half of the sky (AMS Glossary, 2015a). Low ceilings often occur in conjunction with restricted visibility (e.g. fog), and a National Weather Service (NWS) study found that low ceilings and fog were contributing factors in 63% of all fatal accidents involving general aviation and small commuter aviation aircraft between 1995 and 2000 (Pearson, 2002).

For military aviation, in particular, the identification of cloud boundaries is useful for a wide range of weather-sensitive mission profiles. For example, the reduced visibility caused by cloud particles can be a limiting factor for in-flight refueling operations. Additionally, unmanned aircraft are known to be extremely sensitive to even the most benign aircraft icing conditions (Williams, 2004), and therefore, must be aware of cloud boundaries at altitudes where ice formation is possible. However, it is low cloud bases that greatly impact a wide variety of military operations, including takeoff and landing; air assaults; search and rescue, particularly in coastal and oceanic regions where sea stratus is prevalent; intelligence, surveillance, and reconnaissance; general low-level rotary flight, especially through narrow mountain passes; and close air support. Some mission impacts result from having to operate at unsafe altitudes to stay below such low cloud bases, which elevates risk and forces pilots to rely on aircraft instrumentation rather than visual cues, while other impacts result from a lack of cloud-free line of sight (CFLOS).

In terms of climate research, CBH is a significant parameter in determining the surface energy budget (Gupta, 1989; Berendes *et al.*, 1992; Forsythe *et al.*, 2000). Longwave radiation emitted by the surface of the earth is absorbed and re-emitted by clouds, as well as by water vapor, carbon dioxide, and other atmospheric gases. The amount of infrared radiation emitted to the surface by clouds depends primarily on the average temperature at cloud base, as shown by the Stefan-Boltzmann law for an approximate blackbody (which clouds are in the infrared) (Petty, 2006). Given that the average temperature of the emitting cloud layer depends strongly on its height, it is clear that more accurate CBH retrieval corresponds with a more precise surface energy budget determination. In fact, one study found that a 100-millibar (mb) uncertainty in CBH at the 650-mb level leads to surface errors of approximately 5 W m^{-2} (Gupta, 1989).

Currently, the most reliable method for retrieving CBH for a single location is from the surface, with lidar-exploiting ceilometers being the instrument of choice for civilian airports and military bases, alike. The primary limitation of the ceilometer is the lack of coverage across the earth, especially in remote, data-sparse locations. One way to overcome this limitation is to use the high-resolution, global data of polar-orbiting satellites. With the launch of the Suomi National Polar-orbiting

Partnership (S-NPP) satellite in 2011, the Visible Infrared Imaging Radiometer Suite (VIIRS) became "the first operational satellite sensor capable of retrieving three-dimensional cloud fields" (Hutchison *et al.*, 2006b), ultimately determining CBH from a single platform.

1.2 Cloud Base Height (CBH) Retrieval

While space-based retrieval of CBH is important for a wide range of applications, it is notoriously challenging to develop an algorithm that can provide accurate retrievals for the full gamut of cloud regimes (Liou, 1980; Welliver, 2009; Seaman *et al.*, 2014). The use of passive visible and infrared spectra to characterize cloud properties is limited by their inability to penetrate all but the most optically thin cloud layers (Lhermitte, 1988; Forsythe *et al.*, 2000; Welliver, 2009). Therefore, such algorithms rely on substantial parameterization, while exploiting reflectance and radiance information retrieved from the uppermost portion of the highest cloud layer (Liou, 1992). This has led some to explore cloud boundary detection using a combination of instruments.

Much effort in CBH retrieval has been focused on combining millimeter-wave cloud radar (MMCR) and micro-pulse lidar (MPL), especially with the launch of the CloudSat and Cloud-Aerosol Lidar and Infrared Pathfinder Satellite Observations (CALIPSO) satellites in April of 2006 (Welliver, 2009). CloudSat's primary instrument is the 94-GHz Cloud Profiling Radar (CPR), while CALIPSO hosts the Cloud-Aerosol Lidar with Orthogonal Polarization (CALIOP) instrument. The synergistic use of these instruments for cloud profile retrieval combines the ability of the CPR to penetrate thick cloud layers with the advantage of detecting thin cloud layers (e.g. thin cirrus) with the CALIOP lidar. CBH, then, is represented by the lower boundary of such a profile. A significant limitation of this approach is ground clutter bias in the lowest 500 m (Welliver, 2009). This low-level bias is undesirable for aviation, especially in remote, data-sparse locations where satellite data may be the only CBH information available.

The development of the Moderate-resolution Imaging Spectroradiometer (MODIS) and VIIRS instruments brought about a new generation of passive visible and infrared sensors that contained a wide range of spectral bands at very high resolution on a single platform. MODIS was developed and launched approximately 12 years before VIIRS, but the two instruments have many similarities. This allowed pre-launch testing of the VIIRS CBH algorithm using MODIS data; however, MODIS microphysical properties are only available during daytime, and the MODIS retrieval of cloud top height (CTH) is different than that of VIIRS (Hutchison, 2002).

Beginning in 1998 under the National Polar-orbiting Operational Environmental Satellite System (NPOESS) program, and leading up to the launch of the S-NPP in 2011, an algorithm for the retrieval of CBH using the VIIRS instrument was developed and ground tested (Hutchison, 1998; Hutchison and Wilheit, 2000; Hutchison, 2002; Hutchison *et al.*, 2006b). The basic idea of the algorithm is to subtract geometric cloud thickness (ΔZ) from CTH, where ΔZ is derived from parameterized equations that convert the cloud optical thickness (COT, τ) and effective particle size (EPS, r_e) to a geometric thickness (ΔZ) (Hutchison, 1998). This is done in the CBH intermediate product (IP), which uses other VIIRS cloud products' output as its input. VIIRS IPs serve as intermediaries between the sensor data records (SDRs), which are the calibrated and geolocated sensor (i.e., radiance and reflectance) data, and the lower-resolution environmental data records (EDRs) that serve as final cloud products for the end user. The CBH IP has a pixel-level, horizontal spatial resolution (HSR) of approximately 750 m at nadir and 1.6 km at edge of scan (EOS) (see Table 2 in Chapter II), giving an average HSR of approximately 1 km. On the other hand, the CBH EDR is the result of pixel aggregation and averaging and has a reduced resolution of approximately 6 km at both nadir and EOS (JPSS OAD for VIIRS CCL, 2013).

Calibration and validation (cal/val) of the VIIRS CBH retrieval algorithm by the National Aeronautics and Space Administration (NASA) Joint Polar Satellite System (JPSS) cal/val team has revealed some significant limitations. The CPR/CALIOP vertical profile product served as ground truth during cal/val, ignoring cases with precipitation and/or clouds below 1 km in order to compensate for errors in the CPR/CALIOP truth data at lower altitudes. The cal/val team reported that the algorithm consistently performed far better for single-layer, water-phase clouds than for any other cloud phase (Seaman *et al.*, 2014), which confirmed pre-launch expectations (Hutchison, 2002; Hutchison *et al.*, 2006b). Performance for water-phase clouds peaked at a correlation of 0.814 when CTH was within the VIIRS-required accuracy range of 1 km for optically thick clouds, and 2 km for optically thin clouds (see Table 1 in Section 2.2.1). When all cloud types were considered, the correlation was 0.595 when CTH was within the accuracy range. However, correlation dropped to 0.188 for all cloud types when CTH was not within this accuracy range. Due to the poor overall performance, a statistics-based replacement algorithm is currently being tested (Noh *et al.*, 2015). The new algorithm uses a CPR/CALIOP training dataset with linear regression to calculate a more accurate CBH, which was shown to outperform the existing algorithm. At the time of inquiry, the new algorithm was still being tested, with no planned, operational time frame reported.

1.3 Research Topic and Objective

Previous research in the spaceborne retrieval of CBH has relied upon using radar/lidar as ground truth. Even validation of the VIIRS CBH retrieval algorithm has been limited to a single, CPR/CALIOP-based approach for daytime pixels using satellite "match-up points." This is not unwarranted, as the CPR/CALIOP combination has proven to capture most cloud boundaries quite accurately. However, it has a clear bias in the lowest levels of the atmosphere, where CBH retrieval becomes critical for a majority of aviation operations. It is this low-level water-phase cloud regime, in the absence of overlap by upper-level cloud layers (i.e., cirrus), which performs best for the current VIIRS algorithm. This was shown by the VIIRS CBH cal/val team for daytime cases above 1 km and will be expanded below 1 km for both daytime and nighttime cases in this research.

While cal/val moves towards a statistics-based regression algorithm, relying heavily on the combined radar/lidar product, daytime and nighttime validation of the actual components of the existing VIIRS CBH algorithm and operational products being created at the NASA Interface Data Processing Segment (IDPS, i.e., ground station) is noticeably absent. No study has conducted a system-level analysis of the physical parameterizations and cloud product components that comprise the current algorithm. The primary objective of this research was to construct an algorithm error budget, by performing sensitivity analysis on each of the key components of the algorithm, in order to identify the largest sources of error. Specifically, VIIRS-calculated CBH, CTH, COT (τ), and EPS (r_e) were evaluated for single-layer water clouds against ground-based truth datasets from four Atmospheric Radiation Measurement (ARM) site locations, which provided the necessary precision for analysis. Retrieval comparisons were made for both daytime and nighttime conditions using the pixel-level IP, as opposed to the lower-resolution

EDR. After evaluating the error of these key components of the physical algorithm, future research can be focused to address the major sources of error.

1.4 Preview

The next chapter provides an overview of previous CBH retrieval research and the VIIRS CBH IP retrieval algorithm, as well as ARM instrumentation and associated algorithms. Methodology is presented in Chapter III, and results and findings are covered in Chapter IV. The final chapter summarizes the findings and provides recommendations for future research.

II. Background

2.1 Previous Research

Algorithm development for the space-based retrieval of CBH has been attempted since long before the launch of VIIRS on the S-NPP satellite. Given the importance of CBH retrieval for military operations, the Department of Defense (DOD) led the way in various early attempts at retrieving CBH. These early methods relied primarily on data from the Defense Meteorological Satellite Program (DMSP), conventional weather observations, or combinations of the two. The earliest known attempt can be traced back to the agency formerly known as the Air Force Global Weather Central (AFGWC) and its automated cloud analysis model (Fye, 1978), which later became the 3-Dimensional Nephanalysis (3DNEPH) Model. The 3DNEPH ran operationally at AFGWC beginning in 1970, until it was replaced with the Real-Time Nephanalysis (RTNEPH) Model in 1983 (Kiess and Cox, 1988; Hamill *et al.*, 1992). Both the 3DNEPH and the RTNEPH merged surface-based weather observations, and additional conventional weather observations, with satellite-based cloud products to generate a global CBH product (Hamill *et al.*, 1992). Since 2002, the 557th Weather Wing's Cloud Depiction and Forecast System II (CDFS II) has produced an hourly World Wide Merged Cloud Analysis (WWMCA) that employs geostationary and polar-orbiter imagery, as well as surface observations, and uses the RTNEPH technique to determine CBH (Horsman II, 2007). Due to limitations with the automated retrieval, CBH output often relies upon the climatological cloud thicknesses of 10 cloud types being subtracted from the CTH (Kiess and Cox, 1988). These early attempts relied heavily on climatology and surface-based observations to supplement the satellite data, which was a significant limitation for remote, data-sparse regions. Other early algorithms shared this limitation, or only applied to specific cloud types.

Another early approach by Berendes *et al.* (1992) used image processing techniques with Land Satellite (LANDSAT) imagery to match the edges of daytime cumulus clouds with their corresponding shadows. CBH was then approximated using the Generalized Hough Transform to determine the separation distance. Values calculated from this method were within 100 m (328 ft) of surface-based CBH observations; however, the approach assumes flat terrain, and LANDSAT views a given location on Earth's surface only once every 16 days. In another early approach, Forsythe *et al.* (2000) combined visible and infrared, satellite-derived cloud classification methods with surface observations to retrieve CBH for bases less than 10,000 ft (3,048 m). The study found an improvement over techniques that estimate CBH using only surface data interpolation, especially for broken and overcast conditions (Forsythe *et al.*, 2000). However, given the large extinction cross-section of cloud particles at these wavelengths, the inability of radiation to penetrate most cloud depths was a substantial drawback for these early, passive, visible and infrared algorithms.

Much progress has been made towards independent, space-based retrieval of CBH with active radar and lidar instrumentation, complementing each other in advantageous ways (Wang and Sassen, 2001). Micro-pulse lidar (MPL) struggles to penetrate thick low- and mid-level clouds, but is ideal for detecting relatively thin, mid- and high-level clouds that may be missed by radar. On the other hand, MMCR is able to penetrate thick cloud layers, but is often contaminated by virga, precipitation, and even insects. MMCR is also often unable to detect clouds with small particles, such as altocumulus, thin cirrus, or stratus (Wang and Sassen, 2001).

Lhermitte (1988) demonstrated the superiority of hydrometeor detection by ground-based MMCR over that of previously used centimeter-wavelength radar. While the higher-frequency MMCR is more susceptible to attenuation by water vapor, it is also more sensitive to hydrometeor reflectivity in the detection of cloud boundaries. Clothiaux *et al.* (1995) advanced the use of MMCR by developing an algorithm for cloud boundary height detection using power return statistics. The study highlighted the radar's ability to estimate both CTH and CBH for single- and multiple-layer clouds, simultaneously.

A significant drawback identified by both studies was the MMCR sensitivity to drizzle and precipitation, resulting in radar-determined CBH being substantially lower than ground truth comparisons (Lhermitte, 1988; Clothiaux *et al.*, 1995). Another limitation was the underdetection of optically thin clouds, such as thin cirrus (Clothiaux *et al.*, 1995). However, MPL can be used in conjunction with MMCR in order to overcome the latter limitation (Clothiaux *et al.*, 2008). A key skill of surface-based MPL during testing at the Southern Great Plains (SGP) ARM site was its superior detection of thin cirrus compared to that of the Belfort Laser Ceilometer (BLC) (Clothiaux *et al.*, 2008), which was the primary ceilometer at the ARM facilities from 1994-2000 (ARM BLC, 2015).

During initial testing of space-based lidar, known as the Lidar In-space Technology Experiment (LITE), it was found that "LITE profiles penetrated to an altitude of 1 km or less in 70% of all cloud cases" (Winker *et al.*, 2003). The success of this space-based testing led to the development of the CALIOP instrument on-board the CALIPSO satellite. The CALIOP sensor works by producing linearly-polarized pulses of light at 1.064 and 0.532 µm. The backscattered intensity at 1.064 µm, and the two orthogonal polarization components at 0.532 µm, are all measured by a 1-m telescope (Winker *et al.*, 2003).

Many scholars have since focused on a multi-instrument approach for space-based CBH retrieval that combines 94-GHz radar and MPL on the CloudSat and CALIPSO satellites of the NASA Earth Observing System A-Train constellation. The CloudSat and CALIPSO satellites were launched in April 2006, and the CPR and CALIOP instruments on-board these two synergistic platforms combine to provide highly accurate cloud profiling (Welliver, 2009). The result is the 2B-GEOPROF-Lidar (2GL) product, which combines data from each instrument "to provide a complete profile of the vertical structure of clouds in the atmosphere" (Welliver, 2009). However, the product is limited to a vertical (i.e. nadir) cross-section of the atmosphere along the satellite ground track, which limits both the horizontal footprint (shown in Figure 1) and temporal resolution of the product. The horizontal footprint is less than 100 m, and it views the same spot on the globe only once every 16 days.

A study similar to the one detailed in this paper compared CBH values from the 2GL product to CBH truth data at four different ARM sites (Welliver, 2009). However, rather than using only ceilometer data for truth values, a since-retired ARM CBH Value-Added Product (VAP) was used. VAPs are developed to derive important cloud properties from ARM site measurements. This VAP was the CBH portion of the Active Remote Sensing of Clouds (ARSCL) VAP, and it combined co-located 35-GHz MMCR, MPL, and Vaisala laser ceilometer data to derive best-guess CBH values at each ARM site. 2GL CBH values were considered to be "accurate" when they were within 480 m of the truth values, where 480 m is the vertical resolution of the CPR. Welliver found that CBH values were accurate 73% of the time. However, it was noted that the limited horizontal surface footprint and temporal resolution were significant drawbacks to any operational application of the product. Another substantial drawback was the "clear bias towards classifying

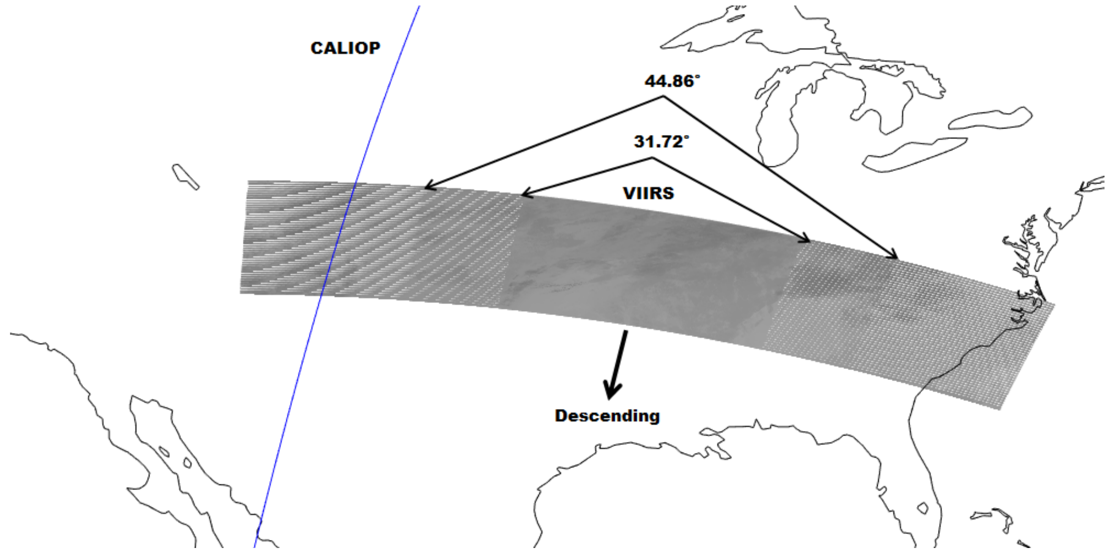

Figure 1. VIIRS-CALIOP Comparison. This figure shows the significant difference in the horizontal footprint of the CALIOP and VIIRS instruments. The CALIOP views only the vertical profile of the sub-satellite column, so the horizontal footprint is very small compared to that of VIIRS. The VIIRS swath is 3,000 km wide, and only one granule (48 scans) is shown here. VIIRS pixels undergo "bow-tie deletion" (explained in Section 2.2.2), which are seen as empty pixels when the ground track mercator projection is not used. These missing pixels begin to appear at a scan angle of 31.72 degrees, and double in size at 44.86 degrees.

hydrometeors detected in the lowest 500 m of the column as ground clutter" (Welliver, 2009). Error handling by the algorithm ignored the low-level feature altogether, which resulted in the algorithm consistently placing the CBH too high.

While the 2GL product of the CALIOP/CPR instruments is quite useful as a set of ground truth data in cloud boundary analysis, it lacks the footprint and temporal resolution needed for aviation operations support. Also, the shortcomings of the active radar/lidar approach in the near-surface limit are inherent in the MMCR wavelengths being employed and are difficult to overcome. Therefore, a return to passive visible and infrared instrumentation is necessary for low-level CBH accuracy, especially with the high resolution and advanced, hyperspectral sampling ability of the VIIRS instrument.

2.2 Suomi NPP and VIIRS

2.2.1 Suomi NPP.

The NPOESS was created in the early 1990s in order to consolidate "civilian and military environmental sensing programs and expertise under a single national system" (Lee *et al.*, 2006). The acquisition and management of the program for both the Department of Commerce (DOC) and DOD fell under a single organization, called the Integrated Program Office (IPO). The IPO, a tri-agency organization composed of DOC, DOD, and NASA personnel, established system-level requirements for all EDRs. Requirements for the VIIRS CBH EDR (see Table 1) were first described in the VIIRS Technical Requirements Document of 2000, and, after cancellation of the NPOESS program, were incorporated into the EDR requirements for the National Oceanic and Atmospheric Administration (NOAA) JPSS (JPSS REQ, 2013). These requirements remained the same as the NPOESS program evolved into the S-NPP.

The S-NPP satellite, formerly known as the NPOESS Preparatory Project (NPP), launched on October 28th, 2011 (NASA S-NPP Mission Page, 2015). The spacecraft resides at an altitude of approximately 824 km, has an orbital inclination of about 98.74 degrees, and a near-circular orbit with a period of about 101 minutes. The satellite has five sensors on board (NASA S-NPP Brochure, 2015). The Clouds and the Earth's Radiant Energy System (CERES) measures reflected solar and emitted infrared energy in order to compile a long-term record of the Earth's energy budget. The Cross-track Infrared Sounder (CrIS) and the Advanced Technology Microwave Sounder (ATMS) work together to provide "global high-resolution profiles of temperature and moisture," with the ability to create cross-sections of weather systems for both short- and long-term forecasting (NASA S-NPP Brochure, 2015). The Ozone Mapping and Profiler Suite (OMPS) measures

Table 1. VIIRS System Specification Requirements. Table adapted from Tables 5.3.1, 5.3.3, 5.3.6-5.3.9 in JPSS Level 1 Requirements document (JPSS REQ, 2013). The "threshold" is the required accuracy/uncertainty, while the "objective" is the desired accuracy/uncertainty.

Cloud Product	**Attribute**	**Threshold**	**Objective**
Cloud Base Height	Measurement Uncertainty	$\leq$ 2 km	$\leq$ 250 m
Cloud Top Height	Measurement Accuracy	2 km if COT $<$ 1 1 km if COT $\geq$ 1	$\leq$ 300 m
Cloud Top Temperature	Measurement Accuracy	6.0 K if COT $<$ 1 3.0 K if COT $\geq$ 1	2.0 K 1.5 K
Cloud Top Pressure	Measurement Accuracy (shown only for COT $\geq$1)	Surface - 3 km: 100 mb 3 - 7 km: 75 mb $>$ 7 km: 50 mb	10 mb 7 mb 5 mb
Cloud Optical Thickness (τ)	Measurement Accuracy	Greater of 24% or 1 τ	$\leq$ 5%
Effective Particle Size (r_e)	Measurement Accuracy	Greater of : 22% (water) or 1 µm 28% (ice) or 1 µm	$\leq$ 5%

and tracks ozone in the upper atmosphere and troposphere, improving air quality monitoring and extending a "40-year long record" of ozone measurement (NASA S-NPP Brochure, 2015). However, the VIIRS instrument on-board the S-NPP is the focus of this study.

2.2.2 VIIRS.

The VIIRS is a direct descendant of the MODIS, which flies on NASA's Terra and Aqua Earth Observing System satellites (NASA S-NPP Brochure, 2015). The sensor serves a wide range of scientific communities, providing radiometric data from 22 channels (see Table 2) that are used to observe clouds, aerosols, active fires, vegetation, ocean color, and sea surface temperature, among other surface features. VIIRS information is used for both short- and long-term forecasting, to include potential climate change.

Table 2. VIIRS Channels. Also shown are the corresponding central wavelengths and horizontal spatial resolution (HSR) (downtrack x crosstrack) at both nadir and edge-of-scan (EOS). Intermediate products (IPs) that use these channels as input are listed in the far right-hand column and include Cloud Mask (CM), Cloud Optical Properties (COP), and Cloud Top Parameters (CTP). This table is adapted from Table 1 in the VIIRS SDR User's Guide (Cao *et al.*, 2013), and from inputs listed in the JPSS Operational Algorithm Description (OAD) documents (VIIRS CM, 2015; VIIRS COP, 2013; VIIRS CTP, 2013). M-band channels are moderate resolution channels, I-band channels are imagery resolution channels, and the day-night band (DNB) is a panchromatic, solar reflective channel.

Channel #	Central Wavelength (μm)	HSR, Nadir (m)	HSR, EOS (m)	IPs
M1	0.412	742 x 259	1600 x 1580	CM
M2	0.445	742 x 259	1600 x 1580	
M3	0.488	742 x 259	1600 x 1580	
M4	0.555	742 x 259	1600 x 1580	CM
I1	0.640	371 x 387	800 x 789	CM
M5	0.672	742 x 259	1600 x 1580	CM, COP
DNB	0.700	742 x 742	800 x 789	
M6	0.746	742 x 776	1600 x 1580	
I2	0.865	371 x 387	800 x 789	CM
M7	0.865	742 x 259	1600 x 1580	CM
M8	1.240	742 x 776	1600 x 1580	COP
M9	1.378	742 x 776	1600 x 1580	CM
I3	1.610	371 x 387	800 x 789	
M10	1.610	742 x 776	1600 x 1580	CM, COP
M11	2.250	742 x 776	1600 x 1580	CM, COP
M12	3.700	742 x 776	1600 x 1580	CM, COP
I4	3.740	371 x 387	800 x 789	CM
M13	4.050	742 x 259	1600 x 1580	CM, COP
M14	8.550	742 x 776	1600 x 1580	CM, COP
M15	10.763	742 x 776	1600 x 1580	CM, COP, CTP
I5	11.450	371 x 387	800 x 789	CM
M16	12.013	742 x 776	1600 x 1580	CM, COP

The instrument uses a rotating telescope scan, extending to 56 degrees on either side of nadir (Cao *et al.*, 2013). Each VIIRS moderate-resolution band (M-band, see Table 2) has 16 detectors in the along-track direction, while the imagery-resolution bands (I-bands) have 32. At nadir, three detector footprints are aggregated to form a single VIIRS "pixel." The aggregation scheme transitions from 3x1 (downtrack x crosstrack) at nadir to 2x1 at around 32 degrees scan angle, and then to a 1x1 at around 48 degrees (see Table 2). The resulting swath width is approximately 3000 km.

Detector size and scan timing are designed so that no gaps are present between adjacent scans because "scan width at nadir is the same as the traveling distance of the sub-satellite point in one scan period" (Cao *et al.*, 2013). However, pixel growth occurs in both the along-scan and along-track directions, as the scan width increases from 11.7 km at nadir to 25.8 km at EOS. The result is scan-to-scan overlap beyond a scan angle of approximately 19 degrees, which is known as the "bow-tie" effect (Cao *et al.*, 2013). The overlap becomes apparent as it grows beyond the M-band pixel size at 31.72 degrees, and double the pixel size at 44.86 degrees (Cao *et al.*, 2013). In order to save downlink bandwidth, these duplicate pixels are not transmitted to the ground. This is referred to as "bow-tie deletion," and these deleted pixels are shown in Figures 1 and 4.

2.3 VIIRS CBH Retrieval Algorithm

Three VIIRS IPs use a total of 17 of the 22 channels (as shown in Table 2), in addition to ancillary data, to begin the VIIRS CBH processing chain (CM OAD, 2015; CBH OAD, 2013; COP OAD, 2013; CTP OAD, 2013). These first three IPs, the Cloud Mask (CM), the Cloud Optical Properties (COP), and the Cloud Top Parameters (CTP) IPs, compute cloud confidence, cloud phase, EPS (r_e), COT (τ), CTH, cloud top temperature (CTT), and cloud top pressure (see Figure 2). After parallax and terrain corrections are applied, these key parameters are then used as inputs for the Cloud Layer/Type (CLT) and CBH IPs to compute cloud type and CBH, respectively. More detailed information is available for each IP in the following sections, and at the S-NPP Science Documents page: http://npp.gsfc.nasa.gov/documents.html (accessed December, 2015).

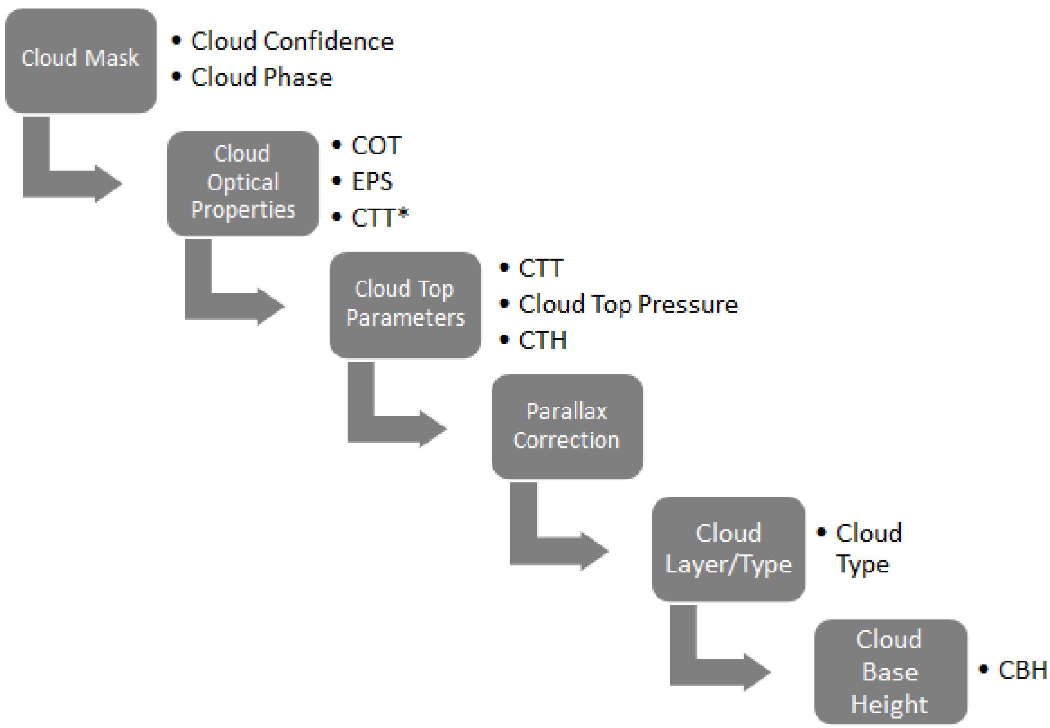

Figure 2. VIIRS CBH Processing Chain Diagram. VIIRS Intermediate Products (IPs) are processed in the order shown, with selected outputs indicated by the black text. Each IP (with the exception of CM) uses outputs from preceding IPs. Outputs of interest for this research include cloud confidence, cloud phase, cloud optical thickness (COT), effective particle size (EPS), cloud top temperature (CTT), cloud top pressure, cloud top height (CTH), cloud type, and cloud base height (CBH). CTT* is calculated in the COP IP only for the nighttime/IR processing path; otherwise, it is calculated in the CTP IP. Figure adapted from Figure 1 in Hutchison *et al.* (2006b).

2.3.1 VIIRS Cloud Mask (CM) IP.

Cloud confidence and cloud phase are both retrieved from the CM IP (JPSS VCM ATBD, 2014). Cloud confidence is the likelihood that each pixel is cloudy or not, and cloud phase is the physical state of the particles that make up the cloud. The CM IP takes in many inputs in addition to the calibrated and geolocated SDR data from the channels listed in Table 2.

Other VIIRS inputs include:

1. Gridded, 17-day Top-of-Canopy Normalized Difference Vegetation Index (TOC NDVI) IP
2. Moderate, pixel-level resolution, monthly gridded Snow Cover IP
3. Active Fires IP
4. 1-km Quarterly Surface Type IP

Gridding consists of mapping VIIRS swath data to a fixed external grid, while re-gridding involves mapping external gridded data (e.g. numerical weather model data listed below) to the VIIRS swath (JPSS Earth Gridding ATBD, 2014).

Non-VIIRS input includes the following numerical weather prediction (NWP) products:

1. Sea surface winds for determination of sun glint
2. Total precipitable water for thin cirrus determination over daytime desert backgrounds
3. Near-surface (i.e., 2-m) temperature for determining numerous brightness temperature thresholds

NWP sources include National Centers for Environmental Prediction (NCEP) Global Forecast System (GFS) and Navy Operational Global Atmospheric Prediction System (NOGAPS) data (JPSS CDFCB, 2014).

Before cloud tests are applied, background conditions are determined by choosing one of eight background domains: daytime land, daytime coast, daytime water, daytime desert, daytime snow/ice, nighttime land/desert/coast, nighttime water, and nighttime snow/ice. The domain depends on the input surface type from the VIIRS Quarterly Surface Type IP, and on snow/ice cover information from the gridded Snow Cover IP, as well as the solar zenith angle from the moderate-resolution geolocation data. A solar zenith angle of less than 85 degrees is considered to be daytime.

Next, a series of spectral and spatial tests are executed, depending on the background conditions (see Tables 5 and 6 in the JPSS VCM ATBD, 2014). Tests are placed in one of five independent groups according to the test type. Test types include emission threshold, emission difference, reflectance threshold, reflectance thin cirrus, and emission thin cirrus. More details on the determination of cloud confidence can be found in numerous publications (Hutchison *et al.*, 2005, 2008, 2012, 2014; Kopp *et al.*, 2014), and the JPSS VIIRS CM Algorithm Theoretical Basis Document (ATBD) (2014).

The final process in the CM IP that is most significant for CBH retrieval is the cloud phase determination, as described by Pavolonis and Heidinger (2004, 2005), and in the ATBD (JPSS VCM ATBD, 2014). Initially, the M15 brightness temperature (BT) is compared to CTT values in Table 20 in the ATBD, where a cloud is classified as a water cloud as long as the CTT is above freezing (i.e., 273.16 Kelvin (K)). Next, several tests are run to determine if cloud overlap is present, where cloud overlap is defined as a thin cirrus layer overlying a lower-level water cloud layer. Thin cirrus will contaminate the true BT of the water cloud if it goes undetected. The only way a cloudy pixel can be classified as liquid water phase is if the M15 BT is above the freezing threshold, and no overlying cirrus is detected.

This single-layer, water cloud phase is the only one considered in this research. A flow chart of the entire cloud phase algorithm can be found in Figure 28 of the ATBD, and details of the cloud phase tests are also found in the ATBD and aforementioned publications. These publications also cover differentiation between heavy aerosols and clouds (Hutchison *et al.*, 2008, 2010; JPSS VCM ATBD, 2014), as well as geometric-based cloud shadow detection (Hutchison *et al.*, 2009; JPSS VCM ATBD, 2014), as some algorithms in the CM IP are sensitive to cloud shadow and heavy aerosol contamination.

One major assumption of this IP is that all required inputs can be retrieved, which is a good assumption with the exception of rare cases of data retrieval errors. It also assumes that the surface type, snow and ice coverage, and NDVI databases are accurate and representative of the current, overall conditions of each individual pixel. This can be a poor assumption with rapidly changing background conditions, due to the relatively low temporal and spatial resolution of these databases. However, the snow/ice cover database is augmented in the daytime by an internal, pixel-resolution algorithm that performs spectral tests to determine the presence of snow or ice. It also assumes that the NWP weather model data used are accurate, which can be another poor assumption due to the relatively low, 1-degree spatial resolution. Finally, for cloud phase determination, it is assumed that the M15 (i.e., 10.763-µm) IR window channel BT is the same as the CTT. This is generally a good assumption, considering that water vapor and other atmospheric gases have very little effect on radiance in this window band, and that clouds are a good blackbody approximation at this wavelength. A significant limitation is evident during nighttime, when the lack of solar reflectivity data constrains the amount of information that can be gathered about cloud cover and cloud phase.

Accuracy of the CM IP is very important because all errors flow downstream to the other IPs, as shown in Figure 2. Probability of correct typing (PCT) is a measure of how often the algorithm correctly classifies a pixel as cloudy or clear (JPSS VCM ATBD, 2014). One study found that when CM IP data were compared to manually generated cloud masks, they had PCT values of 96.5%, 94.4% and 95.7% for ocean, land, and desert backgrounds, respectively (Hutchison *et al.*, 2014). This same study also found that PCT values were 95.0%, 93.9%, and 96.0% when compared to CALIOP-generated cloud masks with the same respective backgrounds. On the other hand, VIIRS cloud phase was only 83% accurate when compared to CALIOP-generated cloud phase (Heidinger, 2014), which agrees with ongoing cloud phase validation by Pavolonis (2014). This level of accuracy of cloud confidence and cloud phase is passed onto the next algorithm, the COP IP.

2.3.2 VIIRS Cloud Optical Properties (COP) IP.

Cloud microphysics, phase, particle shape, and particle size distribution all determine COP; and COP, in turn, affect emission, transmission, reflection, and absorption of radiation propagating through the atmosphere (Ou *et al.*, 2004). Cloud optical depth (COD, τ^*) is defined to be the total extinction optical thickness of all cloud layers in a vertical column of the atmosphere, shown below in Equation 1.

$$\tau^* = \Delta Z \int \sigma_e n(r) dr = \Delta Z \int Q_e \pi r^2 n(r) dr \tag{1}$$

In this equation, ΔZ is the geometric vertical distance between two levels of the atmosphere; $\sigma_e = Q_e \pi r^2$ is the extinction cross-section; Q_e is the extinction efficiency factor, and is a function of droplet radius, wavelength, and refractive index; r is the droplet radius; $n(r)$ is the cloud droplet number concentration as a function of radius; and dr is the increment across which the droplet size distribution is integrated.

COT (τ) is COD along an off-nadir, diagonal path through the atmosphere, and is related by the inverse cosine (i.e., secant) of the sensor scan (i.e., zenith) angle (θ). This is depicted mathematically in Equation 2 below and graphically in Figure 3 in Section 2.3.6.

$$\tau = \frac{\tau^*}{\cos(\theta)} = \tau^* \sec(\theta) \tag{2}$$

Additionally, τ and τ^* are wavelength dependent and assumed by the VIIRS COP IP to be measured in a narrow band centered on 0.450 µm.

EPS (r_e, i.e., mean effective radius) serves as a measure of the mean size of the cloud droplet size distribution, which determines the scattering properties of the distribution (Liou, 1992). It is defined to be the ratio of the 3rd and 2nd moments of the droplet size distribution, where the 3rd moment is the liquid water content (LWC, i.e., liquid water concentration), and the 2nd moment is the surface area concentration of the distribution (Ou *et al.*, 2004). This is shown mathematically in Equation 3 below,

$$r_e = \frac{\int r \pi r^2 n(r) dr}{\int \pi r^2 n(r) dr} \tag{3}$$

where r is the radius of each droplet, and πr^2 is the cross-sectional area of each droplet. In other words, EPS is essentially the simple mean radius weighted by the droplet cross section (Liou, 1992).

Four basic techniques are employed to retrieve both COT and EPS in the COP IP. In the daytime, one of two solar reflectance techniques is chosen for either ice or water clouds, using a two-channel correlation method for both water (Nakajima and

King, 1990; Ou *et al.*, 2004) and ice (Platnick *et al.*, 2003; Ou *et al.*, 2003, 2004) phases. These reflectances are compared to reflectance values listed in a comprehensive look-up table (LUT) to infer the COT and EPS. The LUT reflectance values are pre-computed using a line-by-line equivalent (LBLE) radiative transfer model (RTM) for a wide range of possible scenarios. For each scenario, an atmospheric profile, solar and sensor geometry, band parameters (e.g. spectral response), cloud phase and CTH are all specified. A value must be assumed for CTH because it has not yet been determined at this point in the process (discussed below). Also for each scenario, the RTM is run over a wide range of COT and EPS values.

For nighttime retrieval, IR radiance is used for both cloud phases, with a two-channel technique from Liou *et al.* (1990) and Ou *et al.* (1993; 2004), to infer CTT and IR emissivity. COT and EPS are then derived based on theory and parameterizations of radiative transfer and cloud microphysics.

VIIRS inputs include:

1. Calibrated, geolocated radiance and reflectance data
2. Viewing geometry and solar illumination
3. Cloud confidence and cloud phase from the CM IP
4. Surface albedo from the VIIRS Surface Albedo IP, for proper use of the solar reflectance LUTs
5. Surface type from the 1-km Quarterly Surface Type IP (Ou *et al.*, 2004)

Non-VIIRS inputs are used for pre-processing only, and are not used operationally. They are used to compute *a priori* LUT values, to be referenced later by the algorithm while it's in operation. These include:

1. Atmospheric NWP soundings, for construction of the reflectance LUTs and running the LBLE RTM

2. A spectral library containing reflection and emission properties for various surface types, which are used to create the LUTs
3. Exo-atmospheric, solar, spectral irradiance values, for conversion of radiance to bi-directional reflectance factors for the LUTs
4. VIIRS band parameters for deriving single-scatter properties and reflectance LUTs
5. CTH, which must be assumed (hasn't been calculated yet) for computation of the LUTs for the solar algorithms; 1 km is assumed for water clouds, and 10 km for all others (all other phases are considered in a single, "ice" cloud phase processing path for this IP)

The daytime retrieval method uses M10 reflectance with M8 reflectance over snow or ice surfaces, and it uses M10 with M5 reflectances over non-snow/ice surfaces (Ou *et al.*, 2004). The approach is relatively simple for water clouds, where properties for these solar channels are computed using classic Mie scattering theory for water droplets. In the water phase retrieval method, sun-sensor geometry parameters are first determined for each pixel, which include the solar zenith angle, the sensor viewing zenith angle, and the relative azimuth angle. Surface albedo is assigned based on the surface type. Reflectance arrays are then constructed for each combination of water droplet EPS and COT, as well as for each VIIRS channel used (i.e., M5, M8, and M10). Numerical iteration is executed, as described in Appendix B of the COP ATBD (Ou *et al.*, 2004), to find the LUT reflectances in the arrays that best match the measured reflectances. Computing optical properties for the myriad of ice particles is much more complex. Additional details on this ice phase approach can be found in the COP ATBD (Ou *et al.*, 2004).

Conversely, the IR nighttime method uses radiances at M12, M14, M15, and M16 to infer CTT and IR emissivity. Specifically for water clouds, only the M12 and M15 window channels are used, where water vapor has very little effect. Nine particle size distributions were used to calculate the regression coefficients for this two-channel correlation method. Clear-sky radiances were calculated using the Pressure-layer Fast Algorithm for Atmospheric Transmittances (PFAAST) RTM described in Appendix C of the COP ATBD (Ou *et al.*, 2004). The correlated k-distribution radiative transfer (RT) equations of Kratz (1995), coupled with microphysical parameterizations, are used to numerically solve for CTT and channel-specific emissivities. The emissivities are parameterized in terms of visible COT, so an inversion method is used to solve for COT once the emissivities have been calculated (Liou *et al.*, 1990). EPS can then be solved for as a function of COT and liquid water path (LWP), as shown in Equation 7 in Section 2.3.6. A cloud thickness must be assumed for this parameterization, so a value of 1 km was chosen. A climatological LWC value, expressed in terms of CTT, is also used (Ou *et al.*, 2004).

In addition to the assumptions already listed for this IP, standard RT assumptions apply. These include the plane parallel approximation, the single layer assumption (i.e., multi-layer clouds are not considered), hydrostatic equilibrium, and local thermodynamic equilibrium. These are all good assumptions for the spatial scales and portion of the atmosphere being considered. Furthermore, mixed-phase clouds are treated as ice clouds (e.g. CTH assumed to be 10 km for mixed-phase clouds), and situations where the clear radiance is less than the cloudy radiance (e.g. polar winter) are not considered. For ice-phase clouds, size distributions are based on *in situ* observations from field experiments that were conducted primarily in the mid-latitudes. Ice crystals are assumed to be randomly oriented, and the only habits considered are solid columns and plates. Scattering by ice crystals is highly complex, and the COP IP approach uses a Monte Carlo ray-tracing method with a "unified theory" for an approximate solution (Ou *et al.*, 2004). Such significant assumptions make it much more difficult to accurately determine COT and EPS for ice clouds.

Validation was performed by comparing daytime VIIRS COT and EPS retrievals to MODIS and NOAA cloud products, as reported in the VIIRS Cloud Products Beta Maturity Status Report (CPBMSR) (2013). These retrievals were found to be within the required specification range of Table 1 68% of the time for COT and 64% of the time for EPS. However, these comparisons could only be made when VIIRS CM and cloud phase matched that of the NOAA cloud products. Snow- and/or ice-covered surfaces were ignored, as well. For nighttime retrieval validation, indirect comparisons were made "based on the cloud emissivity data generated by the MODIS cloud top products" (VIIRS CPBMSR, 2013). This method exploited the fact that COT is related to cloud emissivity using the sensor zenith angle and scattering effects. Using this method, it was determined that nighttime retrieval of COT was within the required accuracy range approximately 40% of the time.

As mentioned in the processing chain diagram in Figure 2 and in this section, CTT is computed only for the nighttime/IR processing path. If the daytime/solar processing path is used, CTT is computed in the following CTP IP.

2.3.3 VIIRS Cloud Top Parameters (CTP) IP.

The CTP IP uses VIIRS radiance, other IP data, and ancillary atmospheric profiles from NWP to estimate CTT, CTH, and cloud top pressure (JPSS CT, 2012). Two processing paths are used: one for daytime water (DW) clouds, and another for all other conditions, called non-day-water (NDW) .

For DW, an iterative process is used to minimize the difference between the observed M15 (10.763 µm) radiance and radiance produced by a fast RTM (JPSS

CT, 2012). The RTM uses ancillary NWP profiles of temperature and moisture as inputs, as well as COT, EPS, NWP near-surface temperature, and surface emissivity. Moisture profiles from the NWP source (e.g. NCEP GFS) are used to account for the amount of water vapor absorption above the cloud top. The atmosphere is nearly transparent for the M15 band, but some attenuation occurs due to absorption by water, carbon dioxide, and aerosols. Therefore, optically thick water clouds are very close to being blackbodies, and most of the upwelling radiation at cloud top is from the cloud itself. Conversely, most of the radiation from a clear scene will be from the ground. Optically thin clouds will result in a mixture of ground and cloud radiation because not all of the ground radiation is absorbed by the cloud. In this DW method, cloud top pressure is derived first, then CTT and CTH by interpolating from the ancillary soundings. Interpolation is accomplished through one of two methods: the Newton-Raphson iteration, or the "Search" method when convergence is a problem with the former method. More details on these interpolation methods can be found in the ATBD (JPSS CT, 2012).

If the COP IP process described in Section 2.3.2 should fail (e.g. required inputs are missing or degraded) in the daytime, this DW method can be used as a backup COT/EPS retrieval method. In this backup mode, the cloud is assumed to be optically thick, allowing the COP values to be approximated by BT using a correction for water vapor above the cloud top (from NWP profile) (JPSS CT, 2012).

For NDW clouds, the CTT derived from the COP IP in Section 2.3.2 is used to determine the CTH by linearly interpolating from an ancillary NWP temperature sounding (Rossow *et al.*, 1991). Cloud top pressure is also interpolated from a NWP sounding using the hypsometric equation.

Standard RT assumptions apply here, much like with the COP IP methodology in Section 2.3.2 (JPSS CT, 2012). This set of assumptions includes the single cloud layer assumption, which is valid for the cases included in this study. Of particular importance is the hydrostatic assumption for CTH and cloud top pressure interpolation, where pressure is assumed to decrease exponentially. This is a good assumption for all vertical spatial scales except for severe convection, which is not included in the set of cases for this study. Furthermore, general standard atmospheric temperature profile characteristics are assumed, i.e., temperature decreases monotonically (JPSS CT, 2012). Therefore, temperature inversions and isothermal layers can be problematic. Finally, sub-pixel clouds are ignored (i.e., it is assumed that the entire pixel is cloudy if the pixel is determined to be confidently cloudy in the CM IP) (JPSS CT, 2012), so cloud types with little spatial extent in the horizontal, such as fair weather cumulus, will be susceptible to errors.

Performance of the CTP IP has been validated by matching CTT and CTH values with truth values derived from the CALIOP product suite, and by comparing cloud top pressure to MODIS "truth" values (Heidinger, 2014). Accuracy was defined according to the specification requirements listed in Table 1, and a COT filter for $\tau > 1$ was applied using the CALIOP COT product. CTT had the lowest accuracy at 47.6%, CTH was 73.2%, and cloud top pressure was the most accurate at 82.9%.

2.3.4 VIIRS Parallax and Terrain Correction.

Parallax correction is performed for CM, COP, and CTP outputs, while terrain correction is performed for the geolocation data. The purpose of parallax correction is to adjust for the apparent displacement of a tall feature (e.g. cloud) away from the satellite subpoint as the sensor viewing angle becomes large (i.e., off-nadir angle increases) (Kidder and Vonder-Haar, 1995). The algorithm uses the CTH, satellite position, and cloud position to make the correction (JPSS OAD for PPC, 2013). A similar correction is also made for terrain, where high terrain needs the same adjustment that a cloud would need at the same large viewing angle (Cao *et al.*, 2013). The parallax-corrected CM, COP, and CTP IPs, and the terrain-corrected, moderate resolution geolocation files are used in this study.

2.3.5 VIIRS Cloud Layer/Type (CLT) IP.

Last in line prior to CBH computation, the CLT IP uses an adapted, k-means clustering algorithm to determine the extent, type, and physical characteristics of vertically distributed cloud layers. The k-means algorithm is "an established mathematical method for clustering points into groups with similar properties" (MacQueen, 1967; Selim and Ismail, 1984; Theiler and Gisler, 1997; JPSS VIIRS CCL ATBD, 2011). Pixels with high statistical similarity are grouped together within a single "cluster," and unique physical attributes within a cluster/layer are used to identify the cloud type according to Table 3 below (JPSS VIIRS CCL, 2011). Each pixel is assigned to a cloud layer, where up to four layers are possible with this algorithm.

Table 3. VIIRS Cloud Type Assignments. Predefined cloud types characterized in terms of their macro (height and phase) and micro (EPS/COT) properties. Table adapted from Table 12 in JPSS VIIRS CCL (2011), and is a combination of observations from numerous studies (Weickmann and Aufm-Kampe, 1953; Heymsfield and Platt, 1984; Dowling and Radke, 1990; Liou, 1992).

Cloud Type	Height (km)	EPS (μm)	COT	Phase
Stratus (ST)	< 2.5	2-25	1-10	Water
Alto-cumulus/-stratus (AC, AS)	1.5-5.5	4-30	2-32	Water/Ice
Cumulus (CU)	0.2-6.5	5-50	3-50	Water/Ice
Cirrus (CI)	6-12	10-100	0.01-5	Ice
Cirrocumulus (CC)	6-15	30-120	1-8	Ice

The major assumption with this algorithm is that the values listed in Table 3 are accurate and all-inclusive (JPSS VIIRS CCL, 2011). While the data used to compile this table are varied and robust, they may not be representative of all cloud types observed globally. For example, much of the data for the table were gathered in the mid-latitudes and tropics, so these cloud types are more likely to be erroneous near the poles. To date, the cloud type output from this particular IP has not been validated by the VIIRS cal/val team, so the amount of potential CBH error resulting from cloud type misclassification is unknown.

2.3.6 VIIRS Cloud Base Height (CBH) IP.

The CBH IP focuses on calculating geometric cloud thickness, as the CTH is retrieved externally from the CTP IP. CBH is calculated for every confidently cloudy pixel, as identified in the CM IP, and the applicable algorithm is chosen based on cloud phase (JPSS OAD for CBH, 2013). The water phase CBH algorithm is for all water clouds, while the mixed phase algorithm covers all ice, mixed, and overlap cloud phases. For both phase algorithms, geometric cloud thickness ($\triangle Z$) is subtracted from CTH (see Figure 3), but the parameterization of cloud thickness is different for each phase (Hutchison, 1998).

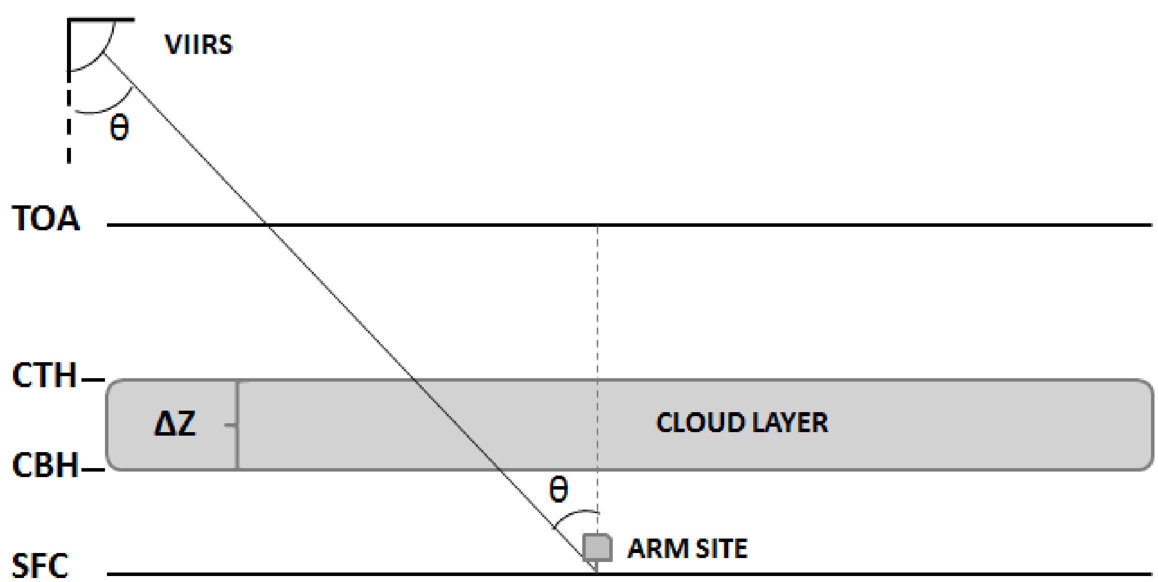

Figure 3. VIIRS CBH Algorithm Overview. Top-of-Atmosphere (TOA) radiance and reflectance sensed by the VIIRS allows for the parameterization of cloud geometric thickness (ΔZ) using COT, EPS, LWP/IWP, and LWC/IWC. ΔZ is then subtracted from CTH to estimate CBH. Sensor zenith angle (i.e., scan angle, θ) is related to the nadir-viewing ARM sensors at the surface. Figure adapted from Hutchison *et al.* (2006b).

For water clouds, COT (τ) and EPS (r_e) are related to the cloud's geometric thickness (ΔZ) using the ratio of LWP and LWC, both of which were mentioned briefly in Section 2.3.2. LWC is the integration of cloud droplet size distribution over droplet size (Hutchison, 1998), while LWP is defined as the vertical integration of LWC across cloud thickness. Both are shown mathematically in the following equations:

$$LWC = \frac{4\pi\rho_l}{3} \int r^3 n(r) dr \tag{4}$$

$$LWP = \int_{CBH}^{CTH} LWC\, dz = \Delta Z \frac{4\pi\rho_l}{3} \int r^3 n(r) dr \tag{5}$$

where ρ_l is the density of liquid water, and the LWC is assumed to be constant throughout the vertical extent of the cloud. This is approximately the case for thin stratus clouds, but not for thick stratus or cumuliform.

For spherical, liquid cloud droplets and solar/visible wavelengths, the extinction efficiency factor (Q_e) in Equation 1 (Section 2.3.2) is very close to two. Using Equations 1, 3, and 5, LWP can be solved for in terms of τ and r_e as shown by Liou (1992), and in Equations 6 and 7 below. Next, the ratio of LWP to LWC is used to determine the geometric thickness in Equation 8:

$$\frac{LWP}{\tau} \approx \frac{\Delta Z \, \frac{4}{3}\rho_l \int r\pi r^2 n(r) dr}{2\Delta Z \int \pi r^2 n(r) dr} \tag{6}$$

$$LWP \approx \frac{2 \cdot \tau \cdot r_e}{3} \tag{7}$$

$$CBH = CTH - \triangle Z = CTH - (\frac{LWP}{LWC} \times \frac{1\,km}{1000\,m}) \tag{8}$$

where ρ_l is 1 g cm^{-3}, τ is unitless, r_e is in µm, CTH is in km, LWP is in g m^{-2}, and LWC is in g m^{-3}. The ratio of LWP and LWC is divided by 1000 to convert m to km, and the final value of CBH is in km above mean sea level (MSL) (JPSS OAD for CBH, 2013). LWC is a constant, climatological value based on the input cloud type from the CLT IP, and is determined from "*a priori* information on the cloud particle size distributions and cloud type" (Hutchison, 1998). These LWC values are stored in a LUT and are based on Table 4.2 in Liou (1992), which summarizes measurements from numerous studies. However, the actual values of LWC differ slightly from those in Liou due to the small differences in cloud type classification. The values used by the VIIRS algorithm are shown in Table 4 below.

Table 4. VIIRS Liquid Water Content (LWC) Values. LWC values as a function of cloud type used in the VIIRS CBH algorithm (Hutchison, 1998; JPSS OAD for CBH, 2013). Only the top three cloud types (i.e., water clouds) are used for this analysis.

Cloud Type	LWC (g m^{-3})
Stratus (ST)	0.293
Altocumulus (AC)	0.455
Cumulus (CU)	0.580
Cirrus (CI)	0.010
Cirrocumulus (CC)	0.010

For the mixed phase processing path, LWP is replaced by ice water path (IWP), and LWC is replaced by ice water content (IWC). Again, Liou (1992) showed that IWP is a function of τ through the ice crystal size distribution, and ice crystal diameter ($D_e = 2 \cdot r_e$), as shown in Equation 9. Regression coefficients (a, b, $c_0 - c_3$) in Equations 9-12 are given in Table 5.4 of Liou (1992).

$$IWP = \frac{\tau}{\frac{a+b}{D_e}} \tag{9}$$

$$\ln(IWC) = -7.6 + 4\exp^{term} \tag{10}$$

$$term = [(-0.2443 \times 10^{-3})(|T_c| - 20)^{2.455}]\ for\ |T_c| > 20\,°C \tag{11}$$

$$D_e = c_0 + c_1 T_c + c_2 T_c^2 + c_3 T_c^3 \tag{12}$$

In these equations, IWP is in g m^{-2}, D_e is in µm, IWC is in g m^{-3}, and T_c is the mean cloud temperature in $°C$, based on the CTT and COT (Hutchison, 1998). Only T_c values of -20 to $-60\,°C$ are used, since ice clouds generally do not fall outside this range (Hutchison, 1998). If $T_c < -60\,°C$, the value is reset to $-60\,°C$, and if $T_c > -20\,°C$, the value is reset to $-20\,°C$. Additional details on the mixed/ice phase portion of the algorithm can be found in the VIIRS CBH ATBD (Hutchison, 1998), but water clouds are the focus of this research.

Many assumptions and limitations exist for the CBH IP algorithm that have not yet been highlighted in the preceding IP algorithms. A general assumption is that all upstream IP and ancillary data that serve as inputs to the CBH IP are accurate and available. This assumption is most significant for the CTH input, which is directly related to the accuracy of CBH. The accuracy of CBH can be no more accurate than CTH, as this value is what the parameterized ΔZ is subtracted from, as shown in Figure 3 and Equation 8. In fact, validation of CTH has demonstrated an accuracy of only 73%, as discussed in Section 2.3.3. It is also assumed that the LWC or IWC is constant throughout the cloud layer, which only holds for thin stratiform-type clouds (Hutchison *et al.*, 2006b). Therefore, thick stratus, cumuliform, and cirrus-type clouds are expected to be less accurate.

A primary limitation of the CBH IP is that there is a maximum COT value for which CBH can be accurately computed, which was determined during algorithm development to be approximately 64 for water clouds and 10 for ice clouds (Hutchison, 1998; Ou *et al.*, 2004). Beyond these values, the information that can be extracted from the data is extremely limited, which makes the retrieved CBH unreliable. However, these limits are still being investigated. One study found the maximum usable COT value for water clouds to be closer to 40 (Welch *et al.*, 2008). Furthermore, CBH is not retrieved if any of the following occur:

1. The pixel is not confidently cloudy
2. Cloud phase is anything other than water, opaque ice, cirrus, mixed, or overlap

3. Cloud type is outside the definition range of stratus, altocumulus/altostratus, cumulus, cirrus, or cirrocumulus (see Table 3)
4. The cloudy layer is outside the range of reasonable values, as stated in the CLT Operational Algorithm Description (OAD) (JPSS OAD for CCL, 2013)
5. The pixel is determined to be in an area affected by “bow-tie” deletion (described in Section 2.2.2)
6. COT, EPS, or CTH contain “fill values” for various errors (i.e., retrieval failed for any one of these critical parameters)
7. For ice, mixed, or overlap phases, CTT retrieval failed (i.e., contains a “fill value”) (JPSS OAD for CBH, 2013)

2.3.7 Validation of the VIIRS CBH IP.

Prior to the launch of the S-NPP spacecraft, data from the MODIS on-board the Terra Earth Observing System satellite were used for initial validation of the CBH retrieval algorithm to be used with the VIIRS instrument (Hutchison, 2002). MODIS, as the primary predecessor instrument to VIIRS, contains many of the same channels; however, MODIS calculates CTH using different channels than that of VIIRS, so collocated radiosondes were used to manually determine the CTH, as CloudSat wasn't launched until 2006. Therefore, only the geometric thickness (ΔZ), which is the heart of the CBH algorithm, was validated. Initially, daytime MODIS data were used for the simulated VIIRS COT and EPS retrieval, since MODIS does not retrieve these microphysical parameters at night. Test scenes were limited to single-layer water cloud systems, the condition for which the algorithm was predicted to perform most accurately. Such scenes were identified over Texas, where the Terra spacecraft descends at approximately 17-18Z. Therefore, overflight of the spacecraft occurred five to six hours after the collocated 12Z radiosondes, so cloud fields had to persist for this period of time. Nearby surface reports using lidar ceilometer measurements were used as ground truth CBH data. Due to the stringent requirements for test scenes, Corpus Christi, Texas, was the only location with useful validation data. Analyses were performed for approximately 225 individual pixels within 0.25 degrees latitude and longitude of Corpus Christi. It was found that the algorithm-calculated, geometric cloud thickness (ΔZ) was 89 m (292 ft) more, or 36% larger than, the ground truth thickness. A similar evaluation was performed for nighttime data using MODIS with ARM MMCR truth data (Hutchison *et al.*, 2006b). This study also found the VIIRS-calculated thickness values to be well within the system specification thresholds listed in Table 1.

A post-launch validation study was conducted for the VIIRS CBH EDR by the Center for Satellite Applications and Research (STAR) JPSS Science Team for their 1st annual team meeting in 2014 (Seaman *et al.*, 2014). For truth data, the team used the CloudSat CPR, the instrumentation of which has known limitations when detecting clouds in areas of significant ground clutter or precipitation. The S-NPP and CloudSat spacecrafts are in the same orbital plane at different altitudes, and they overlap for approximately four and a half hours every two to three days (Seaman *et al.*, 2014). Test cases were limited to daytime events where no precipitation was occurring. To prevent ground clutter issues, only the closest, usable VIIRS pixels that overlapped CloudSat, and had CBH and CTH beyond 1 km above ground level (AGL), were used. Nine total match-up periods were examined during September, 2013.

Results were organized into two categories: the first for all clouds, which consisted of all cases observed simultaneously by CloudSat and VIIRS; and the second for only those cases where VIIRS CTH was within specification requirements (Table 1). This second category was used due to the fact that CBH accuracy is closely tied to CTH accuracy. For the first category, the overall r^2 correlation was 0.188, with water clouds being the best and overlap conditions being the worst. When the CTH was within specification, the overall correlation increased to 0.595, with water clouds the best at 0.814 and overlap the worst at 0.181.

The VIIRS CBH calibration and validation team presented initial results for an improved, statistics-based algorithm at the 2015 Annual STAR JPSS Science Team Meeting (Noh *et al.*, 2015). Linear regression was performed between the MODIS cloud water path product and geometric thickness of the uppermost layer from Afternoon Train ("A-Train") constellation data. Specifically, the 2GL product was used, as described in Section 2.1. The regression method used CTH bins of 2 km up to a maximum of 20 km. The median water path value was determined for each 2-km CTH bin, and linear regression was carried out both above and below this value. This method was initially applied to July daytime data from 2007 to 2010, in order to develop a training dataset. When applied to match-up points from September to October 2013, the r^2 correlation increased from 0.286 to 0.427 for all valid cloud cases, and from 0.452 to 0.760 when the CTH was within specification.

2.3.8 VIIRS Data Maturity.

With the S-NPP satellite only recently launched in late 2011, data needed time to mature as the cloud products underwent cal/val. By mid-2013, the VIIRS CM product was at the provisional level of maturity (see Table 5), while all other VIIRS cloud products had been lumped together as beta (S-NPP Data Maturity, 2015). However, some of the cloud products were closer to provisional status than others; the CBH and nighttime COP products were lagging behind the others in their performance (VIIRS Beta Status Report, 2013). All products had reached provisional maturity status by January 2014, and nearly all reached the validated level by September 2014. The two exceptions are the CLT and nighttime COP algorithms, which currently remain in provisional status (JPSS Algorithm Maturity, 2015).

Table 5. S-NPP Data Maturity Definitions. From S-NPP EDR Product Maturity Levels web page (2015).

Level	Description
Beta	Early release, minimally validated product, which may still contain significant errors
Provisional	Incremental product improvements still occurring, and product quality may not be optimal
Validated	Product performance well defined over a range of representative conditions, but there may still be later, improved versions; three stages of maturity exist

2.4 Atmospheric Radiation Measurement (ARM) Data

The Department of Energy (DOE) ARM Program operates and maintains "some of the most sensitive instruments available" for observing the presence, extent, and radiative properties of clouds (Ackerman and Stokes, 2003). The central facility at Lamont, Oklahoma (OK), of the Southern Great Plains (SGP) site, is the premier facility, but other permanent locations include the Tropical Western Pacific (TWP), North Slope of Alaska (NSA), and Eastern North Atlantic (ENA) (ARM Annual Report, 2015). Mobile sites have also been established, temporarily, at numerous locations around the globe. Datastreams consist of calibrated instrument measurements, as well as post-processed data used in many different algorithms. For example, Value-Added Products (VAPs) are used to derive important cloud properties from ARM site measurements (ARM Annual Report, 2015). Ceilometer measurements and output from two different VAPs were used as ground truth data for this system-level analysis.

2.4.1 Cloud Base Height (CBH) Retrieval.

The primary instrument for CBH measurement at the ARM sites, and the source of ground truth for CBH in this research, is the Vaisala Ceilometer (VCEIL). The VCEIL is a "self-contained, ground-based, active, remote sensing device designed to measure cloud-base height, vertical visibility, and potential backscatter signals by aerosols" (Morris, 2012). A laser ceilometer transmits near-infrared (NIR) pulses of light, and its receiver detects the backscattered light from clouds and precipitation. This basic concept is known as lidar, more generally. Model CL31 is the latest version being employed, and it has a maximum vertical range of 7700 m (25,262 ft). It also has a vertical resolution of 10 m (33 ft). The transmitter is a pulsed indium gallium arsenide (InGaAs) diode laser with a wavelength of 910 nanometers (nm), and the receiver is a silicon avalanche photodiode. Primary output variables are backscatter intensity, CBH for the three lowest layers detected (in m AGL), and vertical visibility in m. An important secondary variable is time, in seconds (s), and numerous data quality flags are included, as well. Additionally, accuracy is ± 5 m, the measurement interval is 2 s, and the reporting interval is 16 s.

The measurement is a lidar technique based on "the time needed for a short pulse of light to traverse the atmosphere from the transmitter of the ceilometer to a backscattering cloud base and back to the receiver of the ceilometer" (Morris, 2012). In order to attain the 10 m vertical resolution, the ceilometer digitally samples the return signal every 67 nanoseconds from 0 to 50 microseconds. This resolution is assumed to be adequate, as 10 m is the approximate visibility in the densest of clouds (Morris, 2012). The constant of proportionality between the backscatter and extinction is known as the Lidar Ratio, which normally varies from 0.02 (for high humidities) to 0.05 (for low humidities). This assumption is known to be accurate for the purposes of cloud detection (Morris, 2012).

2.4.2 Cloud Top Height (CTH) Retrieval.

CTH ground truth is obtained at each ARM site using a micro-pulse lidar (MPL), 30-s cloud mask algorithm developed at the University of Utah (Wang and Sassen, 2001). The algorithm is applied to backscattered radiation of the MPL in 30-s samples in order to detect cloud boundaries and other properties between 500 m and 20 km (Sivaraman and Comstock, 2011). The algorithm cannot be applied below 500 m because of the overlap between the receiving and transmitting systems at these heights (Wang and Sassen, 2001; Sivaraman and Comstock, 2011). A series of lidar-specific corrections is applied, including range-square, background, deadtime, and overlap corrections, as described in the literature (Campbell *et al.*, 2002; Sivaraman and Comstock, 2011).

The algorithm is executed in five basic steps, described below (Wang and Sassen, 2001):

1. In the first step, the signal slope, signal quality, and standard deviation of the background noise level are all calculated. The signal slope and variation "are calculated for the whole profile, and a minimum reliable signal P_{min} is defined for lidar data with a given signal-averaging scheme" (Wang and Sassen, 2001).
2. The second step involves examining the signal from the ground up to determine possible layers and their properties, which include the base, top, and peak signal of the layer. The base is defined as the location "where the signal starts to increase in terms of the positive signal slope," while the top is "the altitude at which the signal slope returns to the slope of the clear-sky signal or the signal magnitude drops below P_{min}" (Wang and Sassen, 2001). The clear-sky signal is calibrated below the layer base by assuming no aerosol is present. The ratio of the peak signal to that of the layer base (T) and the maximum negative slope (D) are two other properties for each layer that are

also used in the algorithm (Wang and Sassen, 2001). In this second step, it is noted that the "layer" could be cloud, aerosol, precipitation, virga, or simply a noise peak. Therefore, certain range-corrected signals are used for low-cloud detection. Additionally, if the signal-to-noise ratio (SNR) is above a given threshold, then the D value within 500-800 m of the layer top is found. The layer top height is then searched again starting from this D value height, which addresses cases of cloud layers with multiple signal peaks.

3. For the third step, cloud is distinguished from aerosols and noise. Clouds are much more dense than aerosols at a given altitude, so an altitude-dependent threshold for the T value can be used to distinguish aerosols and clouds. Dense low clouds can sometimes have a small T value (i.e., indicating aerosol), though, so a D value threshold is used in these cases. If signal variation is high, but T and D values are small, this is indicative of a noise layer.
4. Step four involves determining whether the cloud layer top is an actual top or an "effective top" (ET) (Wang and Sassen, 2001), which is an important factor when considering whether or not these CTH values can be used as ground truth or not. If the signal falls below the P_{min} value, it is considered to be completely attenuated, and this is an ET. A quality flag is included in the output, which indicates whether the top is an actual or ET.
5. In the final step, actual cloud bases are distinguished from virga and precipitation. A key difference between signal characteristics of the two classes is that the signal slope is typically much smaller for virga and precipitation.

There exists an inherent uncertainty of $\pm 2\%$ for all reported distances due to the timing electronics, as well as ± 7.5 m due to the width (i.e., vertical resolution) of each range bin (Coulter, 2012). Other uncertainties related to the MPL instrument that are more difficult to quantify are described in Coulter (2012).

2.4.3 Cloud Optical Property (COP) Retrieval.

Optical thickness ground truth is determined by first using an algorithm for retrieving COD ($\tau*$), and then by converting $\tau*$ to COT (τ) using the VIIRS sensor zenith angle as shown in Equation 2. The same algorithm is also used to retrieve EPS. The algorithm is an ARM VAP that infers the COD and EPS of liquid water clouds from surface-based Multi-Filter Rotating Shadowband Radiometer (MFRSR) measurements of solar irradiance at 0.415 µm in 15-s intervals (Min and Harrison, 1996). This wavelength was chosen due to the lack of gaseous absorption, the relatively constant surface albedo (in the absence of snow), and the fact that its scattering properties are less sensitive to cloud particle sizes (Min and Harrison, 1996; Turner *et al.*, 2014). The algorithm incorporates total LWP measured by a microwave radiometer (MWR) every 20 s to independently retrieve the EPS (r_e) of the warm cloud droplets, which improves the accuracy of the inferred COD. Accuracy is improved due to the "slight dependence" of the extinction coefficient, single scattering albedo, and asymmetry parameter on r_e at this wavelength (Turner *et al.*, 2014). The r_e value is determined from LWP using the inverse of Equation 7 in Section 2.3.6. When a coincident MWR is not available or is inoperable, an assumed r_e of 8 µm is used (Turner *et al.*, 2014).

Input data include observed irradiance from the MFRSR; LWP from the ARM MWR retrieval datastream; Top-of-Atmosphere (TOA) irradiance for clear, stable, temporally proximal days from the Langley regression method; cloud sky cover fraction from the ARM short wave flux analysis VAP, or from the total sky imager if the VAP is not available; estimated CBH from the ARM Clothiaux CBH VAP; infrared sky temperature; and an assumed surface albedo value of 0.036 for green vegetation (Turner *et al.*, 2014). An assumed surface albedo is appropriate for surfaces with such small albedos; however, for a surface with a high albedo, such as snow-covered regions, the albedo becomes much more important. A method for determining the albedo for this VAP for snow-covered regions is still in the evaluation phase, and thus more uncertainty exists in the COD truth data for this background condition (Turner *et al.*, 2014).

Atmospheric transmittance at 0.415 μm is computed using the observed irradiance and the TOA irradiance, where two TOA values are computed for each day (Turner *et al.*, 2014). These values are the mean of clear-sky days within three months before and after the current day being processed. From this sample, the best 10 to 20 points are chosen from which the mean is calculated, as described by Michalsky *et al.* (2001). The heart of the algorithm is the nonlinear least squares method (NLSM), a linearized iterative method described by Bevington (1969). In this method, the solar zenith angle is varying and scattering properties are parameterized to determine EPS and COD, where classic Mie theory is the basis for scattering by approximately-spherical water droplets (Turner *et al.*, 2014). Only COD is returned if the LWP estimate cannot be provided by a coincident MWR.

The VAP assumes horizontally homogeneous, stratiform clouds with COD greater than approximately seven (Turner *et al.*, 2014), and is restricted to daytime retrieval only. A single cloud layer consisting of only liquid water droplets is also assumed. Two temporal resolutions are available for this product: one "instantaneous" output at the 20-second interval of the MFRSR, and an "average" output for the 5-minute period centered on the sample time (Turner *et al.*, 2014). Total 1-σ (i.e., one standard deviation) uncertainties for both COD and EPS are propagated through from the input data and assumed parameters and are available as output. If LWP is available from the MWR retrieval, the uncertainty for LWP is assumed to be 20 g m^{-2}.

One study at the SGP ARM site compared retrieved cloud particle sizes to eight *in situ* vertical profiles constructed from observations by an aircraft-based forward spectra scattering probe, and found that they were within 5.5% (Min *et al.*, 2003). Furthermore, a sensitivity study included in this paper demonstrated that a 13% uncertainty in observed LWP (i.e., 20 g m^{-2}) results in only a 1.5% difference in retrieved COD, but a 12.7% difference in EPS. Therefore, it is clear that EPS is much more sensitive to the relatively large uncertainties of LWP.

2.5 Research Question and Objective

A system-level analysis of the VIIRS CBH IP must include an assessment of other key cloud products used to retrieve CBH in order to completely understand sources of error that drive inaccurate retrievals. Specifically, CTH from the CTP IP, as well as COT and EPS from the COP IP, are assessed for their accuracy. Such an analysis is critical to establishing a detailed algorithm error budget, which is needed to identify the major sources of error in the CBH product and focus future research efforts to address them. Thus, precise measurements are needed not only for the CBH product, but also for the CTH, COT, and EPS products, which led to the use of ground-based data collected at the DOE ARM sites. Data from these ARM sites are assumed to be ground truth data, and are compared to VIIRS data for single-layer water clouds at the pixel level for both daytime and nighttime scenes.

III. Methodology

3.1 Time Period and Location Selection

A significant factor in choosing a time period for the coincident VIIRS and ARM data was the data maturity timeline of the VIIRS cloud products, described in Section 2.3.8. All VIIRS cloud products had been released to the public in beta status by late April 2013, and a report was released in mid-May 2013. Therefore, June 2013 was chosen as the beginning of the research time period. For the sake of time allocated for this research, a cutoff end date was chosen to be 31 October 2015. The other important factor in selecting a time period was that of data availability at each location.

Ground truth locations were chosen by first identifying the data that would be used as ground truth and then finding which locations in the ARM data archive contained those datasets for June 2013 and beyond. In order to evaluate CBH and CTH, at a minimum, it was required that each location have these data available. Any locations that also had data for COP evaluation were considered to be a bonus, as those data were relatively rare. Thus, time periods varied for each location depending on when these particular datasets were available. Individual datasets were placed into one of two categories, as shown in Table 6: Tier 1 for those containing all three ground truth measurements (CBH, CTH, and COP), and Tier 2 for those containing only the CBH and CTH ground truth measurements. Four locations had the measurements needed for the June 2013 - October 2015 time period: Lamont, OK, of the SGP ARM Facility; Darwin, Australia, TWP ARM Facility; Graciosa Island (Isl.), Azores, Portugal, ENA ARM Facility; and the mobile ARM site at Manacapuru, Brazil. Arctic locations at the NSA ARM Facility did not provide enough water-phase cloud cases for evaluation. However, the four selected locations provided observations for both mid-latitude and tropical climates, in addition to covering all seasons. The Lamont and Darwin sites provided all of the Tier 1 data, while the other two consisted of only Tier 2 data. Therefore, the number of cases with COP truth data would be limited.

3.2 Data Sources

The University of Wisconsin Space Science and Engineering Center (SSEC) maintains a NASA Atmosphere Science Investigator-led Processing System (SIPS) website that enabled access to 1 km IP granules, which are the basic units of packaged VIIRS data. One granule contains 48 scans of VIIRS data, which covers approximately 3040 x 570 km, spatially, and about 85 seconds, temporally. The SIPS website contains a search tool that allows users to specify VIIRS granules by product type (e.g. VIIRS CBH IP), date, time, latitude, and longitude. Different methods can be used to specify the spatial search area, but the method used for this research was to search a radius around the latitude and longitude of each ARM site location's coordinates. Matrix Laboratory (MATLAB) software code was used to continuously generate these FTP search pages from the SIPS website until a certain radius was able to single out the closest granule for each VIIRS overpass. With this retrieval method, 12 files of the closest granule were identified and downloaded for every pair of overpasses (six day and six night) for the locations and time periods specified in Table 6. The six files were the moderate-resolution, terrain-corrected geolocation (GMTCO) SDR; CM IP; Parallax-corrected COP IP; Parallax-corrected CTP IP; CLT IP; and CBH IP. All VIIRS files were formatted as Hierarchical Data Format 5 (HDF5) files.

Late in the data collection process, SIPS began removing all GMTCO files prior to 2015 from the online archive, so the NOAA Comprehensive Large Array-Data

Table 6. ARM Sites and Corresponding Data. Tier 1 datasets include all three ground truth measurements (CBH, CTH, COP), while Tier 2 datasets only have the CBH and CTH measurements (i.e., COT and EPS cannot be validated). The far right column shows what percentage of the data were Tier 1 for each location.

ARM Site	Tier 1 Date Range	Tier 1 (months)	Tier 2 Date Range	Tier 2 (months)	Tier 1 %
Lamont, OK, USA	1 Jun 2013 - 9 Jul 2015	25	1 Jun 2013 - 31 Oct 2015	29	86%
Darwin, Australia	1 Jun 2013 - 5 Oct 2014	16	1 Jun 2013 - 30 Dec 2014	19	84%
Graciosa Isl., Azores, Portugal	None	0	2 Oct 2013 - 31 Oct 2015	25	0%
Manacapuru, Brazil	None	0	1 Jan 2014 - 31 Dec 2014	12	0%

Stewardship System (CLASS) was used to collect these files for the remaining locations and time periods. NOAA CLASS packages their VIIRS data in "chunks" of four granules, so the data had to be de-aggregated at the time they were ordered. From the de-aggregated data, the nearest granule was found and downloaded.

All ground truth data were collected using the ARM data archive (ARM, 1996a; 1996b; 1997), which was also used to determine data availability for the locations and time periods in Table 6, as described in section 3.1. The archive search function allows the user to easily browse and order specific data. In the archive, the specific datasets are named ceilometer (listed in the ARM Data Archive as "CEIL") for the CBH truth data, the 30-s MPL Cloud Mask using the first Wang and Sassen (2001) algorithm (30SMPLCMASK1ZWANG) for the CTH truth data, and the 1-minute MFRSR Cloud Optical Depth (MFRSRCLDOD1MIN) for the COP truth data. After datasets were ordered, they were downloaded for each date, time, and location as Network Common Data Form (NetCDF) files using MATLAB code.

3.3 Evaluation

3.3.1 VIIRS-ARM Site Match-ups.

Within each GMTCO granule file, which contains all geolocation data, all pixels were searched to find the pixel with coordinates nearest to those of the particular ARM site being evaluated. Using this spatial match-up method, 89% of the VIIRS-ARM match-ups were within 500 m, and 99% were within 1 km. It was from this single, closest pixel that all other pertinent data were extracted, to include time. The time associated with this pixel was then used to match-up all data from the ARM truth dataset that were within ±5 minutes of the pixel time. An average value for this 10-minute period was used as the ground truth value for each ARM site and data type.

3.3.2 Processing the Data.

Data were processed in three different ways: two different methods for daytime cases, and one for all nighttime cases. This would yield three principal datasets for evaluation.

3.3.2.1 Primary Daytime Method.

Each location and associated datasets were processed one at a time, for the respective time period listed in Table 6, using MATLAB. After the data were processed to find the closest pixel, as described in section 3.3.1, the VIIRS CM data were then used to determine if it was a suitable test case by meeting four criteria:

1. Pixel must be "confidently cloudy," meaning that all tests in the CM algorithm indicate that the pixel is cloudy

2. Pixel CM quality must be "high," meaning the maximum number of tests were used, given the limiting factors of background conditions and solar illumination
3. Pixel cloud phase must be "water" phase, indicating that the pixel scene was comprised completely of liquid water cloud particles
4. The thin cirrus flag in the CM algorithm indicated that no thin cirrus clouds were present in the pixel scene

If any of the above criteria were not met, the case was omitted by the MATLAB code. At a minimum, a case had to include both VIIRS-calculated and ground truth values for both CBH and CTH to be evaluated. Furthermore, there were cases where a liquid water phase was identified by the CM IP, but an inconsistent cloud type (i.e., cirrus or cirrocumulus) was chosen in the CLT IP. In the CLT IP clustering algorithm, all pixels within a 6x6 km grid cell are assigned the same cloud type, so it was likely that cirrus was too close to the ARM site to be a valid test case. This was confirmed using a manual inspection of false-color imagery, as described in Section 3.3.3.

Next, other important data were extracted from each VIIRS file for the nearest pixel, including sensor and solar zenith angles from the GMTCO, COT and EPS from the COP IP, CTH from the CTP IP, cloud type from the CLT IP, and CBH from the CBH IP. Truth data were also extracted and included the lowest instantaneous CBH from the CEIL file, the highest instantaneous CTH from the 30SMPLCMASK1ZWANG file, and the instantaneous COD and EPS values from the MFRSRCLDOD1MIN file. All of these instantaneous values were averaged over a 10-minute period (i.e., within ± 5 minutes of the pixel time), as described in section 3.3.1.

To compare these VIIRS-calculated and ARM ground truth values, they had to be converted to common units and measurements. CBH and CTH values were compared in meters, while EPS values were compared in microns. Additionally, the unitless COD ground truth value (τ^*) from the MFRSR VAP was converted to COT (τ) using the cosine of the VIIRS sensor scan (i.e., slant-path) angle, as shown in Equation 2. VIIRS assumes a wavelength of 550 nm when calculating COT, while the ARM VAP uses transmittance at 415 nm to estimate COT; therefore, it was assumed that atmospheric extinction coefficients were the same for these two wavelengths, which is a very good approximation for these wavelengths and particle sizes (Warren, 2015).

Furthermore, two different methodologies were used to handle the attenuation flag information described in step four of the CTH algorithm in Section 2.4.2. In this primary daytime method, the first and simplest method was to average the attenuation flag array corresponding to the 10-minute average of the CTH truth data. If the average was closer to the value of an ET, then it was labeled as such; otherwise, it was labeled as an actual top. With this method, an ET implies that the array used to calculate the CTH truth value was more heavily weighted with false tops, and should therefore be used with caution.

3.3.2.2 Alternate Daytime Method.

Another method was added in order to increase the robustness of the evaluation. The alternate daytime method involved all of the same steps as the primary method, but with a different approach to the ARM CTH attenuation flag handling. It consisted of removing all effective CTH values from the array before averaging, such that the CTH ground truth value was an average of only true CTH values, uncontaminated by ET values. While this second method was more ideal, there were many cases that consisted entirely of ETs (i.e., optically thick clouds that completely attenuated all of the MPL signals during that 10-minute period). Therefore, this second method limited the number of total cases in the study, especially with the ±5 minute time period that was used. To offset this limitation, time periods of ±10 minutes and ±15 minutes were attempted, but this only resulted in larger errors, especially for COT. These results were not included in this document.

3.3.2.3 Nighttime Method.

The nighttime method consisted of all the same steps as the primary daytime method, but with one significant difference: the COT and EPS products could not be evaluated. The ground truth measurements for these properties rely on solar reflectance information. Additionally, the false color imagery, described below, could not be used to verify cloud phases for the nighttime cases.

3.3.3 Test Scene Identification using False Color Images.

False-color, composite images were used to verify the cloud phase calculated by the VIIRS CM IP. These images were generated using the method described by Hutchison and Cracknell (2005). The method involves using the M1 (0.412 μm), M9 (1.378 μm), and M10 (1.610 μm) channels to create multi-spectral images in which cloud phases and types are clearly observed. Low-level water clouds appear yellow, while mid-level water clouds appear gray/white, as shown in Figure 4. More information is given in the figure caption below.

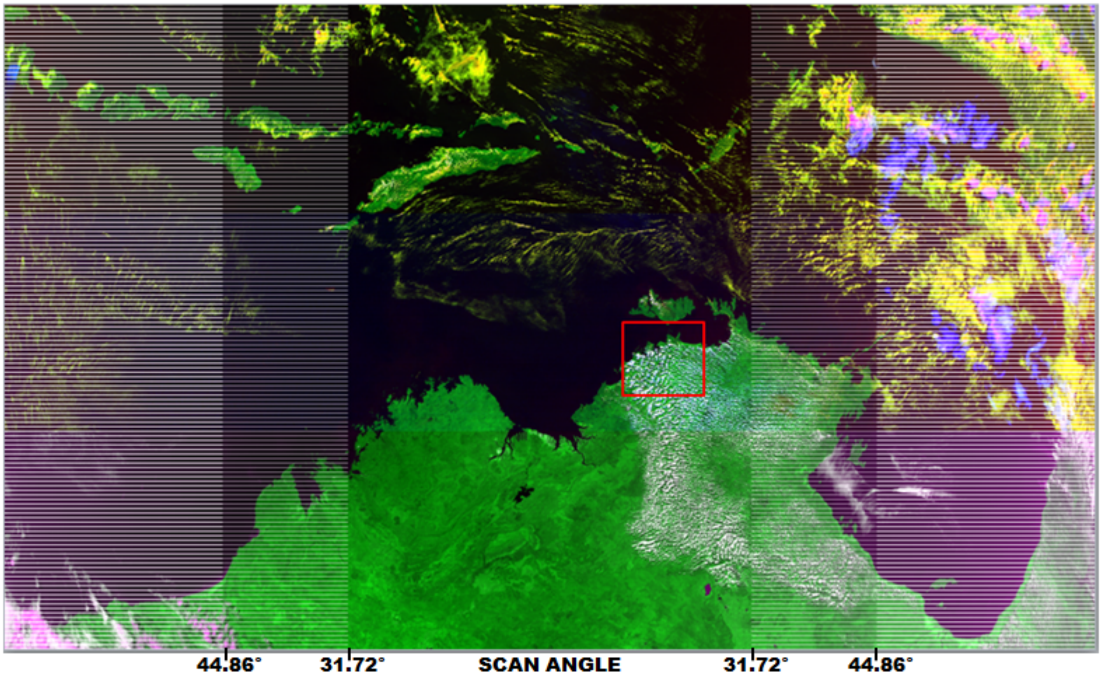

Figure 4. VIIRS False-color Image Example. False-color (red-green-blue) composite image used to identify the cloud types in the VIIRS scene being used (Hutchison and Cracknell, 2005). This scene is July over Darwin, Australia. Yellow means stronger reflectance in the red (M1, 0.412 µm for this method) and green (M10, 1.61 µm), characteristic of low-level water clouds. Pink and purple have strong reflectance in red and blue (M9, 1.378 µm), indicative of high-level, thick ice clouds, while blue alone is a thin ice cloud. Mid-level water clouds are shown in the red box (surrounding Darwin), where there is approximately equal contribution from all three bands, and so the clouds appear gray/white. Snow/ice (when present) is shown in red for low elevations, and in blue/purple for higher elevations. Water appears dark blue/black, and land surfaces appear green. Scan angles across the bottom of the figure indicate the appearance of "bow-tie" deleted pixels, which is described in Section 2.2.2. These deleted pixels first appear at 31.72 degrees, and double in size at 44.86 degrees.

IV. Results and Analysis

4.1 Initial Results

4.1.1 Daytime Results using Primary Method.

Daytime comparisons for VIIRS CBH and upstream cloud products were made using the truth data collected at all four ARM sites, first with the primary data processing method from Section 3.3.2.1. The data in Figures 5-8 represent 156 coincident, daytime observations for single-layer water clouds found in VIIRS-ARM site match-ups for the period of 1 June 2013 to 31 October 2015, using this primary method. Correlation between VIIRS and ARM CBH is plotted on the left side of Figure 5 (in blue), while correlation between VIIRS and ARM CTH is plotted on the right side (in red). In Figure 6, CBH error is shown in blue (+), while CTH error is shown in red (*). Additionally, average CBH error is represented by the solid blue line, while average CTH error is represented by the dashed red line. Error was calculated by subtracting the ARM ground truth values from the VIIRS values.

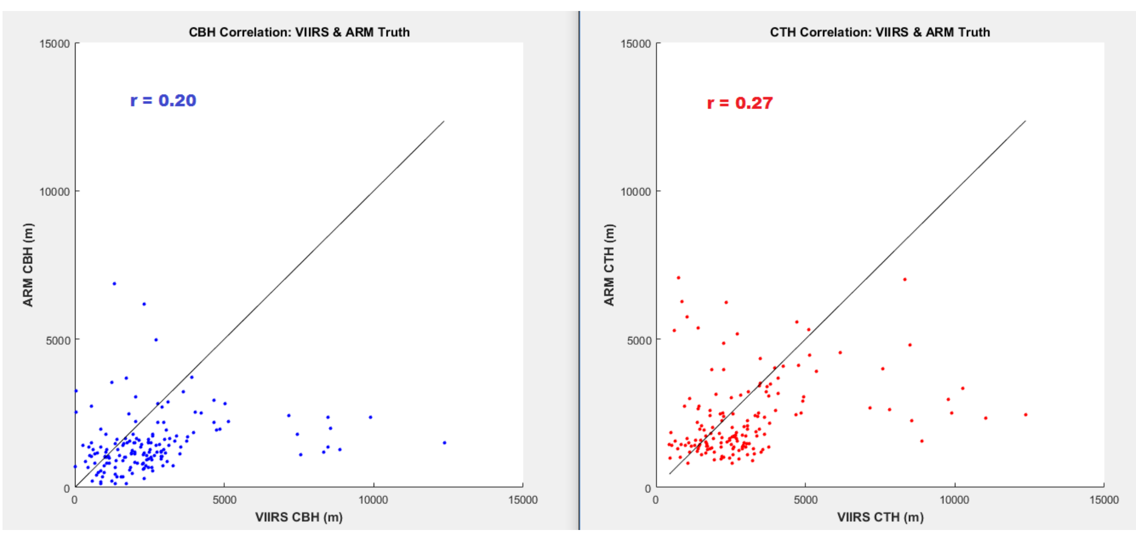

Figure 5. Correlations for CBH and CTH (Primary Daytime). Correlation of VIIRS and ARM CBH is shown on the left (in blue), while correlation of VIIRS and ARM CTH is shown on the right (in red).

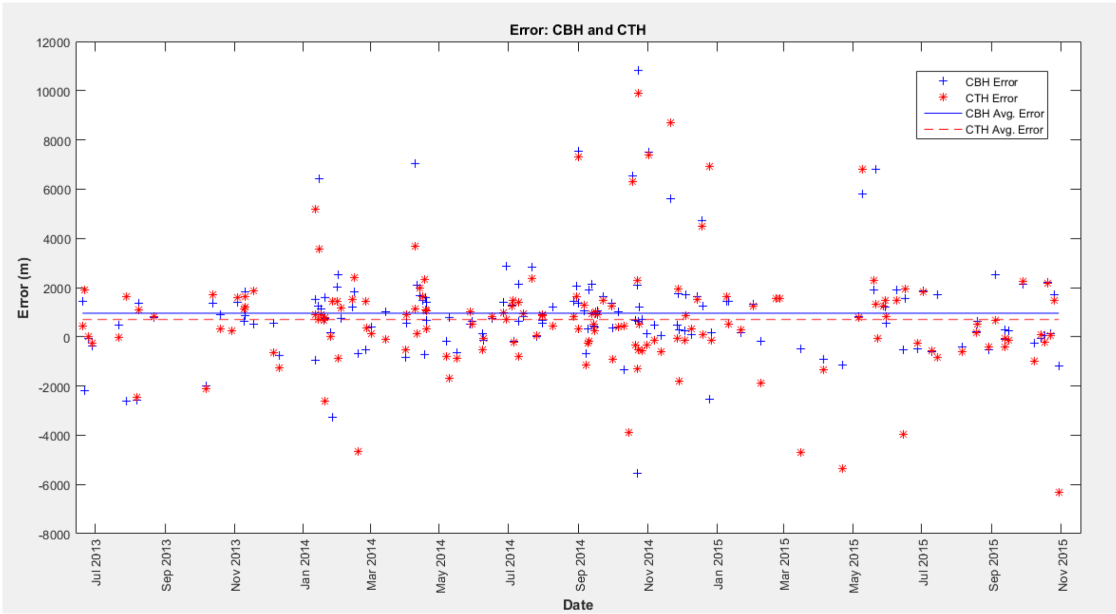

Figure 6. Error (VIIRS - ARM) for CBH and CTH (Primary Daytime). CBH error is shown in blue (+), while CTH error is shown in red (*). Average CBH error is indicated with the solid blue line, while average CTH error is indicated with the dashed red line.

Correlation is weak for both CBH and CTH, with a significant cluster of observations towards the lower right-hand side of each plot - indicating that VIIRS often overestimates both CBH and CTH. This is consistent with the average (i.e., arithmetic mean) error (VIIRS - ARM) of CBH and CTH, plotted in Figure 6, which demonstrates a large positive bias for both products. Similar plots are shown for the two other key, upstream VIIRS cloud products, COT and EPS, in Figures 7 and 8 below.

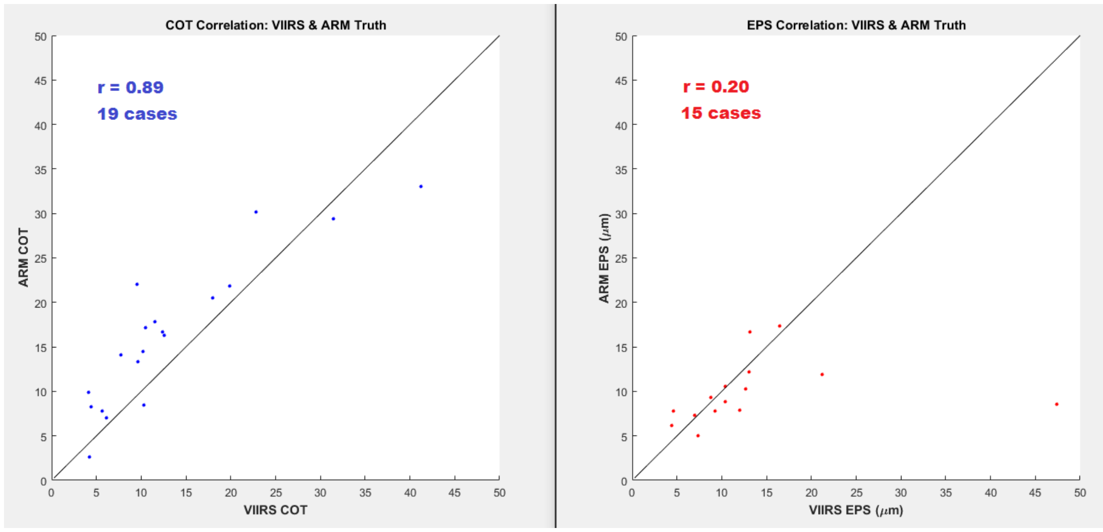

Figure 7. Correlations for COT and EPS (Primary Daytime). Correlation of 19 coincident VIIRS and ARM COT observations is shown on the left (in blue), while correlation of 15 coincident VIIRS and ARM EPS observations is shown on the right (in red).

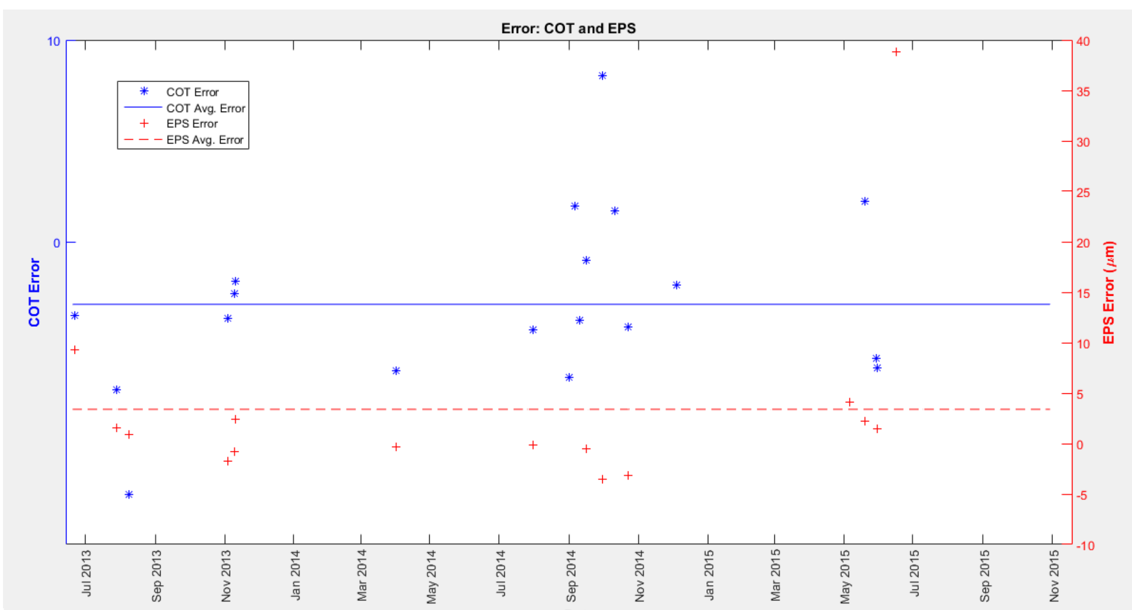

Figure 8. Error (VIIRS - ARM) for COT and EPS (Primary Daytime). COT error is shown in blue (*), while CTH error is shown in red (+). Average COT error is indicated with the solid blue line, while average EPS error is indicated with the dashed red line.

The number of cases comparing VIIRS and ARM data for these products was much lower, with only 19 cases for COT and 15 for EPS. VIIRS COT has a much stronger correlation with its ARM counterpart, at 0.89, while the EPS correlation is weak and similar to that of CBH and CTH, at 0.20. In Figure 8, COT (blue *, axis on left) has a negative bias, while EPS (red +, axis on right) has a positive bias, as indicated by the different scales of their respective y-axes.

Corresponding statistics are shown in Table 7. Of the 156 cases, 69 occurred at the Graciosa Island site (Azores, Portugal), 39 at the Lamont, OK site, 34 at the Manacapuru, Brazil site, and 14 match-ups at the Darwin, Australia site. Comparisons between the VIIRS cloud products and ARM site truth data are shown for CBH, CTH, COT, and EPS, as a function of cloud type. The numbers of COT and EPS cases, which were much smaller than that of CBH and CTH, are indicated by the parentheses in the correlation coefficient (r) column for each cloud type.

Table 7. Daytime Statistics (Primary). All VIIRS - ARM daytime match-up datasets, segregated by cloud type, along with the error (VIIRS - ARM) of VIIRS cloud products compared to the ARM ground-based truth datasets. Cloud types are stratus (ST), altocumulus (AC), and cumulus (CU). These results were generated using the primary daytime processing method described in Section 3.3.2.1. Numbers of COT and EPS cases are in parentheses.

ARM Site Observations		**VIIRS CBH**		**VIIRS CTH**		**VIIRS COT**		**VIIRS EPS**	
Cloud Type	*# of Cases*	r	*Avg. Error (m)*	r	*Avg. Error (m)*	r	*Avg. Error*	r	*Avg. Error (μm)*
ST	14	0.33	443.0	0.30	287.5	1.00 (2)	-3.7	1.00 (2)	-0.4
CU	82	0.17	1191.0	0.13	694.2	0.99 (3)	2.8	-0.09 (4)	10.0
AC	60	0.26	757.6	0.58	802.4	0.87 (14)	-4.3	0.73 (9)	1.3
Total	**156**	**0.20**	**957.2**	**0.27**	**699.3**	**0.89 (19)**	**-3.1**	**0.20 (15)**	**3.4**

In general, the correlations between the VIIRS cloud products and ARM truth data were poor, except for the COT product, which had a relatively high correlation coefficient of 0.89. Correlation for the CBH product was 0.20 for all cloud types, although it improved slightly to 0.33 for the 14 stratus cloud cases. Correlations for the CTH and EPS products were 0.27 and 0.20, respectively. VIIRS CBH and CTH both had a high bias for all cloud types, but especially for cumulus CBH. COT values had a low bias overall, with average VIIRS-calculated values being smaller than that of the truth data for all cloud types. Cumulus was the exception, however. By far, the lowest correlation and largest errors for EPS came from the four cumulus cases. The alternate data processing method for daytime cases was evaluated, as well, in order to see if results were similar for both methods.

4.1.2 Daytime Results using Alternate Method.

Daytime match-ups using the alternate ARM CTH attenuation flag handling method, described in Section 3.3.2.2, yielded 63 total cases, only six of which contained COT and EPS comparisons.

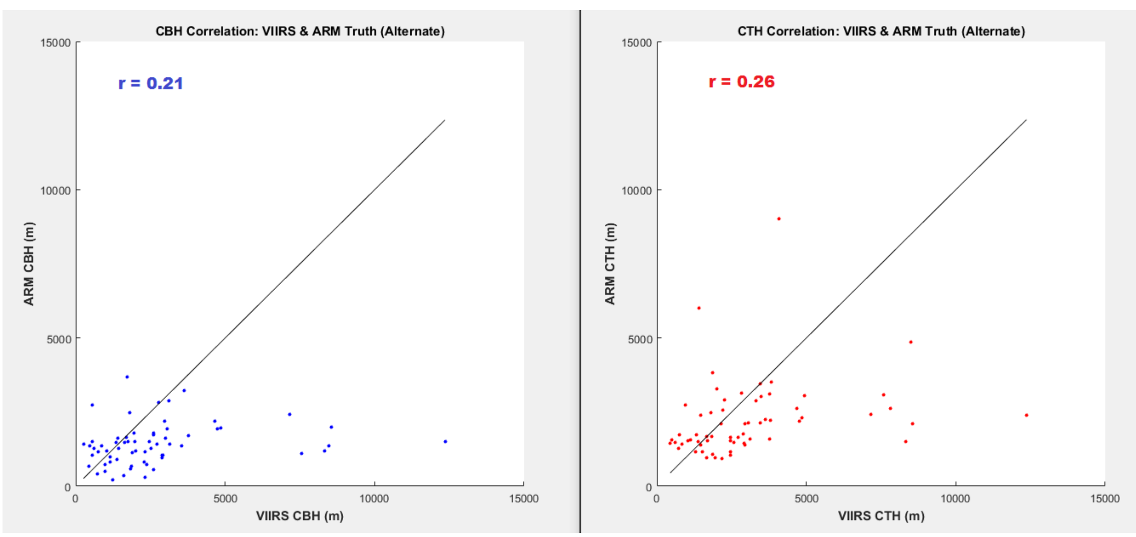

Figure 9. Correlations for CBH and CTH (Alternate Daytime). Correlation of VIIRS and ARM CBH is shown on the left (in blue), while correlation of VIIRS and ARM CTH is shown on the right (in red).

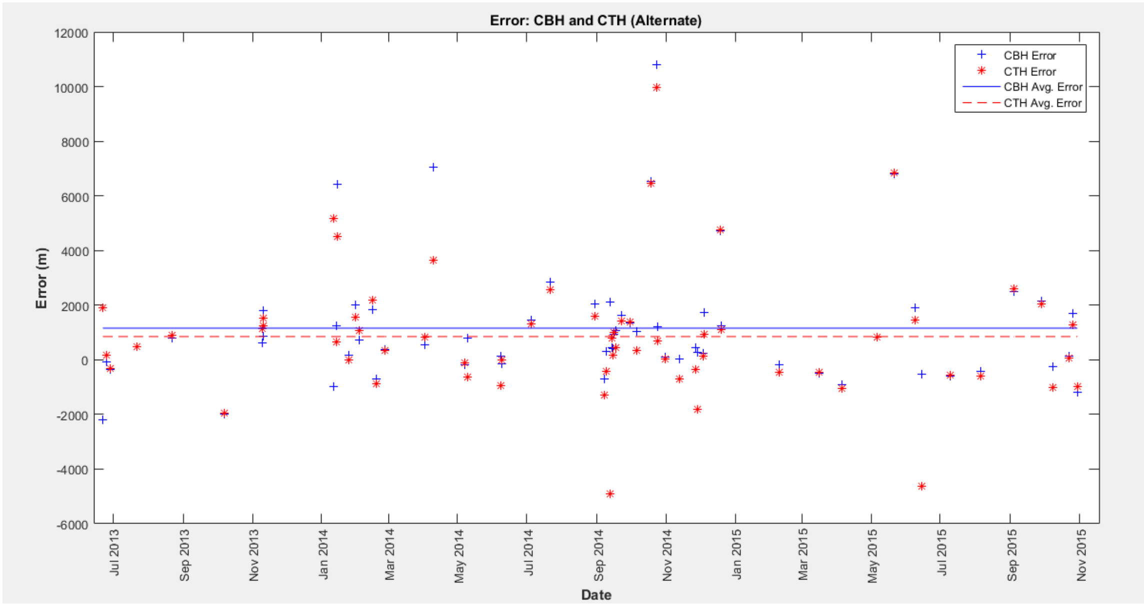

Figure 10. Error (VIIRS - ARM) for CBH and CTH (Alternate Daytime). CBH error is shown in blue (+), while CTH error is shown in red (*). Average CBH error is indicated with the solid blue line, while average CTH error is indicated with the dashed red line.

Figure 9 shows CBH and CTH correlations that are very similar to those using the primary data processing method in the preceding section. Additionally, Figure 10 again shows a large positive bias for both CBH and CTH, indicated by their average errors. The two following figures show COT and EPS in the same way as the preceding section, but for a small sample size of only six cases each.

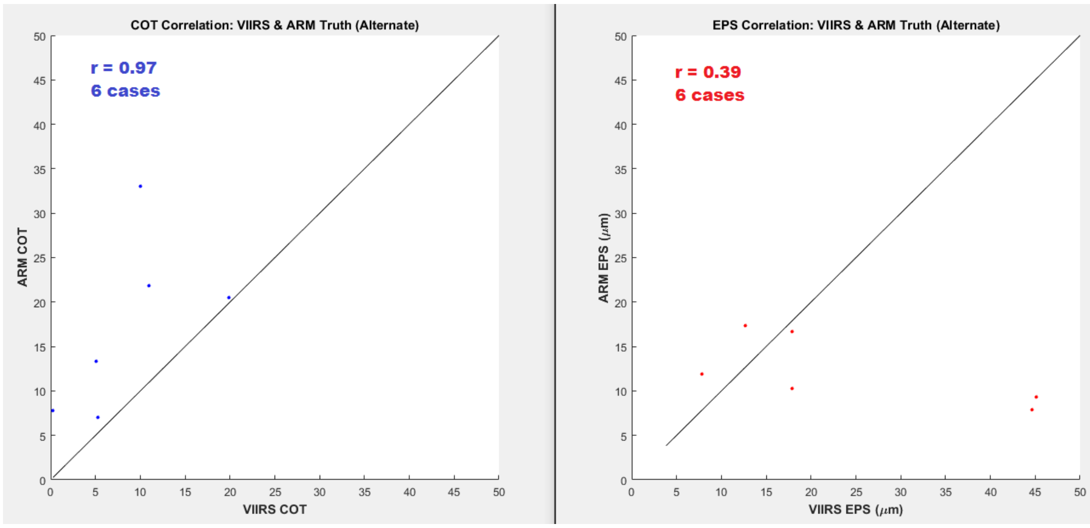

Figure 11. Correlations for COT and EPS (Alternate Daytime). Correlation of 19 coincident VIIRS and ARM COT observations is shown on the left (in blue), while correlation of 15 coincident VIIRS and ARM EPS observations is shown on the right (in red).

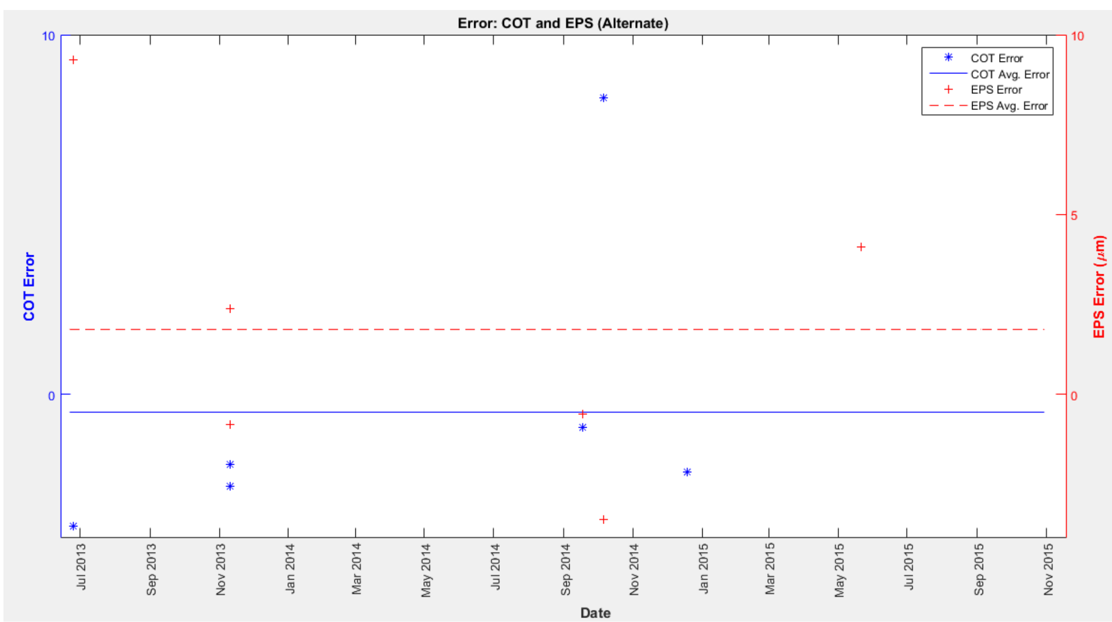

Figure 12. Error (VIIRS - ARM) for COT and EPS (Alternate Daytime). COT error is shown in blue (*), while CTH error is shown in red (+). Average COT error is indicated with the solid blue line, while average EPS error is indicated with the dashed red line.

The six COT cases in Figure 11 again show a strong correlation with the ARM COT values, while the correlation of six VIIRS-ARM EPS cases is weak and similar to CBH and CTH. Furthermore, there is a negative COT bias and positive EPS bias in Figure 12, just as with the primary method, but they are smaller with this alternate method. It is difficult to draw conclusions from such small COT and EPS sample sizes, but there is clearly a very similar trend to that of the primary method. The same statistics were generated for the alternate method results and are shown in Table 8 below.

Table 8. Daytime Statistics (Alternate). All VIIRS - ARM daytime match-up datasets, segregated by cloud type, along with the error (VIIRS - ARM) of VIIRS cloud products compared to the ARM ground-based truth datasets. Cloud types are stratus (ST), altocumulus (AC), and cumulus (CU). These results were generated using the alternate daytime processing method described in Section 3.3.2.2. Numbers of COT and EPS cases are in parentheses.

ARM Site Observations		**VIIRS CBH**		**VIIRS CTH**		**VIIRS COT**		**VIIRS EPS**	
Cloud Type	*# of Cases*	*r*	*Avg. Error (m)*	*r*	*Avg. Error (m)*	*r*	*Avg. Error*	*r*	*Avg. Error (μm)*
ST	6	-0.08	648.2	0.05	678.8	N/A (1)	-0.9	N/A (1)	-0.6
CU	42	0.22	1430.4	0.22	777.4	1.00 (2)	3.1	1.00 (2)	-0.6
AC	15	0.34	605.9	0.48	1115.8	0.99 (3)	-2.8	0.42 (3)	4.2
Total	**63**	**0.21**	**1159.6**	**0.26**	**848.6**	**0.97 (6)**	**-0.5**	**0.39 (6)**	**1.8**

The total number of valid cases decreased by 60% to 63, and the number of cases including COT and EPS dropped sharply to only six cases each. Comparing these results to those of all 156 cases in Table 7, one can see that CBH performance is very similar using the two different data processing methods, with correlations of 0.20 and 0.21 for the primary and alternate methods, respectively. CTH correlation was also very similar using the two methods, at 0.27 and 0.26, for primary and alternate, respectively. CBH and CTH bias was once again positive, and slightly larger than that of the primary method. COT correlation was higher for the alternate method - likely a result of such a small number of cases.

4.1.3 Nighttime Results.

Nighttime results consisted of only CBH and CTH comparisons, as ARM COT and EPS truth data were not available for nighttime cases. A total of 27 match-ups were generated using the same method as the primary daytime dataset. The same correlation and error plots were created for these nighttime cases and are shown in the two figures below.

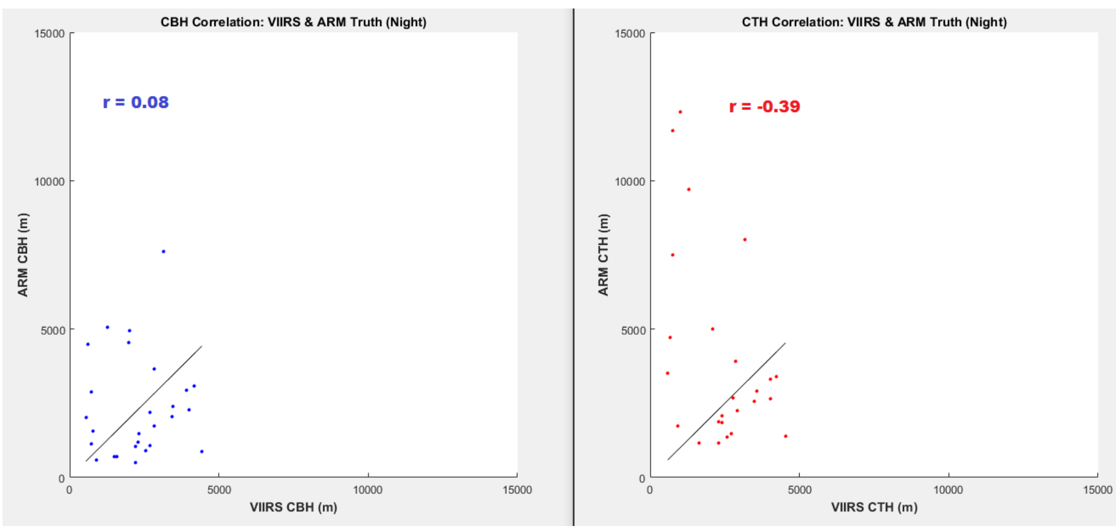

Figure 13. Correlations for CBH and CTH (Nighttime). Correlation of VIIRS and ARM CBH is shown on the left (in blue), while correlation of VIIRS and ARM CTH is shown on the right (in red).

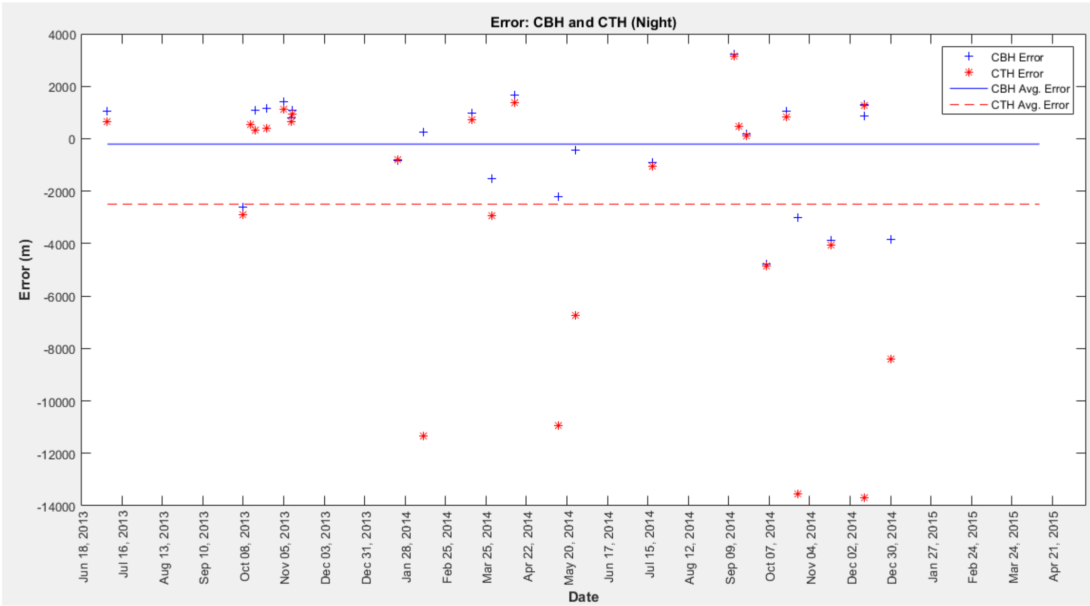

Figure 14. Error (VIIRS - ARM) for CBH and CTH (Nighttime). CBH error is shown in blue (+), while CTH error is shown in red (*). Average CBH error is indicated with the solid blue line, while average CTH error is indicated with the dashed red line.

Results were similar to those of the daytime cases, but correlations and errors were generally worse, as expected. The correlations in Figure 13 for CBH and CTH were 0.08 and -0.39 (anti-correlated), respectively, compared to 0.20 and 0.27 from the primary daytime results. The statistics for these results are summarized in Table 9 below. The bias for CBH was negative for these nighttime cases, as seen in Figure 14, owing primarily to the large, negative average error for stratus. This was surprising, but such large errors were likely produced by an outlier in such a small sample size. More analysis was needed in order to better understand these results for both daytime and nighttime cases, and the first thing to do was to identify such outliers.

Table 9. Nighttime Statistics. All VIIRS - ARM nighttime match-up datasets, segregated by cloud type, along with the error (VIIRS - ARM) of VIIRS cloud products compared to the ARM ground-based truth datasets. COT and EPS ground truth data were not available for nighttime cases. Cloud types are stratus (ST), altocumulus (AC), and cumulus (CU).

ARM Site Observations		**VIIRS CBH**		**VIIRS CTH**	
Cloud Type	*# of Cases*	*r*	*Avg. Error (m)*	*r*	*Avg. Error (m)*
ST	3	0.32	-2534.2	0.94	-5966.8
CU	6	0.70	553.3	-0.67	-2496.6
AC	18	-0.02	-70.3	-0.37	-1920.6
Total	**27**	**0.08**	**-205.5**	**-0.39**	**-2498.2**

4.2 Removal of Outliers

Due to the overall poor accuracy and correlation with truth data, outlying cases were removed from the complete dataset to see how they were impacting performance. Outliers were removed for the following conditions:

1. CTH greater than 20,000 ft (6100 m, both VIIRS and ARM truth)
2. CTH error greater than 10,000 ft (3050 m), or less than -10,000 ft (-3050 m)
3. COT/EPS truth uncertainty greater than 10%, based on the output parameter from the ARM VAP used for COP truth data (described in Section 2.4.3); not all ARM COD/EPS truth values have an associated uncertainty value, as it was unable to be calculated by the VAP for some cases
4. EPS error greater than 5 µm, or less than -5 µm

Criterion 1 was needed in order to identify those cases in which cloud phases were labeled as water clouds, but the height of the layer indicated that this was unlikely. The false-color images were also used to confirm the existence of these erroneous cloud phases for daytime images. Criterion 2 was necessary to omit the cases in which it was clear that the VIIRS and ARM instruments were detecting two different layers. Criterion 3 identified the cases where there was too much uncertainty for the ARM data to serve as reliable ground truth. Criterion 4 was used to omit cases of large VIIRS EPS error, which included two cases where the errors were 39 and 9 µm - significantly larger than all other cases.

Criteria 1 and 2 are shown graphically in Figure 15. Criterion 1 (CTH outliers) is shown in blue, such that all markers above the blue line are the outliers. The majority of the outliers are VIIRS CTH values (indicated by symbol: *), although there are some ARM CTH outliers (indicated by symbol: +), as well. Criterion 2 (CTH error outliers) are in red, and all of the red markers that fall outside of the space contained between the two lines (i.e., between -10,000 ft and 10,000 ft) are the outliers. More error outliers exist on the positive end, which is not surprising considering the overall positive bias that was found in the preceding section. Some VIIRS cases were outliers for both criteria, as indicated by the vertically aligned red and blue asterisk (*) markers falling outside of the defined ranges.

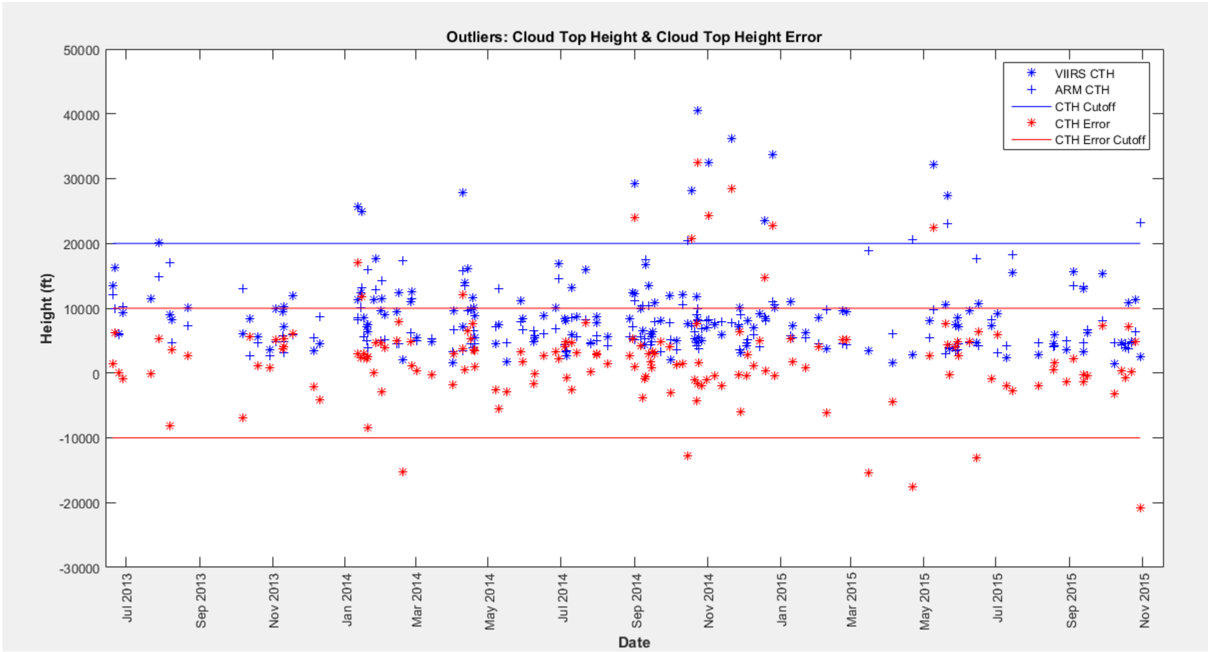

Figure 15. CTH Outliers. Outliers identified for CTH > 20,000 ft (6100 m) and CTH error (VIIRS CTH – ARM CTH) > 10,000 ft (3050 m, or < -10,000 ft/-3050 m). CTH values are listed in blue (∗ for VIIRS CTH and + for ARM CTH), while CTH error values are listed in red (∗). Generated using the primary daytime processing method described in Section 3.3.2.1.

COP outliers are shown graphically in Figure 16, where criterion 3 outliers (ARM COD/EPS truth uncertainty outliers) are in blue, and criterion 4 (EPS error outliers) are in red. Again, all blue markers lying above the blue line are outliers, and all red markers outside of the two red lines are outliers. Both kinds of blue markers are ARM values in this figure, with (*) representing the COD uncertainty, and (+) representing the EPS uncertainty. Only one EPS uncertainty outlier exists; all the rest are COD uncertainty. The red markers represent the VIIRS EPS error outliers, of which there were only two.

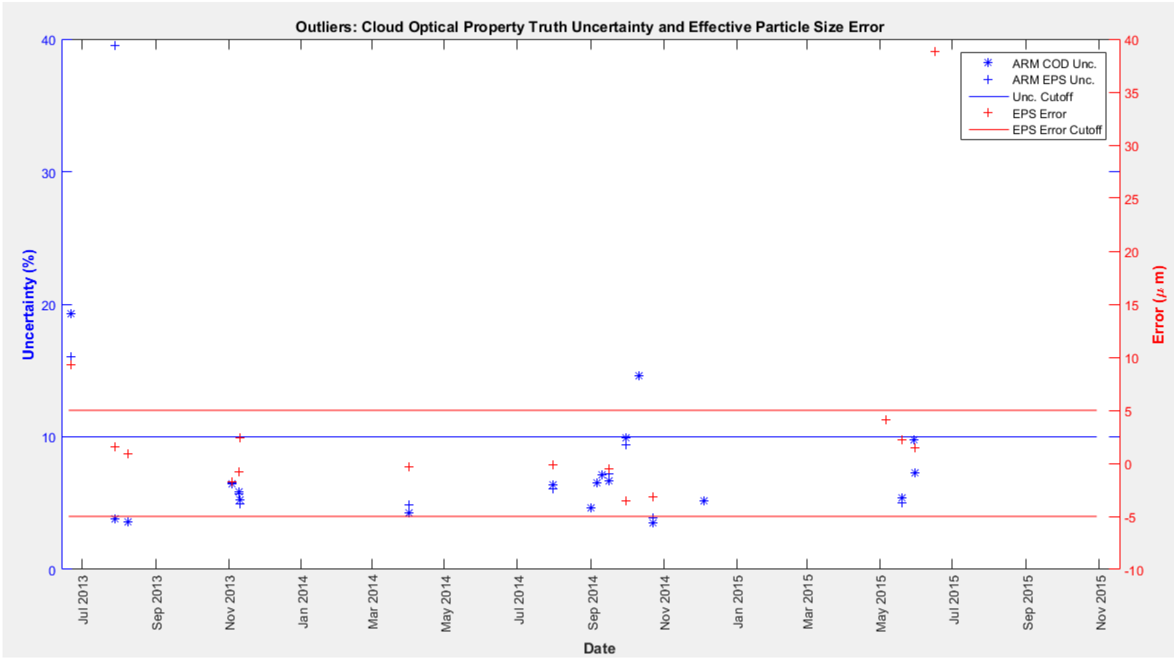

Figure 16. COD and EPS Outliers. Outliers identified for COD/EPS uncertainty > 10% and EPS error (VIIRS EPS – ARM EPS) > 5 μm (or < - 5 μm). Uncertainty values are listed in blue (∗ for ARM COD Uncertainty and + for ARM EPS Uncertainty), while ARM EPS error values are listed in red (+). Generated using the primary daytime processing method described in Section 3.3.2.1.

After these outliers were removed, 134 daytime cases remained for the primary method, the results of which are shown in Table 10. Overall, CBH and CTH correlations nearly doubled to 0.36 and 0.50, respectively, while EPS correlation increased four-fold to 0.82 (shown graphically in Figure 17). In general, average error was reduced drastically for all cloud types except for stratus, which had no outlier cases. Correlation improved from -0.09 to 0.87, and average error fell from 10 μm to 0.4 μm.

Table 10. Daytime Statistics with Outliers Removed (Primary). Outliers removed for CTH > 20,000 ft (6100 m) and CTH error (VIIRS CTH – ARM CTH) > 10,000 ft (3050 m, or < -10,000 ft/-3050 m), COD/EPS uncertainty > 10% and EPS error (VIIRS EPS – ARM EPS) > 5 µm (or < - 5 µm). Cloud types are stratus (ST), altocumulus (AC), and cumulus (CU). Generated using the primary daytime processing method described in Section 3.3.2.1. Numbers of COT and EPS cases are in parentheses.

ARM Site Observations		VIIRS CBH		VIIRS CTH		VIIRS COT		VIIRS EPS	
Cloud Type	*# of Cases*	*r*	*Avg. Error (m)*	*r*	*Avg. Error (m)*	*r*	*Avg. Error*	*r*	*Avg. Error (µm)*
ST	14	0.33	443.0	0.30	287.5	1.00 (2)	-3.7	1.00 (2)	-0.4
CU	65	0.33	670.1	0.36	373.1	0.99 (3)	2.8	0.87 (3)	0.4
AC	55	0.39	850.3	0.65	584.8	0.73 (11)	-4.6	0.84 (7)	0.1
Total	**134**	**0.36**	**720.3**	**0.50**	**451.0**	**0.90 (16)**	**-3.1**	**0.82 (12)**	**0.1**

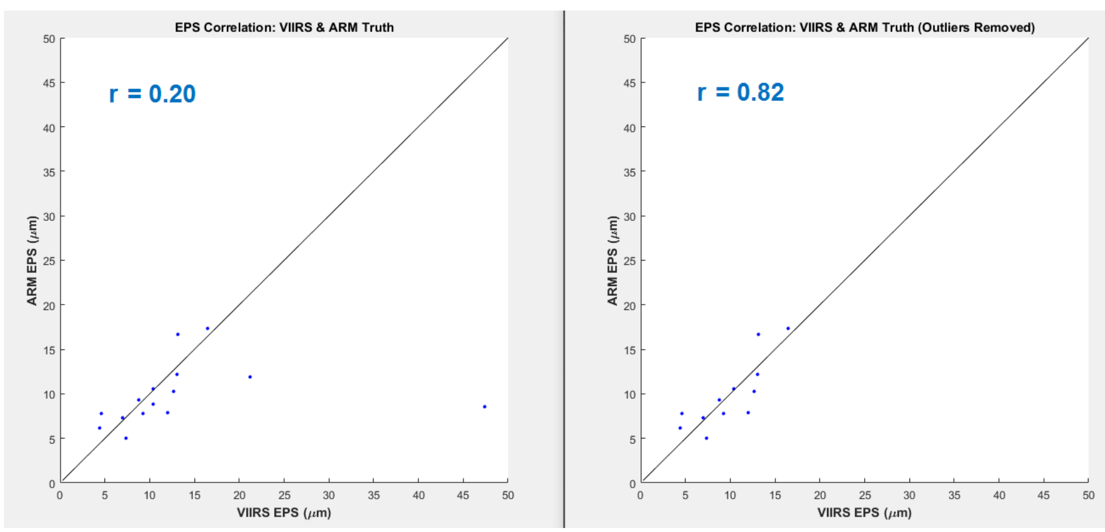

Figure 17. EPS Correlation Comparison. Correlation before (left) and after (right) outliers are removed for error > 5 µm (or < - 5 µm), using the primary daytime results. Correlation improves dramatically after outliers are removed. Generated using the primary daytime processing method described in Section 3.3.2.1.

The alternate CTH attenuation flag method produced similar results, with 53 of the 63 cases left after outlier removal, as shown in Table 11. The CBH correlation more than doubled from 0.21 to 0.44, and CBH average error was nearly cut in half, decreasing from 1160 m to 610 m. Likewise, CTH correlation improved from 0.26 to 0.41, while CTH average error dropped from 849 m to 373 m. Much like the primary daytime results, EPS saw the most significant improvement with just a single case removed. Correlation improved from 0.39 to 0.74, and error dropped from 1.8 µm to 0.3 µm.

Table 11. Daytime Statistics with Outliers Removed (Alternate). Outliers removed for CTH > 20,000 ft (6100 m) and CTH error (VIIRS CTH – ARM CTH) > 10,000 ft (3050 m, or < -10,000 ft/-3050 m), COT/EPS uncertainty greater than 10%, and EPS error (VIIRS EPS – ARM EPS) > 5 µm (or < - 5 µm). Cloud types are stratus (ST), altocumulus (AC), and cumulus (CU). Generated using the alternate daytime processing method described in Section 3.3.2.2. Numbers of COT and EPS cases are in parentheses.

ARM Site Observations		**VIIRS CBH**		**VIIRS CTH**		**VIIRS COT**		**VIIRS EPS**	
Cloud Type	*# of Cases*	*r*	*Avg. Error (m)*	*r*	*Avg. Error (m)*	*r*	*Avg. Error*	*r*	*Avg. Error (µm)*
ST	6	-0.08	648.2	0.05	678.8	N/A (1)	-0.9	N/A (1)	-0.6
CU	34	0.36	475.2	0.36	177.8	1.00 (2)	3.1	1.00 (2)	-0.6
AC	13	0.61	943.0	0.50	742.1	1.00 (2)	-2.4	1.00 (2)	1.6
Total	**53**	**0.44**	**609.5**	**0.41**	**372.9**	**0.98 (5)**	**0.1**	**0.74 (5)**	**0.3**

Improvement was even more drastic for the 18 nighttime cases remaining after omission of CTH and CTH error outliers. As shown in Table 12, correlations increased from 0.08 to 0.39 for CBH, and from -0.39 to 0.20 for CTH, which were still weak correlations. The negative bias that existed before outlier removal became a positive bias for both CBH and CTH. While the removal of these outliers yielded some interesting results, some analysis of upstream cloud products was needed to identify the largest sources of error.

Table 12. Nighttime Statistics with Outliers Removed. Outliers removed for CTH > 20,000 ft (6100 m) and CTH error (VIIRS CTH – ARM CTH) > 10,000 ft (3050 m, or < -10,000 ft/-3050 m). Cloud types are stratus (ST), altocumulus (AC), and cumulus (CU).

ARM Site Observations		**VIIRS CBH**		**VIIRS CTH**	
Cloud Type	*# of Cases*	*r*	*Avg. Error (m)*	*r*	*Avg. Error (m)*
ST	1	N/A	-1506.8	N/A	-2933.5
CU	4	0.83	873.9	0.91	774.9
AC	13	0.31	482.0	0.27	213.7
Total	**18**	**0.39**	**458.6**	**0.20**	**163.6**

4.3 Analysis of the Upstream Cloud Products

4.3.1 CTH Analysis: CBH Sensitivity to CTH Error.

Since the COT is a reflection of the cloud geometric thickness, as shown in Equations 7 and 8, additional analyses were needed to better understand the poor correlations for CBH products in spite of the excellent COT correlations. The individual cloud cases were examined more closely, and the results for a subset (April 2014 through May 2015) of the individual VIIRS-ARM truth match-up data collected at the Lamont, OK site are shown in Table 13. The subset serves to help demonstrate the sensitivity analysis using the primary daytime dataset, but with a smaller, less cumbersome sample size. The subset only consists of cases from the Lamont, OK site, which contained the greatest number of COT and EPS match-ups, as well as the largest mixture of cloud types. The first column contains the calendar dates of the match-up dataset, and the second shows the type of cloud present, based upon the cloud type output parameter from the VIIRS CLT IP described in Section 2.3.5. The VIIRS CBH, CTH, and COT are shown in Table 13, columns 3, 6, and 9, while the corresponding ARM cloud products are in columns 4, 7, and 10, respectively. The EPS is not shown for convenience. The arithmetic errors between the VIIRS and truth data (VIIRS – ARM) for the match-ups are shown in columns 5, 8, and 11.

Table 13. Daytime Subset. Error of VIIRS CBH and other VIIRS cloud data products based upon comparisons with ARM site truth match-ups. Cloud types are stratus (ST), altocumulus (AC), and cumulus (CU). Generated using the primary daytime processing method described in Section 3.3.2.1.

Date	Cloud Type	VIIRS CBH (m)	ARM CBH (m)	CBH Error (m)	VIIRS CTH (m)	ARM CTH (m)	CTH Error (m)	VIIRS COT	ARM COT	COT Error
4/1/2014	ST	36.7	865.7	-829.0	472.2	1003.2	-531.1	7.7	14.1	-6.4
4/2/2014	AC	2293.6	1740.6	552.9	2949.9	2043.9	905.9	30.8	-	-
5/30/2014	CU	2152.9	1537.3	615.6	2542.7	2028.2	514.5	2.0	-	-
6/9/2014	CU	1319.8	1469.7	-149.8	1674.0	1731.3	-57.3	1.7	-	-
6/17/2014	AC	2240.1	1512.1	727.9	2685.9	1861.2	824.7	11.0	-	-
6/27/2014	AC	2586.9	1193.1	1393.8	3063.5	2082.5	981.0	10.9	-	-
7/31/2014	AC	2160.2	1608.6	551.5	2660.8	1759.9	900.9	12.4	16.7	-4.4
9/1/2014	AC	3080.0	1728.3	1351.7	3712.4	3400.2	312.3	10.4	17.2	-6.7
9/6/2014	AC	2513.4	1445.4	1068.0	3015.0	1725.6	1289.4	10.3	8.5	1.8
9/10/2014	AC	4710.0	2818.3	1891.7	5111.8	5311.7	-199.9	4.4	8.3	-3.9
9/16/2014	ST	1521.7	594.1	927.7	1956.1	936.9	1019.3	6.1	7.0	-0.9
10/23/2014	AC	3206.7	1121.6	2085.1	3583.9	1285.9	2298.0	10.2	14.4	-4.2
12/5/2014	AC	2021.0	292.7	1728.3	2461.5	1584.1	877.4	5.7	7.8	-2.2
12/10/2014	ST	1745.9	1660.0	85.9	2133.1	1814.1	319.0	7.5	-	-
1/10/2015	AC	3022.5	1565.9	1456.5	3361.5	1747.0	1614.5	1.2	-	-
5/6/2015	AC	2001.2	1164.9	836.3	2461.6	1662.8	798.8	8.6	-	-
5/20/2015	CU	2639.5	741.6	1897.9	3217.5	914.7	2302.8	31.4	29.4	2.0
5/30/2015	AC	2150.1	954.9	1195.3	2581.1	1108.9	1472.2	4.2	9.9	-5.7
5/31/2015	AC	1702.9	1140.9	562.0	2171.1	1354.4	816.7	11.5	17.8	-6.3

Table 14 lists the statistics for Table 13, with σ_{error} representing the one-standard-deviation error. An inspection of the results shows that the correlations between the VIIRS CBH and CTH products are similar, at 0.59 and 0.71, respectively, while the correlations between the VIIRS COT product and the ARM site truth data are much stronger, at 0.91. Thus, it appears that the largest errors in the VIIRS CBH product results are associated with errors in the VIIRS CTH products.

In order to decouple the errors in the VIIRS CBH products from those in the VIIRS CTH products, further results were generated using the ARM CTH (truth) data in place of the VIIRS CTH products. First, the geometric cloud thicknesses were calculated from the VIIRS CTH and CBH products shown in Table 13. These cloud thicknesses were then subtracted from the ARM CTH (truth) data, and those "corrected" results are shown in column 2 of Table 15. Only columns that contain results affected by this substitution of the ARM CTH product for the VIIRS CTH product are shown in Table 15, i.e., columns 3 (VIIRS CBH), 5 (CBH error), 6 (VIIRS CTH), and 8 (CTH error) from Table 13. The rest of the columns from Table 13 are not shown to avoid redundancy.

Table 14. Daytime Subset Results. Statistics of the data from from Table 13. CBH and CTH correlations are similar and weak, while that of COT is much higher. Generated using the primary daytime processing method described in Section 3.3.2.1.

CBH			CTH			COT		
r	**Avg. Error (m)**	σ_{error} **(m)**	r	**Avg. Error (m)**	σ_{error} **(m)**	r	**Avg. Error**	σ_{error}
0.59	944.7	750.2	0.71	866.3	743.1	0.91	-3.4	3.2

Table 15. Daytime Subset (Corrected). Error of VIIRS CBH and other VIIRS cloud data products based upon comparisons with ARM site truth match-ups (same as Table 13), but with ground truth (ARM) CTH substituted for VIIRS CTH. Only updated columns are shown here (dates have not been changed). Generated using the primary daytime processing method described in Section 3.3.2.1.

Date	VIIRS CBH (m)	CBH Error (m)	VIIRS CTH (m)	CTH Error (m)
4/1/2014	567.8	-297.9	1003.2	0.0
4/2/2014	1387.6	-353.0	2043.9	0.0
5/30/2014	1638.4	101.2	2028.2	0.0
6/9/2014	1377.1	-92.6	1731.3	0.0
6/17/2014	1415.4	-96.8	1861.2	0.0
6/27/2014	1605.9	412.9	2082.5	0.0
7/31/2014	1259.2	-349.4	1759.9	0.0
9/1/2014	2767.8	1039.4	3400.2	0.0
9/6/2014	1224.0	-221.4	1725.6	0.0
9/10/2014	4909.9	2091.5	5311.7	0.0
9/16/2014	502.5	-91.6	936.9	0.0
10/23/2014	908.7	-212.9	1285.9	0.0
12/5/2014	1143.6	850.9	1584.1	0.0
12/10/2014	1426.9	-233.1	1814.1	0.0
1/10/2015	1408.0	-158.0	1747.0	0.0
5/6/2015	1202.4	37.5	1662.8	0.0
5/20/2015	336.7	-404.9	914.7	0.0
5/30/2015	677.9	-277.0	1108.9	0.0
5/31/2015	886.1	-254.8	1354.4	0.0

Table 16. Daytime Subset Comparison. A comparison of statistics of the data from from Tables 13 and 15. Ground truth (ARM) CTH is substituted for VIIRS CTH in Table 15, which greatly increases the CBH correlation and reduces the CBH error. COT is unchanged between Tables 13 and 15.

Table	CBH			CTH		
	r	Avg. Error (m)	(σ_{error}) (m)	r	Avg. Error (m)	(σ_{error}) (m)
13	0.59	944.7	750.2	0.71	866.3	743.1
15	0.83	78.4	627.4	1.00	0.0	0.0

The most obvious difference between Tables 13 and 15, shown in the comparison in Table 16, is the dramatically improved correlation between VIIRS CBH and ARM

CBH data after errors in VIIRS CTH are taken into account. This CBH correlation, which was 0.59 when the VIIRS CTH product was used to retrieve the VIIRS CBH product, improved to 0.83 when the ARM CTH (truth) data are used in place of the VIIRS CTH product. Additionally, the VIIRS CBH one-standard-deviation error (σ_{error}) improves from 750 m to 627 m, while the average VIIRS CBH error is reduced from 945 m to nearly 75 m, which allows the VIIRS CBH product to easily meet the system requirements listed in Table 1. Thus, the results obtained by using the ARM (truth) CTH product in the VIIRS CBH retrieval demonstrate that the theoretical basis of the VIIRS CBH algorithm is fundamentally sound, i.e., it validates the concept of converting COT into a geometric cloud thickness.

When applying the same statistical analysis and sensitivity methodology to all 156 cases of the complete, primary, daytime dataset (not shown here to save space), the correlations, mean errors, and error standard deviations improved for the full spectrum of CBH and upstream parameters, as shown in Table 17. The CBH results generated using the VIIRS CTH are shown in columns 3, 4, and 5, while the results from the "corrected" method (i.e., using ARM CTH in place of VIIRS CTH) are shown in columns 6, 7, and 8. Correlation improved from 0.20 to 0.31, while average error dropped from 957 m to 258 m, and σ_{error} decreased from 2020 m to 1704 m.

Improvement is even more substantial when applying this same analysis to the outlier-free dataset, show in Table 18. The improvement in CBH correlations for all daytime cases using the primary method is shown graphically in Figure 18. Red dots in the figure represent the "corrected" CBH, observed to be grouped much closer to the correlation line in the figure.

Table 17. Corrected Daytime CBH Comparison (Primary). A side-by-side comparison of CBH results for all primary, daytime VIIRS - ARM CBH match-up datasets by cloud type after ARM CTH truth data have been substituted for VIIRS CTH. Generated using the primary daytime processing method described in Section 3.3.2.1.

ARM Site Observations		VIIRS CBH			Corrected VIIRS CBH		
Cloud Type	*# of Cases*	r	*Avg. Error (m)*	σ_{error} *(m)*	r	*Avg. Error (m)*	σ_{error} *(m)*
ST	14	0.33	443.0	664.3	0.47	155.5	476.3
CU	82	0.17	1191.0	2461.0	0.31	496.8	1948.2
AC	60	0.26	757.6	1458.2	0.32	-44.8	1479.6
Total	**156**	**0.20**	**957.2**	**2019.8**	**0.31**	**257.8**	**1703.6**

Table 18. Corrected Daytime CBH Comparison with Outliers Removed (Primary). VIIRS - ARM CBH match-up datasets by cloud type after ARM CTH truth data has been substituted for VIIRS CTH. Outliers removed for CTH > 20,000 ft (6100 m) and CTH error (VIIRS CTH − ARM CTH) > 10,000 ft (3050 m, or < -10,000 ft/-3050 m), COT/EPS uncertainty greater than 10%, and EPS error (VIIRS EPS − ARM EPS) > 5 µm (or < - 5 µm). Generated using the primary daytime processing method described in Section 3.3.2.1.

ARM Site Observations		VIIRS CBH			Corrected VIIRS CBH		
Cloud Type	*# of Cases*	r	*Avg. Error (m)*	σ_{error} *(m)*	r	*Avg. Error (m)*	σ_{error} *(m)*
ST	14	0.33	443.0	664.3	0.47	155.5	476.3
CU	65	0.33	670.1	1165.6	0.51	296.9	1138.6
AC	55	0.39	850.3	1155.5	0.61	265.5	948.4
Total	**134**	**0.37**	**720.3**	**1120.4**	**0.55**	**269.3**	**1006.4**

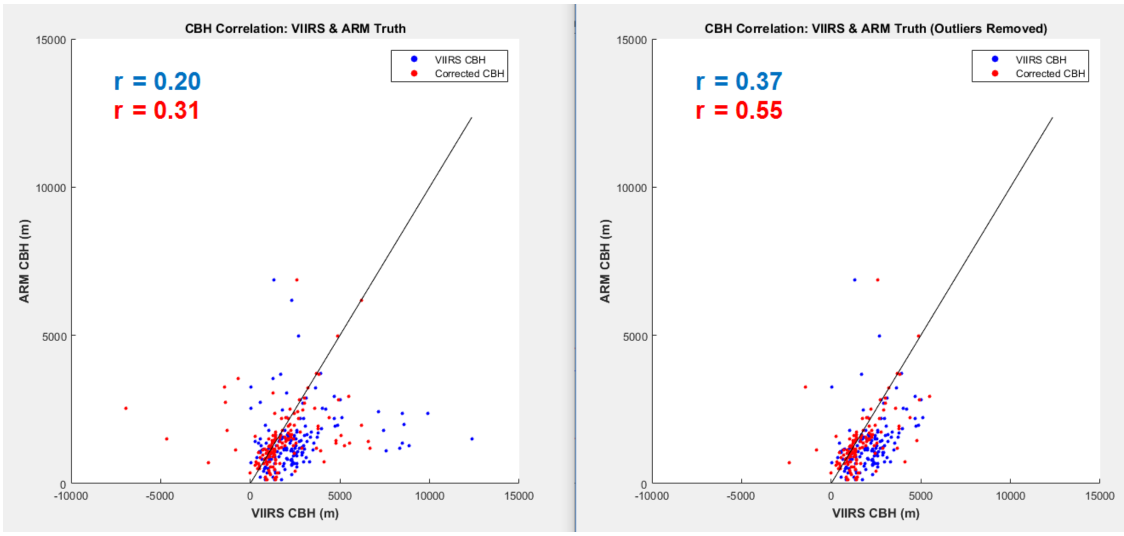

Figure 18. CBH Correlation Comparison. Correlation before (left) and after (right) outliers are removed. Correlation improves significantly after CTH error is removed (in red). Generated using the primary daytime processing method described in Section 3.3.2.1.

Similar results are shown using the alternate ARM CTH attenuation flag method (Tables 19 and 20). The highest correlation and lowest error for all cloud types are observed using the alternate approach, especially after CTH error and outliers have been removed (Table 20). This makes sense because ARM CTH values are closest to truth when using the alternate processing method.

Table 19. Corrected Daytime CBH (Alternate). VIIRS - ARM CBH match-up datasets by cloud type after ARM CTH truth data has been substituted for VIIRS CTH, using the alternate data processing method described in Section 3.3.2.2.

ARM Site Observations		**VIIRS CBH**			**Corrected VIIRS CBH**		
Cloud Type	*# of Cases*	r	*Avg. (m)*	σ_{error} *(m)*	r	*Avg. Error (m)*	σ_{error} *(m)*
ST	6	-0.08	648.2	737.8	0.78	-30.7	224.7
CU	42	0.22	1430.4	2625.2	0.39	653.0	1362.4
AC	15	0.34	605.9	1232.0	0.21	-509.9	1954.3
Total	**63**	**0.21**	**1159.6**	**2256.8**	**0.29**	**311.0**	**1532.1**

Table 20. Corrected Daytime CBH with Outliers Removed (Alternate). VIIRS - ARM CBH match-up datasets by cloud type after ARM CTH truth data has been substituted for VIIRS CTH, using the alternate data processing method described in Section 3.3.2.2. Outliers removed for CTH > 20,000 ft (6100 m) and CTH error (VIIRS CTH – ARM CTH) > 10,000 ft (3050 m, or < -10,000 ft/-3050 m), COT/EPS uncertainty greater than 10%, and EPS error (VIIRS EPS – ARM EPS) > 5 μm (or < - 5 μm).

ARM Site Observations		VIIRS CBH			Corrected VIIRS CBH		
Cloud Type	*# of Cases*	r	*Avg. Error (m)*	σ_{error} *(m)*	r	*Avg. Error (m)*	σ_{error} *(m)*
ST	6	-0.08	648.2	737.8	0.78	-30.7	224.7
CU	34	0.36	475.2	1061.9	0.77	297.4	511.5
AC	13	0.61	943.0	885.3	0.90	200.9	423.2
Total	**53**	**0.44**	**609.5**	**994.2**	**0.80**	**236.6**	**472.4**

Using both data processing methods, the most promising cloud type was stratus - the first four cases of which were collected from the well-established, permanent Lamont, OK site. When CTH ground truth was substituted for VIIRS CTH, as described above, the four Lamont stratus cases of the primary daytime dataset resulted in a 0.98 correlation, an average error of -180 m (i.e., low bias), and σ_{error} of 103 m. This demonstrates that the desired CBH accuracy listed in Table 1 (250 m) may be achievable for stratus clouds if a more accurate CTH retrieval is used. However, when 10 cases from the site at Graciosa, Portugal were added, the performance for stratus decreased to that shown in Tables 17 and 18. For the alternate daytime results, removal of CTH error resulted in a CBH correlation of 0.80, average error of 237 m, and σ_{error} of 472 m. VIIRS retrieval of CBH for stratus is by far the closest to satisfying the system specification objective (i.e., "desired") accuracy requirement listed in Table 1, and this is shown graphically in Figure 19. Numerous other analyses are also shown in this figure, including by other cloud types, with and without outliers removed, the CBH "correction" applied, for nighttime cases, etc. Only the primary daytime results are shown in this figure, and the number of cases for each analysis type is shown in parentheses. The same is shown for CTH retrievals in Figure 20, where it is clear that CTH fails, overall, to satisfy even the threshold (i.e., "required") system specification from Table 1.

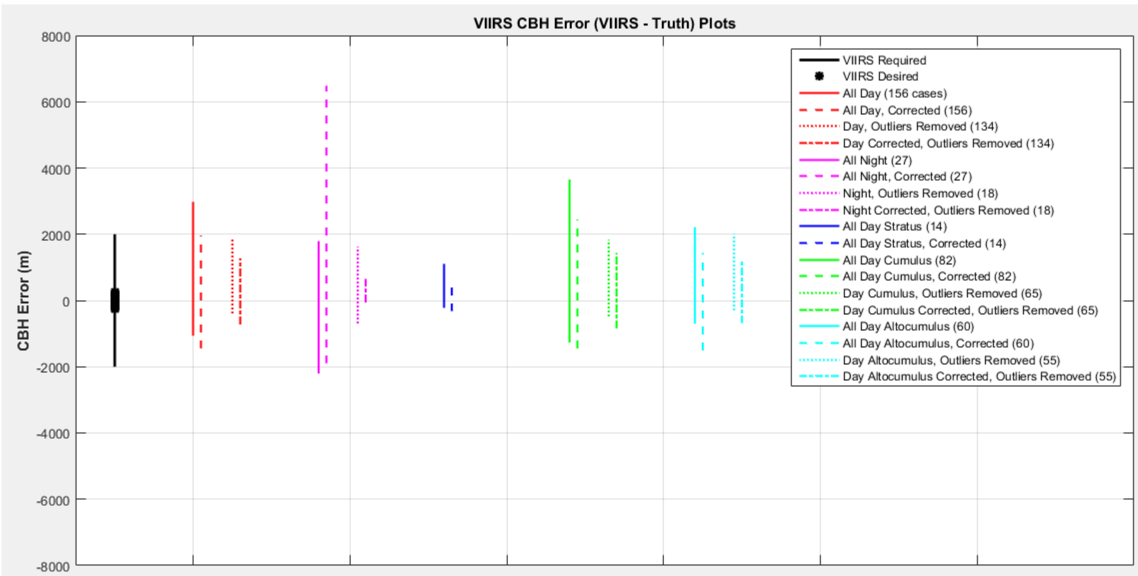

Figure 19. VIIRS CBH Error Plots. VIIRS CBH error compared to the specification requirements using the primary data processing method. The VIIRS System Specification Requirements from Table 1 are shown in black, where the "required" accuracy is the threshold accuracy, and the "desired" accuracy is the objective. All other colors are compared to this standard, including all daytime cases (in red), all nighttime cases (purple), daytime stratus (blue, no outliers), cumulus (green), and altocumulus (cyan). The order from top to bottom in the legend is the same order from left to right on the plot. Number of cases for each analysis type are in parentheses in the legend. "Corrected" cases use ARM CTH in place of VIIRS CTH. The corrected daytime stratus cases are closest to the desired accuracy, and corrected nighttime cases (all cloud types) with outliers removed are a close second.

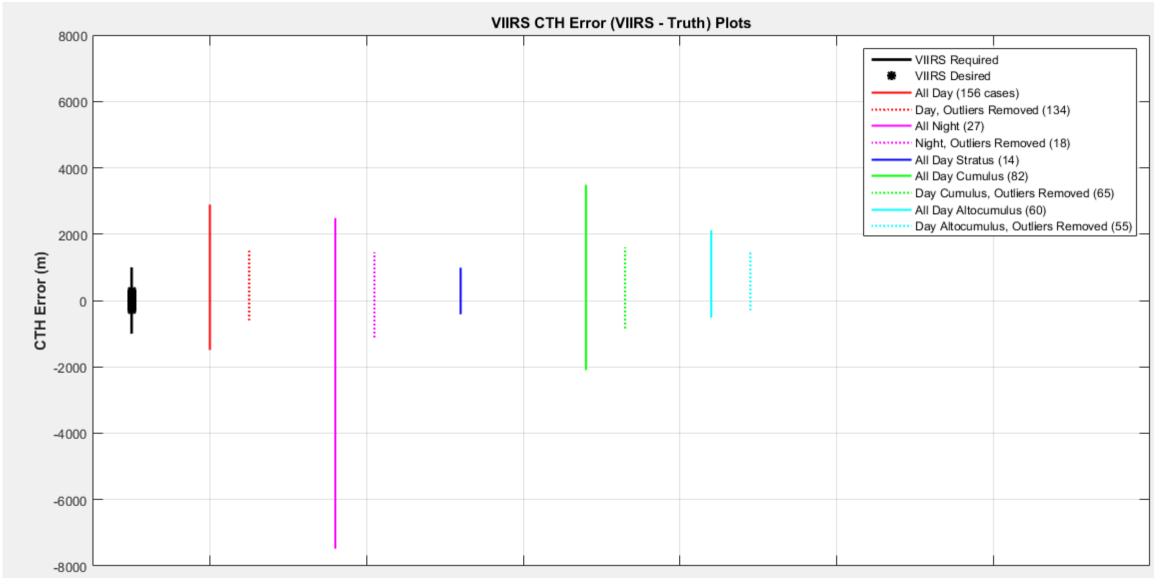

Figure 20. VIIRS CTH Error Plots. VIIRS CTH error compared to the specification requirements using the primary data processing method. The VIIRS System Specification Requirements from Table 1 are shown in black, where the "required" accuracy is the threshold accuracy, and the "desired" accuracy is the objective. Only the requirements for COT > 1 (over 95% of the cases) are shown here. All other colors are compared to this standard, including all daytime cases (in red), all nighttime cases (purple), daytime stratus (blue, no outliers), daytime cumulus (green), and daytime altocumulus (cyan). The order from top to bottom in the legend is the same order from left to right on the graph. Number of cases for each analysis type are in parentheses in the legend. The required accuracy from Table 1 isn't satisfied in most cases, with stratus as the exception.

4.3.2 COT Analysis: CBH Retrieval as a Function of COT.

As highlighted by Hutchison (2002), a retrieval of CBH using optical properties becomes increasingly unreliable at large values of COT. This was confirmed by Welch *et al.* (2008), who noted that CBH errors increased significantly for COT values greater than approximately 40. Out of the total 156 cases analyzed with the primary daytime method, eight contained VIIRS-calculated COT values greater than this threshold (i.e., 5%). CBH results were compared for different values of COT by placing cases in bins of 10 τ and using the corrected version of CBH (ARM CTH – VIIRS geometric thickness). Results are shown in Table 21, and it is clear that correlation decreases dramatically while error increases significantly for the cases of COT > 40, in agreement with the previous findings of Welch *et al.* (2008).

Table 21. Corrected Daytime CBH by Optical Thickness. VIIRS - ARM CBH match-up datasets, segregated by VIIRS-calculated COT and compared to ground truth after ARM CTH truth data have been substituted for VIIRS CTH. Generated using the primary daytime processing method described in Section 3.3.2.1.

VIIRS-calculated COT		**VIIRS CBH**		
COT Bin	*# of Cases*	*r*	*Avg. Error (m)*	σ_{error} *(m)*
COT < 10	92	0.34	610.0	1661.4
10 < COT < 20	44	0.19	70.3	1064.4
20 < COT < 30	7	-0.15	-906.6	1499.7
30 < COT < 40	5	0.14	-25.4	757.2
COT > 40	8	-0.31	-1564.1	3480.2

4.3.3 EPS Analysis: Replacing VIIRS EPS with Modal EPS Values.

The VIIRS EPS correlation was unexpectedly low in Section 4.1, Tables 7 and 8, which led to another sensitivity study consisting of replacing the VIIRS-retrieved EPS values with climatological averages based on cloud type, much like the climatological LWC values used in Equation 8. The modal EPS values from Table 4.2 in Liou (1992) were used, representing the values most likely to be sampled for a given cloud type: 3.5 µm for ocean stratus at Graciosa, 4.5 µm for stratus over land at Lamont, 3.75 µm for cumulus (splitting the difference between fair weather cumulus and cumulus congestus), and 5.0 µm for altocumulus. Retrievals using these EPS values were compared to the standard retrieval using VIIRS-calculated EPS values, and results are shown in Table 22. In all cases, the correlations increased with the modal EPS retrievals, but the errors increased, as well. In general, the modal EPS values resulted in a geometric cloud thickness that was too small; thus, the already-high CBH bias (i.e., VIIRS-calculated CBH generally higher than truth) increased even more. The σ_{error} also increased in all cases, with stratus being the one exception.

Table 22. Daytime Statistics using Modal EPS. VIIRS - ARM match-up datasets, comparing the usual retrieval to one that uses modal EPS values rather than VIIRS-calculated EPS values. The far right columns use modal EPS values and show a higher correlation with increased error.

ARM Site Observations		**VIIRS CBH**			**Modified VIIRS CBH**		
Cloud Type	*# of Cases*	r	*Avg. Error (m)*	σ_{error} *(m)*	r	*Avg. Error (m)*	σ_{error} *(m)*
ST	14	0.33	443.0	664.3	0.35	638.9	657.9
CU	82	0.17	1191.0	2461.0	0.23	1758.0	2518.6
AC	60	0.26	757.6	1458.2	0.40	1345.1	1533.5
Total	**156**	**0.20**	**957.2**	**2019.8**	**0.29**	**1498.8**	**2087.5**

4.4 Findings and Discussion

Daytime results showed a large overall positive bias for both CBH and CTH, indicating that VIIRS is systematically overestimating both. Nighttime results, on the other hand, showed a small negative bias for CBH and a large negative bias for CTH. For both daytime datasets and the one nighttime dataset, correlation was low while error was high. The removal of outliers demonstrated how significantly they were impacting these datasets. VIIRS cloud products include quality flags that may be able to help screen such outliers for future studies, but they were not included in this research. A previous finding that a COT threshold of approximately 40 should be used as an effective upper limit for reliable CBH retrieval appears valid, as well. Using average EPS values as a function of cloud type in place of the VIIRS-calculated EPS offers higher correlation with ground truth CBH, but only at the cost of higher CBH errors. The most significant finding, though, was the large source of error in VIIRS CTH.

Comparisons between results obtained from the VIIRS CTH product, shown in Table 14 for the subset of Lamont cases, with the system requirements listed in Table 1, show that the CTH product failed to satisfy EDR thresholds. With a correlation of 0.71 compared to the ARM CTH truth data, total CTH error (average error $\pm\sigma_{error}$) exceeded 1.6 km, while the threshold (required) σ_{error} accuracy is 1 km, and the objective (desired) accuracy requirement is 300 m (shown graphically in Figure 20). The performance is even worse for the complete set of primary daytime cases, shown in Tables 7 and 10, where correlations with and without outliers are 0.27 and 0.50, respectively. The poor performance of the VIIRS CTH retrieval reiterates the findings of the cal/val team (Seaman *et al.*, 2014; Noh *et al.*, 2015). Thus, it becomes clear that future research to obtain more useful information on the CBH retrieved from VIIRS data must focus on improving the VIIRS CTH product. Other VIIRS cloud products used in the VIIRS CBH algorithm appear adequate, since the correlation between VIIRS and ARM (truth) COT data was 0.91 for the subset in Table 14. Thus, only small errors were introduced into the VIIRS CBH product by the retrieved microphysical cloud properties products.

Previous research has shown various methods to improve the accuracy of CTH of water clouds retrieved from environmental satellite data. One method placed added emphasis on the ancillary moisture profile information from NWP models to compensate for errors in the MODIS CTT product (Hutchison *et al.*, 2006a) when converting from CTT to CTH. For lower-level water clouds, with cloud top pressures greater than about 700 mb, both the MODIS and VIIRS CTH algorithms convert from CTT to CTH based solely on atmospheric temperature and geopotential height profiles without regard for atmospheric humidity profiles

(Platnick *et al.*, 2003; Menzel *et al.*, 2010). Errors as small as 3 K in the CTT product can result in placing the CTH in regions where humidity levels do not support the presence or sustainment of clouds. Thus, CTH products become grossly in error and unsuitable for use in NWP applications (Hutchison *et al.*, 2006a). An improved procedure for the conversion from CTT to CTH was demonstrated. However, it has not been proven that moisture forecast fields created by NWP models, such as the Weather Research and Forecasting (WRF) Model (Skamarock and Klemp, 2008), produce moisture forecast fields that would be useful in reducing existing errors obtained with the MODIS and VIIRS approaches.

V. Conclusion

5.1 Summary of Results

Results were generated for coincident VIIRS-ARM observations using two daytime methods and one nighttime method. All of the VIIRS cloud products had weak correlations with their corresponding ARM products, except for COT. Removal of outliers for cumuliform cloud cases led to a significant improvement in the retrieval for those cloud types. Furthermore, CBH products were shown to be very strongly correlated with CTH error when VIIRS CTH values were replaced with ARM CTH truth values, which produced a "corrected" CBH product. This corrected product increased the correlation by an average of 46% for all cases (i.e., day and night). Average error for daytime cases was reduced by an average of 217%, while daytime σ_{error} was reduced by 47%. Nighttime errors didn't improve until the outliers were removed, after which the average error fell by 56%, and σ_{error} fell by 225%. Additionally, an effective upper limit for COT in the retrieval of CBH was shown to be approximately 40, corroborating an earlier finding by Welch *et al.* (2008). However, this value was exceeded only 5% of the time in the primary daytime dataset. Finally, replacing VIIRS EPS values with modal EPS values by cloud type did not yield any noteworthy improvement in CBH retrieval.

The current VIIRS CBH product is not yet accurate enough to be used to support operational users, especially in austere locations where ancillary data are scarce. However, this study concludes that the CBH algorithm, which uses cloud microphysical and optical properties to determine the geometric cloud thickness, is valid and capable of providing useful CBH products. This is especially true for the relatively homogeneous, water-phase stratiform clouds that tend to have the lowest cloud bases, and thus create the most hazardous conditions for the full spectrum of aviation operations. Results were similar for the alternate data processing method, as well, which served to enhance the findings of the primary daytime dataset. A robust error budget was initiated in this study, with hopes of expanding upon it in the future in order to better understand the sources of error in the VIIRS CBH algorithm.

5.2 Recommendations for Future Research

Future research efforts should initially focus on improving the accuracy of CTH retrieval using other remote sensing techniques, such as observations in the O_2 A-band (Fischer *et al.*, 2003), or methodologies that use NWP moisture profiles to compensate for errors in the CTT to CTH conversion, as described in Section 4.4. As for further evaluation of the VIIRS CBH algorithm, one could expand upon the research presented within this paper by evaluating the 6-km EDR product in a similar manner to the 1-km IP evaluated here. Moreover, ground-based MMCR could be used in conjunction with ground-based MPL in order to provide a better set of CTH truth data, where MMCR would determine the CTH in those cases when the MPL becomes fully attenuated. Otherwise, CTH truth data could be retrieved from the CALIOP/CPR product, which is essentially just a space-based version of this retrieval method. Finally, quality flags from the VIIRS cloud products could also be incorporated in order to screen the types of outliers identified in this document. For example, the COP IP algorithm will flag an excessively large, unrealistic EPS $> 50\,\mu m$ for both ice and water clouds (JPSS OAD for VIIRS COP, 2013). Research such as this can aid the future operational user in determining when CBH retrievals are most likely reliable versus when they are of questionable value.

Appendix . Acronym and Abbreviation List

2GL - 2B-GEOPROF (Geometrical Profile) -Lidar

3DNEPH - 3-Dimensional Nephanalysis

30SMPLCMASK1ZWANG - 30-Second MPL Cloud Mask, 1st Z. Wang *et al.*

A-Train - Afternoon Train

AC - Altocumulus

AFGWC - Air Force Global Weather Central

AGL - Above Ground Level

AMS - American Meteorological Society

ARM - Atmospheric Radiation Measurement

ARSCL - Active Remote Sensing of Clouds

AS - Altostratus

ATBD - Algorithm Theoretical Basis Document

ATMS - Advanced Technology Microwave Sounder

BT - Brightness Temperature

CALIOP - Cloud-Aerosol Lidar with Orthogonal Polarization

CALIPSO - Cloud-Aerosol Lidar and Infrared Pathfinder Satellite Observations

CBH - Cloud Base Height

CC - Cirrocumulus

CCL - Cloud Cover/Layers

CDFS II - Cloud Depiction and Forecast System II

CEIL - Ceilometer

CERES - Clouds and the Earth's Radiant Energy System

CFLOS - Cloud Free Line of Sight

CI - Cirrus

CLASS - Comprehensive Large Array-data Stewardship System

CLT - Cloud Layer/Type

CM - Cloud Mask

COD - Cloud Optical Depth

COP - Cloud Optical Properties

COT - Cloud Optical Thickness

CPBMSR - Cloud Products Beta Maturity Status Report

CPR - Cloud Profiling Radar

CrIS - Cross-track Infrared Sounder

CTH - Cloud Top Height

CTP - Cloud Top Parameters

CTT - Cloud Top Temperature

CU - Cumulus

DMSP - Defense Meteorological Satellite Program

DOC - Department of Commerce

DOD - Department of Defense

DW - Day-Water

EDR - Environmental Data Record

ENA - Eastern North Atlantic

EOS - Edge Of Scan

EPS - Effective Particle Size

ET - Effective Top

GFS - Global Forecast System

GMTCO - Moderate-resolution, Terrain-corrected Geolocation

HDF5 - Hierarchical Data Format 5

HSR - Horizontal Spatial Resolution

IDPS - Interface Data Processing Segment

InGaAs - Indium Gallium Arsenide

IP - Intermediate Product

IPO - Integrated Program Office

Isl. - Island

IWC - Ice Water Content

IWP - Ice Water Path

JPSS - Joint Polar Satellite System

LANDSAT - Land Satellite

LBLE - Line-By-Line Equivalent

LITE - Lidar In-space Technology Experiment

LUT - Look-Up Table

LWC - Liquid Water Content

LWP - Liquid Water Path

MATLAB - Matrix Laboratory

MFRSR - Multi-Filter Rotating Shadowband Radiometer

MFRSRCLDOD1MIN - MFRSR COD, 1-Minute

MMCR - Millimeter-wave Cloud Radar

MODIS - Moderate-resolution Imaging Spectroradiometer

MPL - Micro-Pulse Lidar

MSL - Mean Sea Level

MWR - Microwave Radiometer

NASA - National Aeronautics and Space Administration

NCEP - National Centers for Environmental Prediction

NDW - Non-Day-Water

NetCDF - Network Common Data Form

NIR - Near Infrared

NLSM - Nonlinear Least Squares Method

NOAA - National Oceanic and Atmospheric Administration

NOGAPS - Navy Operational Global Atmospheric Prediction System

NPOESS - National Polar-orbiting Operational Environmental Satellite System

NPP - NPOESS Preparatory Project

NSA - North Slope of Alaska

NWP - Numerical Weather Prediction

NWS - National Weather Service

OAD - Operational Algorithm Description

OK - Oklahoma

OMPS - Ozone Mapping and Profiler Suite

PCT - Probability of Correct Typing

PFAAST - Pressure-layer Fast Algorithm for Atmospheric Transmittances

PPC - Perform Parallax Correction

RT - Radiative Transfer

RTM - Radiative Transfer Model

RTNEPH - Real-Time Nephanalysis

SDR - Sensor Data Record

SGP - Southern Great Plains

SNR - Signal-to-Noise Ratio

ST - Stratus

STAR - Center for Satellite Applications and Research

TOA - Top-of-Atmosphere

TOC NDVI - Top-Of-Canopy Normalized Difference Vegetation Index

TWP - Tropical Western Pacific

VAP - Value-Added Product

VCEIL - Vaisala Ceilometer

VCM - VIIRS Cloud Mask

VIIRS - Visible Infrared Imaging Radiometer Suite

WRF - Weather Research and Forecasting

WWMCA - World Wide Merged Cloud Analysis

Bibliography

Ackerman, T. P., and G. M. Stokes, 2003: The atmospheric radiation measurement program. *Physics Today*, **56**, 38–44.

American Meteorological Society (AMS) Glossary of Meteorology, 2015a: Ceiling. URL http://glossary.ametsoc.org/wiki/Ceiling.

American Meteorological Society (AMS) Glossary of Meteorology, 2015b: Cloud base. URL http://glossary.ametsoc.org/wiki/Cloud_base.

Atmospheric Radiation Measurement (ARM) Belfort Laser Ceilometer (BLC), 2015: URL https://www.arm.gov/instruments/blc.

Atmospheric Radiation Measurement (ARM) Climate Research Facility, 1996a: Updated hourly, Ceilometer (CEIL), Jun. 2013 - Oct. 2015; Jun. 2013 - Dec. 2014; Oct. 2013 - Oct. 2015; Jan. 2014 - Dec. 2014, 36° 36' 18.0" N, 97° 29' 6.0" W; 12° 25' 28.56" S, 130° 53' 29.75" E; 39° 5' 29.68" N, 28° 1' 32.34" W; 3° 12' 46.70" S, 60° 35' 53.00" W: Southern Great Plains (SGP) Central Facility, Lamont, OK (C1); Tropical Western Pacific (TWP) Facility, Darwin, Australia (C3); East North Atlantic (ENA) Central Facility, Graciosa Island, Azores, Portugal (C1); ARM Mobile Facility (MAO) Manacapuru, Amazonas, Brazil; AMF1 (M1), lowest cloud base height. Compiled by V. Morris and B. Ermold. ARM Data Archive: Oak Ridge, Tennessee, USA. Data set accessed 2015-08-27 at http://dx.doi.org/10.5439/1181954.

Atmospheric Radiation Measurement (ARM) Climate Research Facility, 1996b: Updated hourly, Cloud mask from Micropulse Lidar (30SMPLCMASK1ZWANG). Jun. 2013 - Oct. 2015; Jun. 2013 - Dec. 2014; Oct. 2013 - Oct. 2015; Jan. 2014 - Dec. 2014, 36° 36' 18.0" N, 97° 29' 6.0" W; 12° 25' 28.56" S, 130° 53' 29.75" E; 39° 5' 29.68" N, 28° 1' 32.34" W; 3° 12' 46.70" S, 60° 35' 53.00" W: Southern Great Plains (SGP) Central Facility, Lamont, OK (C1); Tropical Western Pacific (TWP) Facility, Darwin, Australia (C3); East North Atlantic (ENA) Central Facility, Graciosa Island, Azores, Portugal (C1); ARM Mobile Facility (MAO) Manacapuru, Amazonas, Brazil; AMF1 (M1), cloud top height. Compiled by C. Sivaraman and L. Riihimaki. ARM Data Archive: Oak Ridge, Tennessee, USA. Data set accessed 2015-09-15 at http://dx.doi.org/10.5439/1027736.

Atmospheric Radiation Measurement (ARM) Climate Research Facility, 1997: Updated hourly, Cloud Optical Properties from MFRSR Using Min Algorithm (MFRSRCLDOD1MIN). Jun. 2013 - Jul. 2015; Jun. 2013 - Oct. 2014, 36° 36' 18.0" N, 97° 29' 6.0" W; 12° 25' 28.56" S, 130° 53' 29.75" E: Southern Great Plains (SGP) Central Facility, Lamont, OK (C1); Tropical Western Pacific (TWP) Facility, Darwin, Australia (C3), cloud optical depth and effective particle size. Compiled by Y. Shi, Q. Min and L. Riihimaki. ARM Data Archive: Oak

Ridge, Tennessee, USA. Data set accessed 2015-09-07 at http://dx.doi.org/10.5439/1027296.

Atmospheric Radiation Measurement (ARM) Climate Research Facility Annual Report, 2015: URL http://www.arm.gov/publications/annual-reports/docs/doe-sc-arm-15-084.pdf, DOE/SC-ARM-15-084.

Berendes, T., S. K. Sengupta, R. M. Welch, B. A. Wielicki, and M. Navar, 1992: Cumulus cloud base height estimation from high spatial resolution Landsat data: a Hough Transform approach. *IEEE Transactions on Geoscience and Remote Sensing*, **30 (3)**, 430–443.

Bevington, P. R., 1969: *Data reduction and error analysis for the physical sciences.* McGraw-Hill, New York.

Campbell, J. R., D. L. Hlavka, E. J. Welton, C. J. Flynn, D. D. Turner, J. D. Spinhirne, V. S. Scott, and I. H. Hwang, 2002: Full-time, eye-safe cloud and aerosol lidar observation at Atmospheric Radiation Measurement Program sites: Instruments and data processing. *Journal of Atmospheric and Oceanic Technology*, **19**, 431–442.

Cao, C., and Coauthors, 2013: VIIRS Sensor Data Record (SDR) User's Guide, Version 1.2. Tech. Rep. NESDIS 142A, NOAA, Washington, DC. URL http://www.star.nesdis.noaa.gov/smcd/spb/nsun/snpp/VIIRS/VIIRS_SDR_Users_guide.pdf.

Clothiaux, E. E., G. G. Mace, T. P. Ackerman, T. J. Kane, J. D. Spinhirne, and V. S. Scott, 2008: An automated algorithm for detection of hydrometeor returns in micropulse lidar data. *Journal of Atmospheric and Oceanic Technology*, **15**, 1035–1042.

Clothiaux, E. E., M. A. Miller, B. Albrecht, T. P. Ackerman, J. Verlinde, D. M. Babb, R. M. Peters, and W. J. Syrett, 1995: An evaluation of a 94-ghz radar for remote sensing of cloud properties. *Journal of Atmospheric and Oceanic Technology*, **12 (2)**, 201–229.

Coulter, R., 2012: Micropulse Lidar (MPL) Handbook. Department of Energy Atmospheric Radiation Measurement (ARM) Climate Research Facility, Technical Report TR-019.

Dowling, D. R., and L. F. Radke, 1990: A summary of the physical properties of cirrus clouds. *Journal of Applied Meteorology*, **29**, 970–978.

Fischer, J., R. Preusker, and C. Rathke, 2003: Cloud top pressure from geo-stationary satellite observations in the oxygen A-band. *EUMETSAT Technical Note.*

Forsythe, J. M., T. H. Vonder-Haar, and D. L. Reinke, 2000: Cloud-base height estimates using a combination of meteorological satellite imagery and surface reports. *Journal of Applied Meteorology*, **39**, 2336–2347.

Fye, F. K., 1978: The Air Force Global Weather Central (AFGWC) Automated Cloud Analysis Model. AFGWC Technical Memorandum 78-002.

Gupta, S. K., 1989: A parameterization for longwave surface radiation from sun-synchronous satellite data. *Journal of Climate*, **2**, 305–320.

Hamill, T. M., R. P. D'Entremont, and J. T. Bunting, 1992: A description of the Air Force Real-Time Nephanalysis Model. *Weather and Forecasting*, **7 (2)**, 288–306.

Heidinger, A., 2014: Validated Stage 1 Science Maturity Review for VIIRS Cloud Top Height and Daytime Optical and Microphysical Products. URL http://www.star.nesdis.noaa.gov/jpss/documents/meetings/2014/EDRVal1/03a-Clouds_part1.pptx.

Heymsfield, A. J., and C. M. R. Platt, 1984: A parameterization of particle size spectrum of ice clouds in terms of the ambient temperature and ice water content. *Journal of the Atmospheric Sciences*, **41**, 846–855.

Horsman II, S. J., 2007: An Assessment of the World Wide Merged Cloud Analysis using Interactive Graphics. Master's Thesis, Naval Postgraduate School, Monterey, CA, URL http://www.dtic.mil/dtic/tr/fulltext/u2/a470121.pdf.

Hutchison, K. D., 1998: VIIRS Cloud Base Height Algorithm Theoretical Basis Document (ATBD), Version 1.0. URL http://npp.gsfc.nasa.gov/sciencedocs/2015-06/474-00045_VIIRS_Cloud_Base_Height_ATBD_Rev-_20110422.pdf, latest version: April 2011, Lanham, MD Raytheon Information Technology and Scientific Services.

Hutchison, K. D., 2002: The retrieval of cloud base heights from MODIS and three-dimensional cloud fields from NASA's EOS Aqua mission. *International Journal of Remote Sensing*, **23 (24)**, 5249–5265.

Hutchison, K. D., and A. P. Cracknell, 2005: *Visible Infrared Imager Radiometer Suite: A New Operational Cloud Imager*. CRC Press, Boca Raton FL.

Hutchison, K. D., B. Hauss, B. D. Iisager, H. Agravante, R. Mahoney, A. Sei, and J. M. Jackson, 2010: Differentiating between clouds and heavy aerosols in sun-glint regions. *Journal of Atmospheric and Oceanic Technology*, **27 (6)**, 1085–1094.

Hutchison, K. D., A. K. Heidinger, T. J. Kopp, B. D. Iisager, and R. A. Frey, 2014: Comparisons between VIIRS cloud mask performance results from manually generated cloud masks of VIIRS imagery and CALIOP-VIIRS match-ups. *International Journal of Remote Sensing*, **35 (13)**, 4905–4922.

Hutchison, K. D., B. Iisager, T. Kopp, and J. M. Jackson, 2008: Distinguishing aerosols from clouds in global, multispectral satellite data with automated cloud classification algorithms. *Journal of Atmospheric and Oceanic Technology*, **25**, 501–518.

Hutchison, K. D., B. D. Iisager, and B. I. Hauss, 2012: The use of global synthetic data for pre-launch tuning of the VIIRS cloud mask algorithm. *International Journal of Remote Sensing*, **33**, 1400–1423.

Hutchison, K. D., R. L. Mahoney, E. F. Vermote, T. J. Kopp, J. M. Jackson, A. Sei, and B. D. Iisager, 2009: A geometry-based approach to identifying cloud shadows in the VIIRS cloud mask algorithm. *Journal of Atmospheric and Oceanic Technology*, **26**, 1388–1397.

Hutchison, K. D., T. Pekker, and S. Smith, 2006a: Improved retrievals of cloud boundaries from modis for use in air quality modeling. *Atmospheric Environment*, **40**, 5798–5806.

Hutchison, K. D., J. K. Roskovensky, J. M. Jackson, A. K. Heidinger, T. J. Kopp, M. J. Pavolonis, and R. Frey, 2005: Automated cloud detection and classification of data collected by the VIIRS. *International Journal of Remote Sensing*, **26**, 4681–4706.

Hutchison, K. D., and T. T. Wilheit, 2000: An approach for retrieving 3-dimensional cloud fields from data collected by NASA's EOS Aqua mission. *Proceedings of the EUMETSAT Meteorological Satellite Data User's Conference, Bologna, Italy.*

Hutchison, K. D., E. Wong, and S. C. Ou, 2006b: Cloud base heights retrieved during night-time conditions with MODIS data. *International Journal of Remote Sensing*, **27 (14)**, 2847–2862.

JPSS Algorithm Maturity, 2015: URL http://www.star.nesdis.noaa.gov/jpss/AlgorithmMaturity.php.

JPSS Common Data Format Control Book (CDFCB) - External Volume VI - Ancillary Data, Auxiliary Data, Messages, and Reports, 2014: URL http://npp.gsfc.nasa.gov/sciencedocs/2015-06/474-00001-06_JPSS-CDFCB-X-Vol-VI_0123D.pdf, JPSS Document 474-00001-06-B0123.

JPSS Level 1 Requirements Supplement (JPSS REQ), Version 2.9, 2013: URL http://www.star.nesdis.noaa.gov/smcd/spb/nsun/snpp/ATMS/JPSS_L1RDS-F_v2.9_Rev_A.1.pdf, JPSS Document JPSS-REQ-1002.

JPSS Operational Algorithm Description (OAD) Document for VIIRS Cloud Base Height (CBH) Intermediate Product (IP) Software, 2013: URL http://npp.gsfc.nasa.gov/sciencedocs/2015-06/474-00084_OAD-VIIRS-CBH-IP_B.pdf, JPSS Document 474-00084, Revision B.

JPSS Operational Algorithm Description (OAD) Document for VIIRS Cloud Cover/Layers (CCL) and Generate Cloud EDR (GCE) Software, 2013: URL http://npp.gsfc.nasa.gov/sciencedocs/2015-06/474-00085_OAD-VIIRS-CCL-GCE-EDR_D.pdf, JPSS Document 474-00085, Revision D.

JPSS Operational Algorithm Description (OAD) Document for VIIRS Cloud Mask (VCM) IP Software, 2015: URL http://npp.gsfc.nasa.gov/sciencedocs/2015-08/474-00062_OAD-VIIRS-Cloud-Mask-IP_I.pdf, JPSS Document 474-00062, Revision I.

JPSS Operational Algorithm Description (OAD) Document for VIIRS Cloud Optical Properties (COP) Intermediate Product (IP) Software, 2013: URL http://npp.gsfc.nasa.gov/sciencedocs/2015-06/474-00074_OAD-VIIRS-COP-IP_C.pdf, JPSS Document 474-00074, Revision C.

JPSS Operational Algorithm Description (OAD) Document for VIIRS Cloud Top Parameters (CTP) Environmental Data Record (EDR) Software, 2013: URL http://npp.gsfc.nasa.gov/sciencedocs/2015-06/474-00083_OAD-VIIRS-CTP-EDR_B.pdf, JPSS Document 474-00083, Revision B.

JPSS Operational Algorithm Description (OAD) Document for VIIRS Perform Parallax Correction (PPC) Intermediate Product (IP) Software, 2013: JPSS Document 474-00088, Revision B.

JPSS VIIRS Cloud Cover/Layers (CCL) Algorithm Theoretical Basis Document (ATBD), 2011: URL http://npp.gsfc.nasa.gov/sciencedocs/2015-06/474-00044_Rev-Baseline.pdf, JPSS Document 474-00045.

JPSS VIIRS Cloud Mask (VCM) Algorithm Theoretical Basis Document (ATBD), 2014: URL http://npp.gsfc.nasa.gov/sciencedocs/2015-06/474-00033_ATBD-VIIRS-Cloud-Mask_E.pdf, JPSS Document 474-00033, Revision E.

JPSS VIIRS Cloud Top (CT) Algorithm Theoretical Basis Document (ATBD), 2012: URL http://npp.gsfc.nasa.gov/sciencedocs/2015-06/474-00041_ATBD-Cloud-Top_A.pdf, JPSS Document 474-00041, Revision A.

JPSS VIIRS Earth Gridding Algorithm Theoretical Basis Document (ATBD), 2014: URL http://npp.gsfc.nasa.gov/sciencedocs/2015-06/474-00028_ATBD-VIIRS-Earth-Gridding_B.pdf, JPSS Document 474-00028, Revision B.

Kidder, S. Q., and T. H. Vonder-Haar, 1995: *Satellite Meteorology: An Introduction*. Academic Press, San Diego CA.

Kiess, R. B., and W. M. Cox, 1988: The Air Force Global Weather Central (AFGWC) Automated Real-Time Cloud Analysis Model. AFGWC Technical Note 88/001.

Kopp, T. J., and Coauthors, 2014: The VIIRS Cloud Mask: Progress in the first year of S-NPP toward a common cloud detection scheme. *Journal of Geophysical Research: Atmospheres*, **119**, 2441–2456.

Kratz, D. P., 1995: The correlated k-distribution technique as applied to the AVHRR channels. *Journal of Quantitative Spectroscopy and Radiative Transfer*, **53**, 501–517.

Lee, T. E., S. D. Miller, F. J. Turk, C. Schueler, R. Julian, S. Deyo, P. Dills, and S. Wang, 2006: The NPOESS VIIRS day/night visible sensor. *Bulletin of the American Meteorological Society*, **87 (2)**, 191–199.

Lhermitte, R. M., 1988: Cloud and precipitation remote sensing at 94 GHz. *IEEE Transactions on Geoscience and Remote Sensing*, **26 (3)**, 207–216.

Liou, K. N., 1980: *An Introduction to Atmospheric Radiation*, International Geophysics Series, Vol. 26. Academic Press, New York.

Liou, K.-N., 1992: *Radiation and Cloud Processes in the Atmosphere*. Oxford University Press, New York.

Liou, K. N., S. C. Ou, Y. Takano, F. P. J. Valero, and T. P. Ackerman, 1990: Remote sounding of the tropical cirrus cloud temperature and optical depth using 6.5 and 10.5 micron radiometers during STEP. *Journal of Applied Meteorology*, **29**, 715–726.

MacQueen, J., 1967: Some methods for classification and analysis of multivariate observations. *Proceedings of the Fifth Berkeley Symposium on Mathematical Statistics and Probability*, L. M. L. Cam, and J. Neyman, Eds., University of California Press, Berkeley and Los Angeles, CA, Vol. I: Statistics, 281–297.

Menzel, W. P., R. A. Frey, and B. A. Baum, 2010: MODIS Cloud Top Properties and Cloud Phase Algorithm Theoretical Basis Document (ATBD), Version 8. URL http://modis.gsfc.nasa.gov/data/atbd/atbd_mod04.pdf.

Michalsky, J. J., J. A. Schlemmer, W. E. Berkheiser, J. L. Berndt, L. C. Harrison, N. S. Laulainen, N. R. Larson, and J. C. Barnard, 2001: Multiyear measurements of aerosol optical depth in the atmospheric radiation measurement and quantitative links programs. *Journal of Geophysical Research*, **106**, 12 099–12 107.

Min, Q., M. Duan, and R. Marchand, 2003: Validation of surface retrieved cloud optical properties with in situ measurements at the Atmospheric Radiation Measurement Program (ARM) South Great Plains site. *Journal of Geophysical Research*, **108 (D17)**.

Min, Q., and L. C. Harrison, 1996: Cloud properties derived from surface MFRSR measurements and comparison with GOES results at the ARM SGP site. *Geophysical Research Letters*, **23 (13)**, 1641–1644.

Morris, V. R., 2012: Vaisala Ceilometer (VCEIL) Handbook. Department of Energy Atmospheric Radiation Measurement (ARM) Climate Research Facility, Technical Report TR-020.

Nakajima, T., and M. D. King, 1990: Determination of the optical thickness and effective particle radius of cloud from reflected solar radiation measurements, Part I: Theory. *Journal of the Atmospheric Sciences*, **47**, 1878–1893.

NASA Suomi NPP Brochure, 2015: URL http://www.nasa.gov/pdf/596329main_NPP_Brochure_ForWeb.pdf.

NASA Suomi NPP Mission Page, 2015: URL http://www.nasa.gov/mission_pages/NPP/main/index.html.

Noh, Y.-J., J. Forsythe, C. Seaman, S. Miller, M. Rogers, D. Lindsey, and A. Heidinger, 2015: Enterprise Cloud Base: VIIRS Cloud Base Height Algorithm Improvement and Evaluation Using CloudSat. URL ftp://ftp.cira.colostate.edu/ftp/ynoh/VIIRS_CAL_VAL/docs/Session7e_CIRA_Noh-etal_Enterprise_Cloud_Base_2015JPSS_Sci_Meeting.pptx, Proceedings of the 2015 STAR JPSS Annual Science Team Meeting, College Park, MD.

Ou, S., K. N. Liou, Y. Takano, G. J. Higgins, A. George, and R. L. Slonaker, 2004: JPSS Cloud Effective Particle Size and Cloud Optical Thickness Algorithm Theoretical Basis Document (ATBD). URL http://npp.gsfc.nasa.gov/sciencedocs/2015-06/474-00042_ATBD-VIIRS-Cloud-EPS-COT_A.pdf, y2393, Version 5, Revision 2 (latest version, April 2014), Raytheon ITSS.

Ou, S. C., K. N. Liou, W. M. Gooch, and Y. Takano, 1993: Remote sensing of cirrus cloud parameters using advanced very-high-resolution radiometer 3.7- and 10.9 micron channels. *Applied Optics*, **32**, 2171–2180.

Ou, S. C., Y. Takano, K. N. Liou, G. J. Higgins, A. George, and R. Slonaker, 2003: Remote sensing of cirrus cloud optical thickness and effective particle size for the NPOESS VIIRS: sensitivity to instrument noise and uncertainties in environmental parameters. *Applied Optics*, **42 (36)**, 7202–7214.

Pavolonis, M. J., 2014: Personal conversation.

Pavolonis, M. J., and A. K. Heidinger, 2004: Daytime cloud overlap detection from AVHRR and VIIRS. *Journal of Applied Meteorology*, **43 (5)**, 762–778.

Pavolonis, M. J., and A. K. Heidinger, 2005: Advancements in identifying cirrus and multilayered cloud systems from operational satellite imagers at night. Proceedings of SPIE 5658, doi:10.1117/12.57764.

Pearson, D. C., 2002: VFR Flight Not Recommended: A Study of Weather-Related Fatal Aviation Accidents. Tech. Rep. SR SSD 2002-18, NOAA/NWS Atlanta Center Weather Service Unit. URL http://www.srh.noaa.gov/topics/attach/html/ssd02-18.htm.

Petty, G. W., 2006: *A First Course in Atmospheric Radiation*. 2nd ed., Sundog Publishing, Madison WI.

Platnick, S., M. D. King, S. A. Ackerman, W. P. Menzel, B. A. Baum, J. C. Riedi, and R. A. Frey, 2003: The MODIS cloud products: algorithms and examples from Terra. *IEEE Transactions on Geoscience and Remote Sensing*, **41 (2)**, 459–473.

Rossow, W. B., L. C. Garder, P. J. Lu, and A. W. Walker, 1991: International Satellite Cloud Climatology Project (ISCCP) Documentation of Cloud Data. World Meteorological Organization, WMO/TD-No. 266.

S-NPP Data Maturity, 2015: URL http://www.star.nesdis.noaa.gov/jpss/DataMaturity.php.

S-NPP Maturity Definitions, 2015: URL http://www.star.nesdis.noaa.gov/jpss/documents/Status/DataProductMaturityLevelDefinitions.pdf.

Seaman, C. J., Y.-J. Noh, S. D. Miller, D. T. Lindsey, and A. K. Heidinger, 2014: Evaluation of the VIIRS Cloud Base Height (CBH) EDR Using CloudSat. URL http://www.star.nesdis.noaa.gov/star/documents/meetings/2014JPSSAnnual/dayThree/04_Session5b_Seaman_VIIRS_CBH_Evaluation.pdf, Proceedings of the 1st Annual STAR JPSS Science Team Meeting, College Park, MD.

Selim, S. Z., and M. A. Ismail, 1984: K-means-type algorithms: A generalized convergence theorem and characterisation of local optimality. *IEEE Transactions on Pattern Analysis and Machine Intelligence*, **6 (1)**, 81–87.

Sivaraman, C., and J. Comstock, 2011: Micropulse Lidar Cloud Mask Value-Added Product Technical Report. Tech. Rep. TR-098, Department of Energy Atmospheric Radiation Measurement (ARM) Climate Research Facility.

Skamarock, W. C., and J. B. Klemp, 2008: A time-split nonhydrostatic atmospheric model for weather research and forecasting applications. *Journal of Computational Physics*, **227**, 3465–3485.

Theiler, J., and G. Gisler, 1997: A contiguity-enhanced k-means clustering algorithm for unsupervised multispectral image segmentation. Proceedings of SPIE 3159.

Turner, D. D., S. A. McFarlane, L. Riihimaki, Y. Shi, C. Lo, and Q. Min, 2014: Cloud Optical Properties from the Multifilter Shadowband Radiometer (MFRSRCLDOD): An ARM Value-Added Product. Tech. Rep. TR-139, Department of Energy Atmospheric Radiation Measurement (ARM) Climate Research Facility.

VIIRS Cloud Products Beta Maturity Status Report, 2013: URL http://www.nsof.class.noaa.gov/notification/pdfs/Beta%20Maturity%20Status%20Report%20for%20Cloud%20Products_v3.docx.

Wang, Z., and K. Sassen, 2001: Cloud type and macrophysical property retrieval using multiple remote sensors. *Journal of Applied Meteorology*, **40**, 1665–1682.

Warren, S. G., 2015: Personal correspondence.

Weickmann, H. K., and H. J. Aufm-Kampe, 1953: Physical properties of cumulus clouds. *Journal of Meteorology*, **10**, 204–211.

Welch, R. M., S. Asefi, J. Zeng, U. S. Nair, Q. Han, R. O. Lawton, D. K. Ray, and V. S. Manoharan, 2008: Biogeography of tropical montane cloud forests, Part I: remote sensing of cloud-base heights. *Journal of Applied Meteorology and Climatology*, **47**, 960–975.

Welliver, E., 2009: Remote detection of cloud base heights using CloudSat and CALIPSO. Master's Thesis, Naval Postgraduate School, Monterey, CA, URL http://www.dtic.mil/dtic/tr/fulltext/u2/a497032.pdf.

Williams, K. W., 2004: A Summary of Unmanned Aircraft Accident/Incident Data: Human Factors Implications. Tech. Rep. DOT/FAA/AM-04/24, Federal Aviaition Administration Civil Aerospace Medical Institute. URL http://www.dtic.mil/cgi-bin/GetTRDoc?AD=ADA460102.

Winker, D. M., J. Pelon, and M. P. McCormick, 2003: The CALIPSO mission: Spaceborne lidar for observation of aerosols and clouds. *Proceedings of SPIE*, U. N. Singh, T. Itabe, and Z. Liu, Eds., Vol. 4893, 11.

Vita

Captain Kyle E. Fitch graduated from the University of Washington with a Bachelor of Science Degree in Atmospheric Sciences in 2006 while simultaneously earning a commission into the United States Air Force. He began his career with the 17th Operational Weather Squadron as a Regional Operations Meteorologist at Hickam Air Force Base, Hawaii, where he was later elevated to the position of Officer in Charge of the Forecasting Element. Subsequently, Captain Fitch was assigned to the 18th Weather Squadron as a Staff Weather Officer for 3d Army at Fort McPherson, Georgia, where he was the Deputy Chief for Weather Plans and Requirements. During this assignment, he deployed to Afghanistan in support of Operation Enduring Freedom where he served as the Staff Weather Officer for the 10th Combat Aviation Brigade, leading 20 Battlefield Weather Airmen providing direct weather support to six battalions at five geographically-separated locations throughout eastern Afghanistan. Next, Captain Fitch was assigned to the 354th Operations Support Squadron as the Weather Flight Commander at Eielson Air Force Base, Alaska, where he led support for Pacific Air Forces' premier air refueling squadron, an alert helicopter rescue squadron, the 18th Aggressor Squadron, and a combat training squadron conducting four Red Flag - Alaska exercises. During this assignment, Captain Fitch was once again deployed to Afghanistan as the Weather Flight Commander of the busiest combat air logistics hub in the Department of Defense. Most recently, Captain Fitch was assigned to Wright-Patterson Air Force Base, Ohio, where he is currently a graduate student at the Air Force Institute of Technology.

REPORT DOCUMENTATION PAGE	*Form Approved* *OMB No. 0704-0188*

1. REPORT DATE *(DD-MM-YYYY)*	2. REPORT TYPE	3. DATES COVERED *(From - To)*
29-02-2016	Master's Thesis	May 2014 - March 2016

4. TITLE AND SUBTITLE	5a. CONTRACT NUMBER
Evaluation of the Visible Infrared Imaging Radiometer Suite (VIIRS) Cloud Base Height (CBH) Pixel-level Retrieval Algorithm for Single-layer Water Clouds	5b. GRANT NUMBER
	5c. PROGRAM ELEMENT NUMBER
6. AUTHOR(S)	5d. PROJECT NUMBER
Fitch, Kyle E., Captain, USAF	5e. TASK NUMBER
	5f. WORK UNIT NUMBER

7. PERFORMING ORGANIZATION NAME(S) AND ADDRESS(ES)	8. PERFORMING ORGANIZATION REPORT NUMBER
Air Force Institute of Technology Graduate School of Engineering and Management (AFIT/EN) 2950 Hobson Way Wright-Patterson AFB OH 45433-7765	AFIT-ENP-MS-16-M-069
9. SPONSORING/MONITORING AGENCY NAME(S) AND ADDRESS(ES)	**10. SPONSOR/MONITOR'S ACRONYM(S)**
Air Force Special Operations Command, Weather Branch Attn: Lt Col John C. Roberts 100 Bartley St., Bldg. 1, Ste. 153 W Hurlburt Field, FL 32544-5273 DSN 579-8747 afsoc.a3w@hurlburt.af.mil or john.roberts.4@us.af.mil	AFSOC/A3O-W **11. SPONSOR/MONITOR'S REPORT NUMBER(S)**

12. DISTRIBUTION/AVAILABILITY STATEMENT

DISTRIBUTION STATEMENT A: APPROVED FOR PUBLIC RELEASE; DISTRIBUTION UNLIMITED.

13. SUPPLEMENTARY NOTES

14. ABSTRACT

Evaluation of the Visible Infrared Imaging Radiometer Suite (VIIRS) Cloud Base Height (CBH) product was accomplished. CBH is an important factor for aviation, but a lack of coverage for ground-based retrieval is a significant limitation. Space-based retrieval is essential; therefore, the VIIRS CBH pixel-level retrieval algorithm was assessed for single-layer water clouds. Accurate (truth) measurements were needed not only for the CBH product, but also for VIIRS cloud optical thickness (COT), effective particle size (EPS), and cloud top height (CTH). Data from Atmospheric Radiation Measurement (ARM) sites were used, with VIIRS-ARM matchups created from June 2013 through October 2015 for four locations. After initial CBH results were large and highly variable, the VIIRS CTH product was replaced with the ARM (truth) CTH product. This substantially reduced variability and errors in the VIIRS CBH products, demonstrating that the CBH algorithm is fundamentally sound. Thus, future research is needed to reduce errors in the VIIRS CTH products in order to ensure the CBH products are suitable for aviation support.

15. SUBJECT TERMS

Cloud Base Height, VIIRS, Atmospheric Radiation Measurement, Suomi-NPP, Algorithm

16. SECURITY CLASSIFICATION OF:			17. LIMITATION OF ABSTRACT	18. NUMBER OF PAGES	19a. NAME OF RESPONSIBLE PERSON
a. REPORT	b. ABSTRACT	c. THIS PAGE			Lt Col Kevin S. Bartlett, AFIT/ENP
U	U	U	UU	114	**19b. TELEPHONE NUMBER** *(Include area code)* (937) 255-3636 x4520 kevin.bartlett@afit.edu

Reset